



THE HONG KONG
POLYTECHNIC UNIVERSITY

香港理工大學

Pao Yue-kong Library

包玉剛圖書館

Copyright Undertaking

This thesis is protected by copyright, with all rights reserved.

By reading and using the thesis, the reader understands and agrees to the following terms:

1. The reader will abide by the rules and legal ordinances governing copyright regarding the use of the thesis.
2. The reader will use the thesis for the purpose of research or private study only and not for distribution or further reproduction or any other purpose.
3. The reader agrees to indemnify and hold the University harmless from and against any loss, damage, cost, liability or expenses arising from copyright infringement or unauthorized usage.

If you have reasons to believe that any materials in this thesis are deemed not suitable to be distributed in this form, or a copyright owner having difficulty with the material being included in our database, please contact lbsys@polyu.edu.hk providing details. The Library will look into your claim and consider taking remedial action upon receipt of the written requests.

The Hong Kong Polytechnic University
Department of Land Surveying and Geo-Informatics

Retrieval of Aerosol Optical Thickness at 500m
resolution using MODIS images, a study in Hong
Kong and the Pearl River Delta region

Wong Man Sing

A thesis submitted in partial fulfilment of the requirements for the
degree of Doctor of Philosophy

November 2008

CERTIFICATE OF ORIGINALITY

I hereby declare that this thesis is my own work and that, to the best of my knowledge and belief, it reproduces no material previously published or written nor material which has been accepted for the award of any other degree or diploma, except where due acknowledgement has been made in the text.

_____ (Signed)

Wong Man Sing _____ (Name of student)

ABSTRACT of thesis entitled “Retrieval of Aerosol Optical Thickness at 500m resolution using MODIS images, a study in Hong Kong and the Pearl River Delta region” submitted by Wong Man Sing for the degree of Doctor of Philosophy at the Hong Kong Polytechnic University in 2009.

Aerosol retrieval algorithms for the MODerate Resolution Imaging Spectroradiometer (MODIS) have been developed to estimate aerosol and microphysical properties of the atmosphere which help to address aerosol climatic issues at global scale. However, higher spatial resolution aerosol products for urban areas have not been well researched, mainly due to the difficulty of differentiating aerosols from bright surfaces in urban areas. Here, a new aerosol retrieval algorithm using the MODIS 500m resolution images is described, for the retrieval of aerosol properties over complex urbanized regions such as Hong Kong and the Pearl River Delta region. The rationale of our technique is to first estimate the aerosol reflectances by decomposing the Top Of Atmosphere reflectances from surface reflectance and Rayleigh path reflectances. For the determination of surface reflectances, a modified Minimum Reflectance Technique (MRT) is used, and MRT images are computed for different seasons. A strong correlation is shown between the surface reflectances of MRT images and MODIS land surface reflectance products (MOD09), with a value of ca. 0.87, and a difference of only 0.03 between MRT images and field measured ground reflectances. For conversion of aerosol reflectance to Aerosol Optical Thickness (AOT), comprehensive Look Up Tables (LUT) are constructed which consider aerosol properties and sun-viewing geometry in the radiative transfer calculations. Four aerosol types, namely mixed urban, polluted urban, dust, and heavy pollution, were derived using cluster analysis for three years of AERONET measurements in Hong Kong, and their aerosol properties were input to the LUT calculation. The resulting 500m AOT images were found to be highly correlated with ground measurements from the AERONET ($r^2 = 0.767$) and MicrotopsII sunphotometers ($r^2 = 0.760$) in Hong Kong. This study demonstrates the feasibility of aerosol retrieval at fine resolution over urban areas. Due to the high temporal resolution of MODIS, the 500m AOT images can be used to monitor cross-boundary aerosols and the development of pollutant sources in the Pearl River Delta region surrounding Hong Kong.

PUBLICATIONS ARISING FROM THE THESIS

SCI journals (6)

Wong M.S., Lee K.H., Nichol J.E. and Li Z.Q., submitted. Retrieval of Aerosol Optical Thickness using MODIS 500 x 500m², a study in Hong Kong and the Pearl River Delta region. IEEE Transaction of Geoscience and Remote Sensing.

Wong M.S., Nichol J.E., Lee K.H. and Lee B.Y., submitted. Monitoring Fine Particulate Matter (PM_{2.5}) within urban regions using satellite-derived Aerosol Optical Thickness (AOT). Atmospheric Environment.

Wong M.S., Nichol J.E. and Lee K.H., submitted. Modeling of aerosol vertical profiles using GIS and remote sensing. Sensors.

Wong M.S., Nichol J.E., Lee K.H. and Li Z.Q., submitted. Fine resolution Aerosol Optical Thickness (AOT) retrieval from MODIS, and applications over a complex urban region. Atmospheric Research.

Nichol J.E., **Wong M.S.** and Chan Y.Y., 2008. Fine resolution air quality monitoring from a small satellite, CHRIS/PROBA. Sensors, 8(12):7581-7595.

Lee K.H., Li Z.Q., **Wong M.S.**, Xin J.Y., Wang Y., Hao W.M. and Zhao F.S., 2007. Aerosol single scattering albedo retrieval using ground-based and satellite observation data, Special Issue on East Asian Study of Tropospheric Aerosol: an International Regional Experiment (EAST-AIRE). Journal of Geophysical Research, 112(D22S15):1-17.

Refereed journals (3)

Wong M.S., Nichol J.E., Lee K.H. and Li Z.Q., 2008. A new algorithm for retrieving aerosol optical thickness using TERRA/MODIS satellite images. *The International Association of Chinese Professionals in Geographic Information Science*, 14(02):86-91 (ISSN 1082-4006).

Wong M.S. and Nichol J.E., 2006. Aerosol retrieval using hyperspectral multiple-look CHRIS satellite images. *WSEAS Transactions on Environmental and Development*, 4(2).

Wong M.S., Nichol J.E., Lee K.H., Li Z.Q. and Kwok K.H., 2009. Retrieval of Aerosol Optical Thickness over Hong Kong and Pearl River Delta region using MODIS satellite data (in Chinese). *Acta Scientiae Circumstantiae*, 7.

Conference proceedings (11)

Wong M.S., Nichol J.E. and Lee K.H., 2008. Improved estimation of aerosol optical thickness using MODIS 500 x 500m² imagery over Hong Kong and Pearl River Delta region. In *Proceedings of the First Conference on Global Change and the Environment in Asia and Pacific (GCEAP): Global and local Energy and Water Cycles Variability*, The Chinese University of Hong Kong, Hong Kong, Sep 25-26, 2008.

Wong M.S., 2008. Earth observation of air pollution in Hong Kong. *Environment, Health and Harmony: An Interdisciplinary Student Leadership Conference*, Hong Kong America Center and School of Public Health, The Chinese University of Hong Kong, Hong Kong, Jul 14-17, 2008.

Wong M.S., Lee K.H., Nichol J.E. and Li Z.Q., 2008. Retrieval of aerosol optical thickness using MODIS 500 x 500m², a study in Hong Kong and Pearl River Delta region. In Proceedings of the International Workshop on Earth Observation and Remote Sensing Applications, Beijing, Jun 30-Jul 2, 2008.

Wong M.S., Lee K.H. and Kim Y.J., 2008. Aerosol vertical profile by scaling height and its linkage with GIS technique. In Proceedings of the International Symposium on Remote Sensing ISRS2007, Seoul, South Korea, Mar 20-21, 2008.

Wong M.S., Nichol J.E. and Lee K.H., 2008. A study of aerosol vertical profiles: scaling height and extinction coefficient. In Proceedings of the 2nd Faculty Postgraduate Research Conference (2008), FCLU, The Hong Kong Polytechnic University, Hong Kong, Jan 19, 2008. ISBN: 978-988-17311-1-1.

Lee K.H., Li Z.Q. and **Wong M.S.**, 2007. Estimation of aerosol single scattering albedo by the combination of satellite and ground based measurements. In Proceedings of the Gordon Research Conference on Radiation & Climate, Colby-Sawyer College, New London, New Hampshire, U.S., Jul 9-Aug 3, 2007.

Holben B.N., Eck T., Smirnov A., Sinyuk A., Dubovik O., Slutsker I., Giles D., Sorokine M., Chin M., Remer L., Goloub P., Li Z., Chen H.B., Panchenko M.V., Boonjawat J., Lin N.H., Lin P.H., Le H.V., Yoon S.C., Singh R.P., **Wong M.S.**, Nichol J., Huang J., Zareen R., 2007. Continental scale aerosol optical properties over east Asia as measured by AERONET and comparison to satellite and modeled results. The 5th Asian Aerosol Conference (2007), Kaoshiung, Taiwan, Aug 26-29, 2007.

Wong M.S., Nichol J.E., Lee K.H. and Li Z.Q., 2007. Analysis of seasonal variation of aerosol optical depth and characterization of aerosol model using MODIS and AERONET measurements, a study in Hong Kong. In Proceedings of the 10th International Conference on Atmospheric Sciences and Applications to Air Quality, Hong Kong, May 14-16, 2007.

Wong M.S., Nichol J.E., Lee K.H. and Li Z.Q., 2007. Development of aerosol retrieval algorithm using small satellite (CHRIS), a study in Hong Kong. In Proceedings of the 10th International Conference on Atmospheric Sciences and Applications to Air Quality, Hong Kong, May 14-16, 2007.

Wong M.S. and Nichol J.E., 2006. Preliminary study of aerosol retrieval using multiple-look, hyperspectral satellite images. In Proceedings of the 2006 IASME/WSEAS International Conference on Energy, Environment, Ecosystems and Sustainable Development (EEESD'06), Athens, Greece, Jul 11-13, 2006.

Wong M.S. and Nichol J.E., 2006. Investigation of the geometric effects of multiple view angle satellite images on surface reflectance: a preliminary study for aerosol retrieval. In Proceedings of the 1st Faculty Postgraduate Research Conference (2006), FCLU, The Hong Kong Polytechnic University, Hong Kong, Nov 4, 2006.

ACKNOWLEDGEMENTS

I would like to thank Prof Janet Nichol for her supervision and contribution to this study. Prof Nichol provided a great deal of valued and vital ideas to me, and she gave many opportunities for me to be involved in and handle a variety of projects. These projects allowed me to widen my horizons and produced international publications.

I am grateful to Prof Zhanqing Li and Dr Kwon Ho Lee at the University of Maryland, Dr Brent Holben from NASA for the help with the Hong Kong PolyU AERONET station, Prof Long Sang Chiu and Prof Soo Chin Liew for valuable comments and Prof Wen Zhong Shi for chairing the board of examination.

I also sincerely thank the staff, colleagues and students in the Department of Land Surveying and Geo-Informatics of the Hong Kong Polytechnic University with grateful support.

Lastly, I gratefully thank the Research Committee and Research Office for their comments and administration. This study was funded by the Hong Kong Government CERG grant no. PolyU 5253/07E.

TABLE OF CONTENTS

	Page
ABSTRACT	1
PUBLICATIONS ARISING FROM THE THESIS	2
ACKNOWLEDGEMENTS	6
TABLE OF CONTENTS	7
LIST OF FIGURES	10
LIST OF TABLES	14
LIST OF FORMULAE	15
1. LITERATURE REVIEW	16
1.1. What are aerosols?	16
1.2. Historical understanding of tropospheric aerosols	17
1.3. Anthropogenic aerosols	17
1.4. Geographical classification of aerosols	18
1.5. Transportation and residence time	20
1.6. Aerosol-climate interaction	21
2. AEROSOL OBSERVATIONS FROM SATELLITES	23
2.1. Methodologies of aerosol observations from satellites	23
2.2. Objectives	29
3. STUDY AREA AND DATA USED	30
3.1. Study area	30
3.2. Data used	32
3.2.1. AERONET	32
3.2.2. MODIS	33

4.	AEROSOL OBSERVATIONS IN HONG KONG AND THE PEARL RIVER DELTA REGION	35
4.1.	MODIS collection 4 and 5 data versus AERONET measurements	35
4.2.	Seasonal and yearly variations of AOT from MODIS images	38
5.	METHODOLOGY	41
5.1.	Rayleigh correction of TOA images	43
5.2.	Derivation of surface reflectance images	49
5.3.	Look up table construction	56
5.3.1.	Local aerosol models	60
5.4.	Aerosol retrieval	64
5.4.1.	Deriving image aerosol reflectances	65
5.4.2.	Deriving modeled aerosol reflectances	66
5.4.3.	Deriving AOT	66
6.	RESULTS	68
6.1.	Validation of surface reflectance images (MRT vs MOD09)	68
6.2.	Validation of surface reflectance images (MRT vs MSR field measurements)	73
6.3.	Validation of cloud masking with Hong Kong Observatory data	76
6.4.	Validation of image derived AOT (500m) with AERONET measurements	77
6.5.	Validation of image derived AOT (500m) with MicrotopsII measurements	81
6.6.	Comparisons between AOT 500m image and AOT 10km image	85
6.7.	Anthropogenic aerosol emission observed from AOT images	87
6.8.	Aerosols from biomass burning observed from AOT images	91
6.9.	Monitoring fine particulate matter (PM _{2.5}) using AOT images	95

7.	DISCUSSION	100
8.	CONCLUSION	105
	REFERENCES	107

LIST OF FIGURES

Figure 1.1.	Urban aerosols, a. smoke being carried into street, b. smoke from urban industries	19
Figure 1.2.	Size ranges of atmospheric aerosols	20
Figure 1.3.	A diagram illustrates the relationship between radiative forcing and climate response	21
Figure 3.1.	Map of Hong Kong and AERONET station	30
Figure 3.2.	AERONETs deployed on the a. library roof of the Hong Kong Polytechnic University, b. remote peninsula in the southeast of Hong Kong island	33
Figure 3.3.	MODIS sensor	34
Figure 4.1.	Area of interest around AERONET station	35
Figure 4.2.	Scatter plots, a. between MOD04 collection 4 with AERONET measurements; b. between MOD04 collection 5 with AERONET measurements	36
Figure 4.3.	Collection 5 AOT derived from land and ocean algorithms	37
Figure 4.4.	AOT seasonal and yearly variations a. between 2000 and 2003, b. between 2004 and 2007	39
Figure 4.5.	Daily AOT variation in 2006, between Hong Kong and Guangzhou	40
Figure 5.1.	The schematic diagram for aerosol retrieval in the study	42
Figure 5.2.	a. TOA reflectance image, b. Rayleigh corrected reflectance image (masked with water and clouds) and c. Rayleigh reflectance image at 470nm	48
Figure 5.3.	Empirical ratios for vegetated areas: a. Blue/SWIR, b. Red/SWIR; Empirical ratios for urban areas: c. Blue/SWIR, d. Red/SWIR	52

Figure 5.4.	Histograms of different surface reflectance values from first minimum reflectance and second minimum reflectance images, a. at 470nm in autumn season, b. at 470nm in winter season	54
Figure 5.5.	Surface reflectance images in the autumn (in UTM grid coordinate system); a. RGB composite of MRT, b. MRT at 470nm, c. MRT at 550nm, d. MRT at 660nm	56
Figure 5.6.	Sample distances calculated from hierarchical clustering method, a. a range from 0 to 730, b. a range from 710 to 730	58
Figure 5.7.	Plot of distances from cluster centers by cluster memberships	59
Figure 5.8.	Scatter plots, a. three-dimensional scatter plot of four clusters, b. two-dimensional scatter plot of four clusters	60
Figure 5.9.	Aerosol size distributions used in this study	63
Figure 5.10.	The SBDART calculations were performed with solar zenith angle = 30° , satellite zenith angle = 10° , azimuth angle = 150°	64
Figure 6.1.	Surface reflectance images in the autumn (in UTM grid coordinate system); a. RGB composite of MOD09, b. MOD09 at 470nm, c. MOD09 at 550nm, d. MOD09 at 660nm	70
Figure 6.2.	Scatter plots between surface reflectances derived from MRT and from MOD09 products: a. at 470nm in spring, b. at 550nm in spring, c. at 660nm in spring, d. at 470nm in autumn, e. at 550nm in autumn, f. at 660nm in autumn, g. at 470nm in winter, h. at 550nm in winter, i. at 660nm in winter	72
Figure 6.3.	Field measurements of surface reflectances over dense vegetation	73
Figure 6.4.	Locations of field measurements overlaid with the winter MRT image	74

Figure 6.5.	Scatter plots, a. between MODIS 500m AOT and AERONET measurements; b. between MOD04 collection 4, 5 AOT and AERONET measurements	78
Figure 6.6.	Histogram of occurrences for different aerosol types derived from the MODIS 500m algorithm	80
Figure 6.7.	Locations of MSR field measurements, a. Mong Kok (urban area), b. Hung Hom (urban area), c. Tsuen Wan (rural area) d. Shing Mun (rural area)	83
Figure 6.8.	MODIS 500m AOT images on a. Nov 11 2007, b. Nov 28 2007, c. Dec 14 2007	84
Figure 6.9.	Scatter plot between MODIS 500m AOT and MicrotopsII measurements	85
Figure 6.10.	a. AOT at 550nm derived from MODIS MOD04 collection 5 algorithm, b. AOT at 550nm and 500m resolution derived from this study over Hong Kong and the Pearl River Delta region	86
Figure 6.11.	AOT at 550nm and 500m resolution derived from this study overlaid with GIS road data	87
Figure 6.12.	a. Color composite RGB image on Jan 28 2007; AOT at 550nm and 500m resolution derived from this study over Hong Kong and the Pearl River Delta region on, b. Jan 28 2007, d. Jan 30 2007; MODIS collection 5 AOT products (10km) on, c. Jan 28 2007, e. Jan 30 2007	90
Figure 6.13.	Wind speed maps over the whole of south China on, a. Jan 28 2007, b. Jan 29 2007, c. Jan 30 2007	91
Figure 6.14.	a. Rayleigh corrected RGB image on Nov 30 2007, b. AOT 500m image, c. AOT collection 5 10km image, d. Fire spots shown on Nov 30 2007 from the Web Fire Mapper	94
Figure 6.15.	Monitoring stations in Hong Kong overlaid	

	with MODIS collection 5 AOT image on Jan 28 2007	96
Figure 6.16.	a. Yearly average collection 5 AOT in 2007,	
	b. modeled yearly PM _{2.5} concentrations ($\mu\text{g}/\text{m}^3$) in 2007	97
Figure 6.17.	a. Scatter plot of MODIS 500m AOT data	
	versus PM _{2.5} measurements, b. 500m AOT map over	
	Hong Kong on Jan 28 2007, c. modeled PM _{2.5}	
	concentrations at 500m resolution over Hong Kong	
	on Jan 28 2007	99

LIST OF TABLES

Table 4.1.	Statistical comparison between the performances of collection 4 and collection 5, with AERONET data	37
Table 5.1.	Coefficients of B, C, D in Rayleigh scattering	44
Table 5.2.	Coefficients of A in Rayleigh scattering	45
Table 5.3.	Distances between cluster centers	59
Table 5.4.	Summary of the cluster analysis results	61
Table 6.1.	Statistical comparison between the surface reflectances of MRT and MOD09	73
Table 6.2.	Surface reflectances from MRT images and multispectral radiometer field measurements	76
Table 6.3.	Confusion matrix of cloud masking	77
Table 6.4.	Statistical comparison between the performances of collection 4 and collection 5, MODIS 500m AOT with AERONET and MicrotopsII data	79
Table 6.5.	AOT measurements from MicrotopsII on different dates	84
Table 6.6.	Meteorological conditions on different dates	85
Table 7.1.	Summary of different aerosol retrieval methods	101

LIST OF FORMULAE

Equation 1.1.	Beer's law	16
Equation 2.1.	Kaufman's DDV algorithm (Blue/SWIR)	24
Equation 2.2.	Kaufman's DDV algorithm (Red/SWIR)	24
Equation 2.3.	MODIS collection 5 algorithm	25
Equation 2.4.	MODIS collection 5 algorithm	25
Equation 2.5.	MODIS collection 5 algorithm	26
Equation 2.6.	MISR operational algorithm	27
Equation 2.7.	MISR operational algorithm	28
Equation 2.8.	MISR operational algorithm	28
Equation 5.1.	Aerosol retrieval algorithm	43
Equation 5.2.	Rayleigh scattering optical thickness	44
Equation 5.3.	Parameterized barometric equation	45
Equation 5.4.	Air mass calculation	45
Equation 5.5.	Rayleigh optical thickness corrected by temperature	46
Equation 5.6.	Atmospheric transmittance (ground to sensor)	46
Equation 5.7.	Atmospheric transmittance (sun to ground)	46
Equation 5.8.	Rayleigh optical thickness for multiple scattering	46
Equation 5.9.	Nadir reflection by Rayleigh scattering	47
Equation 5.10.	Rayleigh reflectance can be obtained by geometric correction	47
Equation 5.11.	Water masking algorithm	49
Equation 5.12.	Cloud masking algorithm	49
Equation 5.13.	Aerosol retrieval algorithm (simplified)	65
Equation 5.14.	Hemispheric reflectances	66
Equation 5.15.	Aerosol reflectance as a function of AOT	66
Equation 5.16.	Optimal spectral shape-fitting	67
Equation 6.1.	Angstrom exponent calculation	81
Equation 6.2.	Linear regression between MODIS 500m AOT and PM2.5	97

CHAPTER 1.

LITERATURE REVIEW

1.1. *What are aerosols?*

Aerosols are particles suspended in the atmosphere in either liquid or solid form. They have different size distributions, shapes and residence times, and are from different sources. The study of aerosol is important because of its effects to the earth radiation budget, climate change, atmospheric conditions and human health. Recent researches have been focused on fine aerosols for their long term damage to the respiratory system (Davidson et al., 2005; Dominici et al., 2006).

At global level, aerosols and clouds which are closely associated with them play an especially important role in the earth's energy budget. If there were no aerosols in our atmosphere, several problems would occur, i. the earth surface's solar radiation would increase since there would be no particle scattering and absorption in the atmospheric column, ii. cloud formation would cease since there was no aerosol particle to act as Cloud Condensation Nuclei (CCN), which is the main element in cloud formation.

Aerosol Optical Thickness (AOT) is a unit of measurement for aerosols, and it is defined as the total attenuation along a path, measured vertically in the atmosphere. It accounts for the sum of attenuation due to scattering and absorption.

$$I = I_0 e^{-\tau_\lambda m} \quad \text{Eq 1.1.}$$

where τ_λ is the optical thickness as a function of wavelength, m is airmass, I_0 is the intensity of radiation at the source and I is the observed intensity at a given path length.

1.2. Historical understanding of tropospheric aerosols

The definition of tropospheric aerosol is the air mass or particle volume between the tropospheric layer and the ground, where tropospheric layer is defined as the layer of atmosphere above the ground with a negative lapse rate (i.e. where temperature decreases with height) and it extends to approximately 10km above the ground. Most of the clouds are found and most aerosols are formed in this layer.

Traditionally, aerosols are considered to be equivalent to “haze” and “dust”. Early observations of aerosols were carried out visually. In the last hundreds years, there were many observations and studies of aerosols. It is well-known that Mie (1908) developed a theory for analyzing the aerosol particle sizes and their optical characterizes, hence the term “Mie particles”. Junge (1952) first illustrated the continuous aerosol size distribution, covering radii from 0.01 μm to 10 μm , where particles less than 0.1 μm are produced by reactive gases in atmosphere such as sulfur dioxide (SO_2) or fires, and particles larger than 1 μm are produced by natural environmental processes such as from windblown soil and sea salt (Hobbs, 1993). These general definitions were adopted and used in further research studies.

1.3. Anthropogenic aerosols

Industrial and vehicle emission can be said to be the main source of anthropogenic aerosols. The emission of sulfur dioxide, organic gases, smoke and haze always produce sulfate aerosols. The National Research Council (1996) shows that 65 to 80 teragrams of SO_2 are released globally per year. Approximately 80 to 90% of the sulfur emissions can be transformed into sulfate aerosols, and may form haze or cloud condensation nuclei. These processes, along with others are said to have caused a substantial decrease of solar irradiance related especially to sulfate along with other anthropogenic aerosols. A study conducted in the United States on regional scale atmospheric sulfur concentration, between pre- and post- industrial times found that the annual loss of solar irradiance was

ca. 7.5%, from sulfate and other anthropogenic aerosols (Ball and Robinson, 1982). Liepert et al. (1994) show that solar irradiance has decreased by 3 to 4 % over Europe in the last 40 years. These studies indicate that the increase of sulfate aerosols from industrial emission is a major factor in the loss of solar irradiance from the earth, causing significant global cooling.

According to the size, the residence time or lifetime of aerosols in the air varies. Large dust particles remain suspended for minutes to hours, submicrometer aerosols have days to weeks lifetime, and stratospheric aerosols from volcanic eruptions have years of lifetime (National Research Council, 1996).

1.4. Geographical classification of aerosols

Different aerosol types have their own characteristics, six types of aerosols are introduced here:

Background aerosols – These are aerosols located above the cloud layers and most measurements are carried out in high mountains.

Maritime aerosol – These aerosols are combined with sea salt, and the maritime environment is normally characterized as having aerosol concentrations around 100 particles per cm^3 .

Remote continental aerosols – These aerosols are assumed to be unaffected by human activities.

Desert dust storm aerosols – These are the aerosols with low concentration (ca. 1500cm^{-3}), but with heavy mass loading and long transportation ability.

Rural aerosols – Rural aerosols are derived mainly from natural origins such as plant pollen and organic particles, these are the aerosols in continental areas without direct influence by urban and industrial sources.

Urban aerosols – These are anthropogenic emissions aerosols mostly from industrial, home heating, traffic, power plant etc (Figure 1.1). They have higher concentrations than the other geographically classified aerosols. The particle sizes range between 0.01 to 10 micron radius. High concentrations of particles can be found near the sources and fewer further away. Also, the chemical composition of small and coarse particles is different. Small particles are the products of combustion and from chemical reactions (gas-to-particle conversion) of sulfate etc and they have particle sizes between 0.001 to 0.5 μm (Wallace and Hobbs, 2006) (Figure 1.2). Coarse particles tend to result from mechanical processes and are composed of dust, sea salt, ash etc (Seinfeld and Pandis, 1998) and they have particle sizes between 0.5 to 5 μm (Wallace and Hobbs, 2006).



Figure 1.1. Urban aerosols, a. smoke being carried into street, b. smoke from urban industries (adopted from Scorer, 2002)

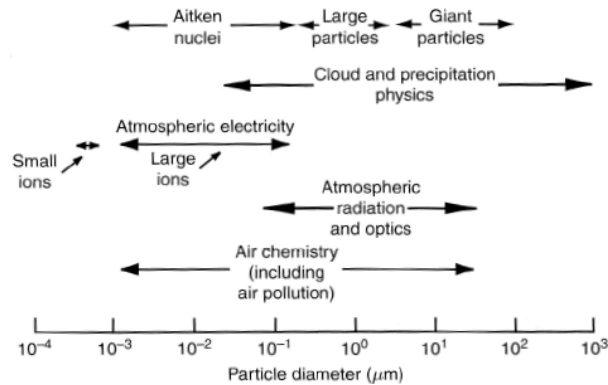


Figure 1.2. Size ranges of atmospheric aerosols (adopted from Wallace and Hobbs, 2006)

1.5. *Transportation and residence time*

Hobbs et al. (1993) shows that tropospheric aerosols can be transported not only regionally, but inter-continently, and Schutz et al. (1990) show that Saharan dust can be transported over great distances across the desert, and even across the Atlantic ocean to reach America. Sometimes, they can even reach the rainforest in South America (Swap et al., 1992). Their vertical transportation and distribution are traditionally measured by sampling and modeling, since most of the calculations are based on modeling as there was little supporting evidence until the Light detection and ranging (Lidar) instrument was developed. The methodology of Lidar is based on laser penetration and transmission for measuring atmospheric aerosol profiles. A laser light pulse is transmitted and atmospheric particles are encountered. Backscattering radiation is collected and translated to optical signal against time and distance. Cheng et al. (1999) used Lidar to show the anthropogenic aerosols from traffic, industrial and human-induced pollutants often remain stable at 700m altitude in the Hong Kong city center. However, since Lidar only provides the backscattering signal of the profile, there is a need to use a sunphotometer to obtain the total optical thickness. In 2005 and 2007, AEROSOL ROBOTIC NETWORK (AERONET) stations were deployed for aerosol optical thickness measurements in urban (library roof of the Hong Kong Polytechnic University) and rural (Hok Tsui - a remote

peninsula in the southeast of Hong Kong island) areas of Hong Kong. More details of AERONET stations will be described in Section 3.2.1.

1.6. *Aerosol-climate interaction*

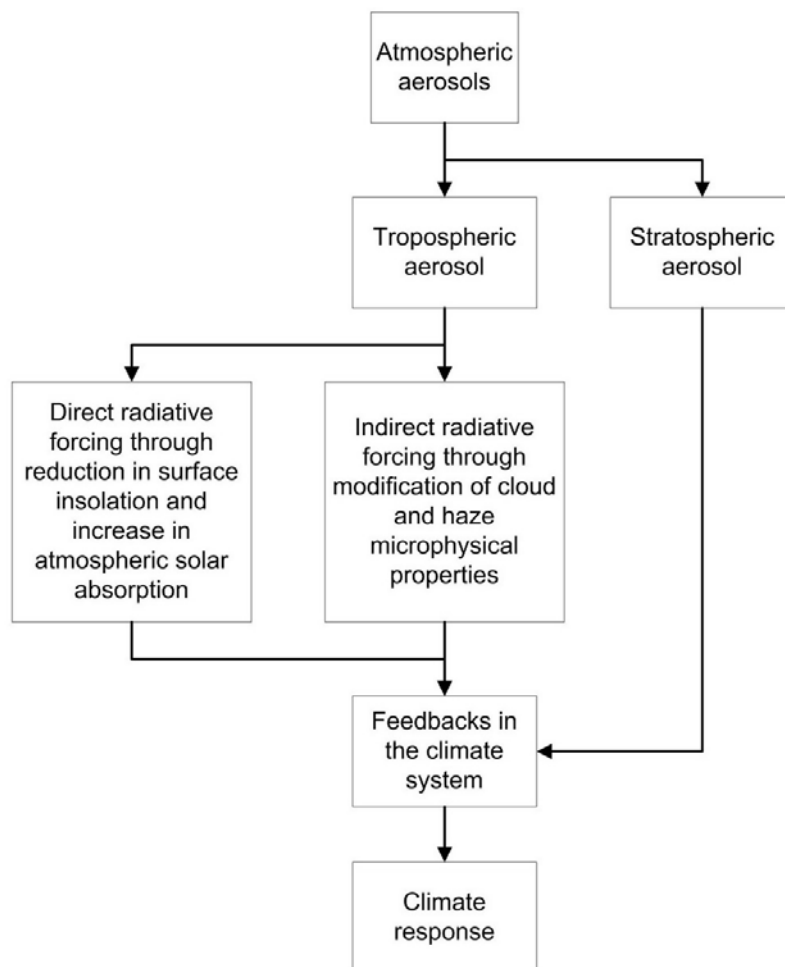


Figure 1.3. A diagram illustrates the relationship between radiative forcing and climate response (Hobbs, 1993)

Figure 1.3 illustrates the relationship between the atmospheric aerosol and climate response. Through the direct radiation (reducing the earth surface insolation and increasing the solar absorption) and indirect radiation (modification of the cloud and haze

microphysical properties), the energy flux changed by tropospheric aerosols is ca. 1.6 Wm^{-2} in 2005 (IPCC, 2007), which is negligible compared to the energy flux in and out of the earth (200 Wm^{-2}), but these 1 to 2% differences can cause significant changes in temperature and rainfall.

CHAPTER 2.

AEROSOL OBSERVATIONS FROM SATELLITES

2.1. Methodologies of aerosol observations from satellites

Retrieval of aerosols from satellite remote sensing is not straightforward because no single algorithm can work with all land surface types. The main state-of-the-art aerosol retrieval algorithms are classified either i. for land (vegetation), ii. for land (bright surfaces), or iii. for ocean. To accomplish these, many sensors have been designed with their purposes specifically for aerosol retrieval as opposed to those which are not explicitly designed for this application such as Advanced Very High Resolution Radiometer (AVHRR) whose primary purpose is the measurement of sea surface temperature and vegetation index. Total Ozone Mapping Spectrometer (TOMS) whose primary purpose is for monitoring ozone content (Herman et al., 1997; Hsu et al., 1999), Sea-viewing Wide Field-of-view Sensor (SeaWiFS) which is developed to study ocean colour and marine biogeochemical processes. However the Earth Observation System (EOS) TERRA with the instruments MODerate Resolution Imaging Spectroradiometer (MODIS) and Multiangle Imaging SpectroRadiometer (MISR) do provide capabilities for atmosphere, as well as land and ocean studies (Tanré et al., 1997; Wanner et al., 1997).

Aerosol remote sensing can be classified into three major types. These are multi-wavelength retrieval (MODIS, MISR, AVHRR), polarization retrieval (POLarization and Directionality of the Earth's Reflectances - POLDER), and active measurement (Lidar). In the current study, focus will be placed on studies using multi-wavelength algorithms. Following the launch of MODIS, a number of algorithms for aerosol retrieval were devised. These state-of-the-art methodologies include i. Dense Dark Vegetation (DDV) algorithm (known as collection 4 algorithm) (Kaufman and Tanré, 1998), ii. Second generation MODIS operation algorithm (known as collection 5 algorithm) (Levy et al., 2007), iii. Deep Blue algorithm (Hsu et al. 2004, 2006) and iv. Multi-angle algorithm

(Martonchik et al., 1998, 2002). These multi-wavelength algorithms take advantages of different aerosol scattering properties at different wavelengths (eg. longer wavelength has smaller aerosol loading). Thus, by virtue of their spectral differences, aerosol can be inferred from longer and shorter wavelengths. The following section will briefly describe the rationales and operational methodologies of these methods (i, ii, iii, iv).

Kaufman and Tanré (1998) proposed the Dense Dark Vegetation (DDV) method using a ShortWave InfraRed (SWIR) (2.1 μm) wavelength to estimate surface reflectances for shorter wavelength bands (red 0.66 μm and blue 0.47 μm regions) over dense forest. This methodology only works over dense forest and it only works with > 60% vegetation in a selected kernel. Based on the analysis of band correlation, Kaufman and Tanré (1998) and Kaufman and Sendra (1987) give equations for estimating the surface reflectances for red and blue wavelengths (Equations 2.1, 2.2):

$$\rho_{0.47\mu\text{m}} = 0.25 \cdot \rho_{2.12\mu\text{m}} \quad \text{Eq 2.1.}$$

$$\rho_{0.66\mu\text{m}} = 0.5 \cdot \rho_{2.12\mu\text{m}} \quad \text{Eq 2.2.}$$

The residual between the original Top of Atmospheric (TOA) reflectances and derived surface reflectances is assumed to be due to aerosol. This amount is then fitted to a best fit aerosol model, with knowledge of the expected aerosol types in the study area, for example, continental (Lenoble and Brogniez, 1984), industrial/urban (Remer et al., 1996), biomass burning (Hao and Liu, 1994), and marine (Husar et al., 1997), to arrive at the Aerosol Optical Thickness (AOT) from the image wavebands. Dubovik et al. (1998) suggested that a window size of 10km gives the best signal to noise ratio for global aerosol retrieval using MODIS. There are several limitations of this method including: i. only coarse resolution can be achieved, ii. it is limited to vegetated areas and cannot address for urban areas, iii. low accuracy in coastal areas especially in southeast China (Kaufman and Tanré, 1998). In addition, Chu et al. (2002) showed that the collection 4 (Kaufman's algorithm - Equations 2.1, 2.2) had a positive bias in comparison to the AERONET sunphotometer data. Remer et al. (2005) and Levy et al. (2004) reported certain inherent problems in determining surface reflectance using the MODIS collection

4 algorithm. Their results imply that inaccurate surface properties can lead to errors ($\pm 0.05 \pm 0.2\tau$) in aerosol retrieval.

Resulting from these perceived errors, Levy et al. (2004) and Remer et al. (2005) compared the accuracy of MODIS collection 4 (Kaufman's algorithm - Equations 2.1, 2.2) data with AERONET data and obtained a correlation of $r^2 = 0.64$, but the MODIS collection 4 AOT tended to be biased high in low AOT condition and low in high AOT condition. Only 68% of MODIS AOT data fell within the expected error of $\pm 0.05 \pm 0.15\tau$ which indicated the need to improve Kaufman's method. Levy et al. (2007) then modified the algorithm by taking into consideration i. band correlation based on vegetation index ($NDVI_{SWIR}$) and ii. the scattering angle, since Gatebe et al. (2002) and Remer et al. (2001) suggested the VISIBLE/SWIR ratio is angle dependent. The rationale of Levy's method (collection 5) is to first identify the dark pixels using the $NDVI_{SWIR}$ (Equation 2.3). The 400 pixels at 500m resolution in the 10km box are evaluated and screened pixel by pixel. The pixel is selected when its surface reflectance is less than 0.25 at $2.12\mu m$ whereas the DDV algorithm operates with the threshold of 0.15. The darkest 20% and brightest 50% of pixels inside the box are discarded, and the remaining 30% or at least 12 pixels inside the box are used for $NDVI_{SWIR}$ calculation. The modified $NDVI_{SWIR}$ is superior to $NDVI_{NIR}$ as it is less influenced by aerosols except for heavy aerosols or dust. Following this the images are classified into three categories based on the $NDVI_{SWIR}$ (Equation 2.4) and the f-linear equations (Equation 2.5) are applied to those three categories with three sets of slope and intercept values. The values of the linear equations are determined by band correlation analysis using atmospherically corrected MODIS images.

$$NDVI_{SWIR} = \frac{(\rho_{1.24\mu m} - \rho_{2.12\mu m})}{(\rho_{1.24\mu m} + \rho_{2.12\mu m})} \quad \text{Eq 2.3.}$$

$$\begin{aligned} NDVI_{SWIR} &< 0.25 \\ 0.25 &< NDVI_{SWIR} < 0.75 \\ NDVI_{SWIR} &> 0.75 \end{aligned} \quad \text{Eq 2.4.}$$

$$\begin{aligned}\rho_{0.66\mu m} &= f_1(\rho_{2.12\mu m}) \\ \rho_{0.47\mu m} &= f_2(\rho_{2.12\mu m})\end{aligned}\tag{Eq 2.5.}$$

The collection 5 algorithm also operates on bright surface areas if the surface reflectance at 2.12 μ m is less than 0.4 and the number of pixels inside the 10km kernel is larger than 12. Then the 0.47 μ m channel is used for aerosol retrieval and the continental model is assigned during the Look Up Table (LUT) calculation. Both the capability of bright surface aerosol retrieval and increased threshold of surface reflectance for dark pixel selection (0.15 in DDV and 0.25 in collection 5) allow collection 5 algorithm to work on semi-urban and suburban areas, although the method still does not work well over large and very bright surfaces such as deserts or complex land surfaces. Also, since only one band at 0.47 μ m wavelength is used and only one aerosol model is assigned for aerosol retrieval, the quality of AOT is deemed to be poor, with greater uncertainty over bright surfaces. Nevertheless, when new collection 5 data was evaluated (Li et al., 2007; Mi et al., 2007), it was deemed to have significant improvements in both accuracy and spatial continuity of the aerosol optical thickness than the original DDV algorithm.

Aerosol retrieval over bright surfaces is challenging because the land surface and atmospheric aerosol contents are not easy to differentiate due to both having high reflectance values. The operational DDV and collection 5 algorithms retrieve aerosol over land when the surface reflectances are less than 0.15 and 0.25 at 2.12 μ m wavelength respectively. They are unable to retrieve aerosol over large bright surface areas like Mongolian desert which is most important dust source in China. Hsu et al. (2004, 2006) recently developed a Deep Blue algorithm for aerosol retrieval over bright surfaces such as desert, arid, semiarid using MODIS images. Their algorithms make use of the blue wavelengths (412nm and 490nm) where the surface reflectances are bright in the red region and darker in the blue region. The Deep Blue algorithm has only been demonstrated successfully for large homogeneous surfaces such as deserts, but not for areas of complex land cover like urban areas.

In order to estimate aerosols over variable cover types including bright and dark surfaces, the Minimum Reflectance Technique (MRT) was developed for TOMS (Herman and Celarier, 1997) and Global Ozone Monitoring Experiment (GOME) (Koelemeijer et al., 2003) data at coarse resolution (> 1 degree). In view of the coarse resolution the accuracy of AOT (of within AOT = $\pm 30\%$ of AERONET ground measurements) could be considered good. The coarse (10km) spatial resolution of MODIS aerosol products only provides meaningful depictions on a broad regional scale, whereas aerosol monitoring over complex regions, such as Hong Kong (1,095km²) requires more spatial and spectral detail. The only “high” resolution aerosol study, by Li et al. (2005), who applied the MODIS collection 4 algorithm at the resolution of 1km to retrieve AOT over Hong Kong, was limited to dark vegetated areas and the results were validated only between October and December 2003 using handheld sunphotometers. Accuracy was within 15-20% compared with handheld sunphotometer measurements.

Instead of single-view satellite sensors, multiple view angle sensors such as National Aeronautics and Space Administration’s (NASA) MISR have been applied to aerosol retrieval recently. The advantage of multiple view angles is that different depths of atmospheric columns are obtained for more accurate aerosol estimations. Martonchik et al. (1998, 2002) developed the heterogeneous areas algorithm for the application of aerosol retrieval using MISR images. This technique works over both urban and vegetated areas and the basic requirement is to have sufficient spatial contrast over the scene. The rationale of this method uses the spatial contrasts over different viewing angles for deriving an Empirical Orthogonal Function (EOF). First, the scatter matrix is calculated on the basis of a suitable subregion (image kernel):

$$C_{ij} = \sum_{x,y} [L_{x,y}^{MISR}(i) - \langle L^{MISR}(i) \rangle] \cdot [L_{x,y}^{MISR}(j) - \langle L^{MISR}(j) \rangle] \quad \text{Eq 2.6.}$$

where $L_{x,y}^{MISR}$ is the MISR radiance at pixel location x, y within the region, $\langle L^{MISR} \rangle$ is the average radiance of the 16 x 16 pixels within the subregion, and i and j denote particular MISR sensor view. The subtraction process (Equation 2.6) completely removes any

effect of the atmospheric path radiance, assuming that the atmosphere is laterally homogeneous within the subregion.

Then the eigenvectors and eigenvalues of matrix C are calculated to be used to express the component of MISR radiances which is directly and diffusely transmitted from the surface. C can be expressed using the eigenvectors $f_{i,n}$ and eigenvalues λ_n as below:

$$\sum_{j=1}^{N_{sen}} C_{i,j} \cdot f_{j,n} = \lambda_n \cdot f_{i,n} \quad \text{Eq 2.7.}$$

In the implementation, only the first largest eigenvalues are used in determining the aerosol optical thickness. After determining the eigenvalues and eigenvectors, an optimal index is calculated using the following formula:

$$\chi_N^2(\tau) = \frac{1}{N_{band} N_{sen}} \sum_{l=1}^{N_{band}} \sum_{j=1}^{N_{sen}} \left[\frac{\langle \rho_{MISR}(l, j) \rangle - \rho^{TOA}(l, j) + \sum_{n=1}^N \lambda_n f_{j,n}(l)}{\sigma_{abs}^2(l, j)} \right]^2 \quad \text{Eq 2.8.}$$

The aerosol optical thickness is estimated from the minimum χ^2 for each value of N . For the aerosol model being evaluated, the reported best-fitting optical thickness is then computed from a weighted average of all N_{max} optical thicknesses.

The limitations and drawbacks of this method are firstly that it works with low spatial resolution satellite images and for example, when applied to the MISR images (Martonchik et al., 2002), the resolution of the resulting aerosol product is 17.6 x 17.6 km, and secondly the accuracy of AOT is sensitive to the selected aerosol model.

2.2. Objectives

This study presents and evaluates a remote sensing methodology for retrieving regional and local scale aerosols in Hong Kong and the Pearl River Delta (PRD). In order to develop and validate the methodology, investigations and evaluations are undertaken as follows.

- (i) Validation of the aerosol retrievals from MODIS collection 4 and collection 5 data against AERONET measurements in Hong Kong
- (ii) Analysis of the seasonal and yearly variations of AOT in Hong Kong and the Pearl River Delta region using MODIS measurements
- (iii) Development of a surface reflectance database based on the modified “Minimum Reflectance Technique”
- (iv) Development of a local aerosol Look Up Table using cluster analysis on three years of AERONET measurements in Hong Kong
- (v) Validation of the modified “Minimum Reflectance Technique” with field measurements and MODIS surface reflectance products (MOD09)
- (vi) Validation of the derived AOT at 500m resolution with AERONET and MicrotopsII sunphotometer measurements
- (vii) Analysis of the feasibility of using MODIS 500m AOT for monitoring biomass aerosols, anthropogenic emission and for modeling fine particulate matter

CHAPTER 3.

STUDY AREA AND DATA USED

3.1. Study area

Hong Kong is a city in south east China with a service-based economy (Figure 3.1). It has suffered serious air pollution over the last decade. Its nearby Pearl River Delta (PRD) region, has been increasingly vulnerable to direct developments such as urbanization and industrial expansion. The cities of Hong Kong and Macau, situated on opposite sides of the PRD, are directly affected in their economy and activities by such changes. CH2M (2002) show that in the year 1997 emission inventory for volatile organic compounds (VOC), respiratory suspended particles (RSP), nitrogen oxides (NO_x), and sulphur dioxide (SO₂), the PRD region was the dominant source area for emissions with 88% of VOC, 95% of RSP, 80% of NO_x and 87% of SO₂ in the whole Guangdong province. Most of the NO_x and SO₂ are from power generation especially from power plants, of which there are 45 in Guangdong Province whereas Hong Kong has two. The largest power plant in Guangdong province is Shajiao power plant, which provides 4,000 MW capacity. It emitted 90,000 tonnes of SO₂ in 2003 (Business Environment Council, 2005).

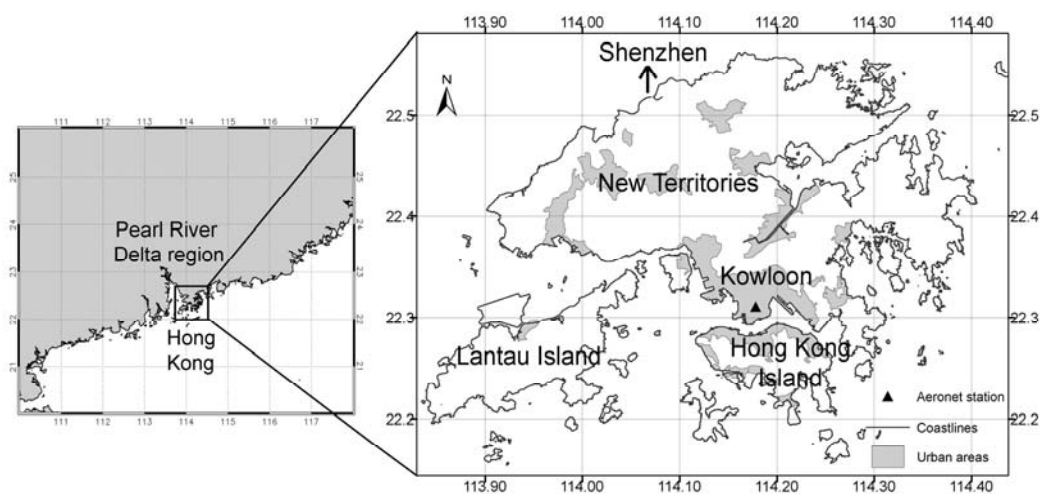


Figure 3.1. Map of Hong Kong and AERONET station

The PRD region is often covered with haze and grey smoke observed on daily MODIS satellite images. Wu et al. (2005) showed that the aerosol optical thickness in this region is often higher than 0.6 at 550nm. Previous studies in the PRD region have measured a range of particle concentrations for PM10 (particulate matter with aerodynamic diameter less than or equal to 10 micrometers) of 70 - 234 $\mu\text{g}/\text{m}^3$, with high average PM10 concentrations of above 200 $\mu\text{g}/\text{m}^3$ in winter, and around 100 $\mu\text{g}/\text{m}^3$ for PM2.5 (particulate matter with aerodynamic diameter less than or equal to 2.5 micrometers) in the autumn (Wei et al., 1999; Cao et al., 2003; Cao et al., 2004). These high concentrations of suspended particles create low visibility and greatly affect the regional radiative budget (Wu et al., 2005). During the long winter dry season, air masses are mainly northeasterly bringing continental pollution into the Pearl River Delta region and Hong Kong (Gnauk et al., 2008). The consequent effects on visibility and health have gradually appeared due to continuous bad air. The Hong Kong Environmental Protection Department (EPD, 2004) reported that increases of 10 $\mu\text{g}/\text{m}^3$ concentration of NO_x , SO_2 , RSP and ozone, causes associate diseases such as respiratory, chronic pulmonary and cardiovascular heart diseases to increase by 0.2% to 3.9%. Ko et al. (2007) demonstrated the air pollution has an adverse effect on hospital admissions for chronic obstructive pulmonary disease in Hong Kong, especially during the winter season. Wong et al. (1999) also found significant associations between hospital admissions for all respiratory diseases, all cardiovascular diseases, chronic obstructive pulmonary diseases, and heart failure and the concentrations of all four pollutants: nitrogen dioxide (NO_2), sulphur dioxide, ozone (O_3) and PM10 in Hong Kong. Moreover, almost 60 days in 2004 suffered from very low visibility which is defined as less than 8km (Business Environment Council, 2005). This not only affects marine and air navigation, but Hong Kong is also losing its status as an international city.

It is likely that the largest proportion of Hong Kong's pollution originates from adjacent rapidly industrializing areas of the Chinese mainland, but with only 16 air quality stations, the occurrence and intensity of trans-boundary air pollution is difficult to establish. For example, although Lo et al. (2006) emphasize the importance of cross-boundary air pollution from the Chinese mainland, and Yuan et al. (2006) affirm that 60-70% of PM10

came from outside Hong Kong, recently Civic Exchange (2007) maintains that local sources are dominant 53% of the time.

Government action on air quality monitoring has involved the setting up of a grid of air quality monitoring stations in nearby Guangdong province and Hong Kong territories, with thirteen stations deployed in the province and three in Hong Kong, they are Tung Chung, Tsuen Wan and Tap Mun stations. Since these are single point measurements and lack regional coverage, satellite images can potentially play an important role in regular and continuous air quality monitoring over the Hong Kong region.

3.2. Data used

3.2.1. AERONET

The AErosol RObotic NETwork, AERONET (Holben et al., 1998) is a federated network of ground sunphotometers, of which there are over 400 sites around the world. An AERONET station consists of a Cimel sunphotometer which measures the aerosol extinction every 15 minutes using multiple wavelengths (Figure 3.2), a solar panel and a controller. It provides real-time aerosol optical thickness, precipitable water, inversion products including size distribution, single scattering albedo and refractive index based on the solutions of radiative transfer equations. There are three levels of data: 1, 1.5 and 2 which present the raw data, cloud-screened data, and cloud-screened and quality-assured data, respectively. In order to collect our local aerosol data, as well as sharing the parameters for MODIS image calibration with other users globally, two AERONET stations was established in the Hong Kong Polytechnic University in 2005 and 2007.



Figure 3.2. AERONETs deployed on the a. library roof of the Hong Kong Polytechnic University, b. remote peninsula in the southeast of Hong Kong island

3.2.1. MODIS

The MODerate resolution Imaging Spectroradiometer (MODIS) is a sensor aboard the TERRA and AQUA satellites. TERRA is the satellite launched in 1999 which passes from north to south in the morning (ca. 10:30 a.m. local time) and AQUA is the satellite launched in 2001 which passes from south to north in the afternoon (ca. 1:30 p.m. local time). With 36 wavebands, MODIS (Figure 3.3) can be fully used for atmospheric, oceanic and land studies at both global and local scales. Images are in true colour, at 250m, 500m and 1km resolution, as well as specific products such as atmospheric aerosol, oceanic chlorophyll index, land cover map and fire product (Justice et al., 2002). However, in this project, MODIS level 1B calibrated reflectance images and MODIS level 2 aerosol products will mainly be used. The aerosol product, which is based on using a Look Up Table of particle sizes and the spectral wavelength, has been identified as having a large error for the southeast China region (Kaufman and Tanré, 1998). In addition, because the particle scattering characteristics and radiation levels in the south China region are significantly different from global averages (as given in global Look Up Tables), there is a need to develop a regional Look Up Table for regional air quality modeling in Hong Kong and the PRD region.

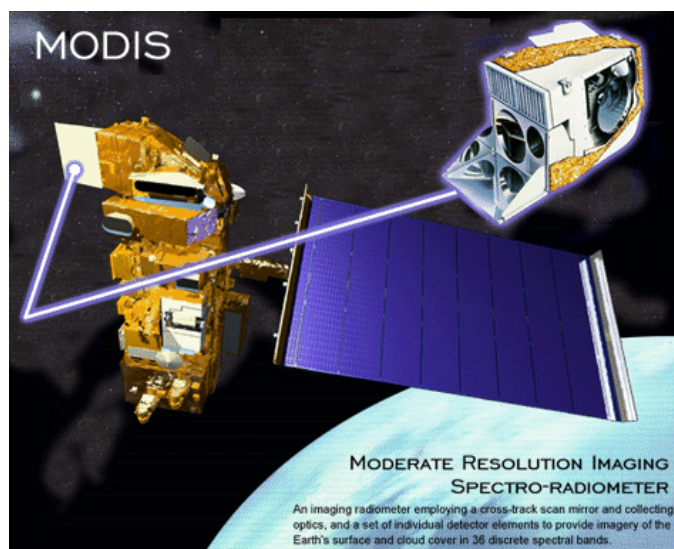


Figure 3.3. MODIS sensor

(adopted from MODIS: http://science.nasa.gov/headlines/y2001/ast21aug_1.htm)

In this study, the 500m resolution TERRA/MODIS level 1B calibrated reflectance (MOD02HKM) and MODIS level 2 aerosol products (MOD04) were collected. Validation was undertaken by comparing the retrieved AOT from our study with AERONET and MicrotopsII data. MicrotopsII sunphotometer is a portable and relatively low cost sunphotometer which measures AOT at 5 wavelengths (440nm, 500nm, 675nm, 870nm and 936nm). In order to validate the surface reflectance estimated from the modified MRT method, the MODIS surface reflectance products (MOD09 8-days composite surface reflectance images) were also acquired from NASA Goddard Earth Science Distributed Active Archive Center (DAAC) for year 2007. The MOD09 images were temporally averaged. The resolution was resampled from 1km to 500m using bilinear interpolation method for comparing with seasonal MRT images at 500m resolution. The MOD09 images are corrected for aerosol, gases and water vapour using the inputs of MODIS atmospheric data. Their surface reflectances are validated with 150 AERONET stations and are considered acceptable if the data error lies within $\pm 0.005 + 0.05 \cdot \rho$ (ρ is surface reflectance) (Vermote and El Saleous, 2006). In addition, field measurements of surface reflectance over Hong Kong using Cropsan MSR-16R multispectral radiometer (MSR) have been measured in 2006.

CHAPTER 4.

AEROSOL OBSERVATIONS IN HONG KONG AND THE PEARL RIVER DELTA REGION

4.3. MODIS collection 4 and 5 data versus AERONET measurements

This chapter presents an evaluation of collection 4 and 5 MODIS aerosol products using AERONET measurements in Hong Kong. TERRA/MODIS and AQUA/MODIS level 2 aerosol products (MOD04) were collected for the years 2000 to 2007. Since AERONET has been deployed in Hong Kong since 2005, temporally matched data with the criteria of overpass time ± 30 minutes was collected from 2005 to 2007. The area of $(0.1^\circ)^2$ degree (11km x 11km) around the AERONET location (Hong Kong PolyU site) was extracted from MODIS AOT images for calculating the average image AOT (Figure 4.1)

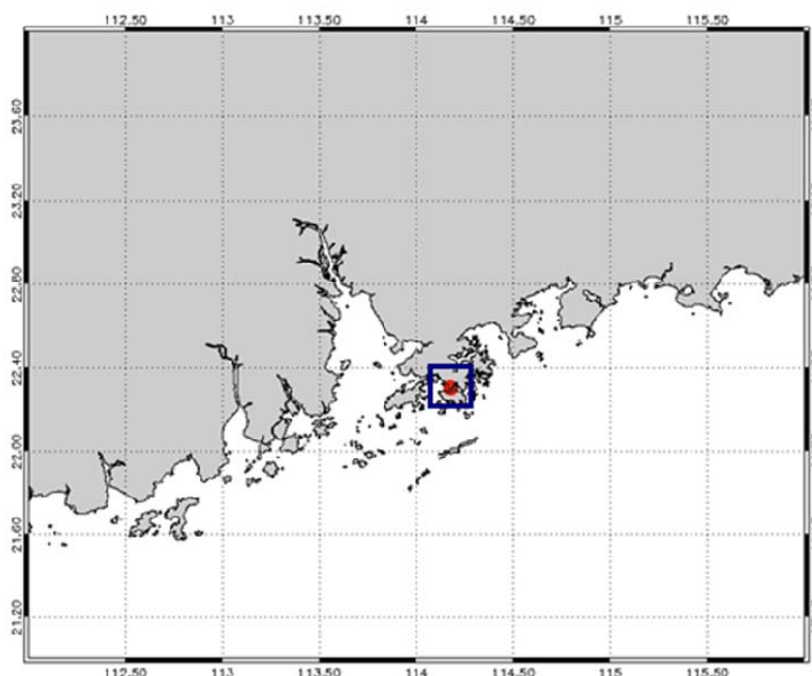


Figure 4.1. Area of interest around AERONET station

The MOD04 collection 4 and 5 AOT data at 10km resolution were compared with AERONET (Figure 4.2a, b). However, there are only 24 MOD04 collection 4 data in the NASA GSFC database in 2007 since the collection 4 data was replaced with collection 5 data over the period of this study, and there are 108 matched daily data from the AERONET (Hong Kong PolyU) station in 2007. Good agreements are shown between the MOD04 collection 4 AOT ($r^2 = 0.671$) and MOD04 collection 5 AOT ($r^2 = 0.778$). The collection 5 AOT performs statistically better than collection 4 in terms of smaller bias, Root Mean Square Error (RMS), Mean Absolute Difference (MAD). The bias, RMS, MAD errors of collection 5 AOT are 0.011, 0.167, 0.129 respectively (Table 4.1).

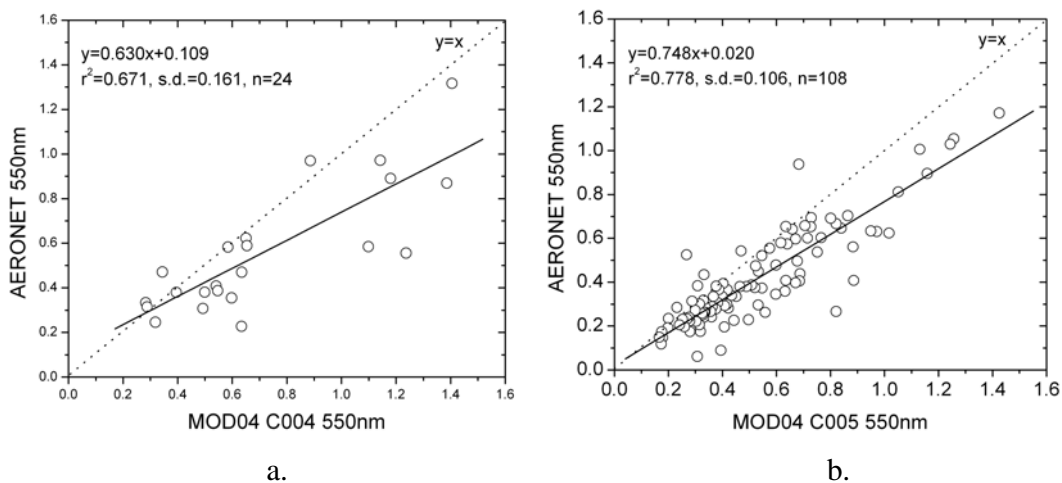


Figure 4.2. Scatter plots, a. between MOD04 collection 4 with AERONET measurements; b. between MOD04 collection 5 with AERONET measurements (r^2 stands for correlation coefficient; s.d. stands for standard deviation; n stands for number of samples)

	Correlation (r^2)	Bias estimator ($E(S^2)$)	Root-Mean-Square Error (RMS)	Mean Absolute Difference (MAD)	Number of samples (n)
MOD C004	0.671	0.032	0.249	0.174	24 (on year 2007)
MOD C005	0.778	0.011	0.167	0.129	108 (on year 2007)

Table 4.1. Statistical comparison between the performances of collection 4 and collection 5, with AERONET data

Similar accuracies were found in China where Li et al. (2007) found of correlations are 0.436 and 0.706 for collection 4 and collection 5 data respectively compared with “in-situ” hazemeter measurements. Since collection 4 operates with a DDV algorithm which makes use of the aerosol loading on different spectral wavelengths, desert areas, bright surfaces and complex land surfaces such as urban areas would have a poor correlation. Significant improvement of collection 5 was observed, with higher correlation, and also higher spatial continuity of AOT between land mode and ocean modes (Figure 4.3).

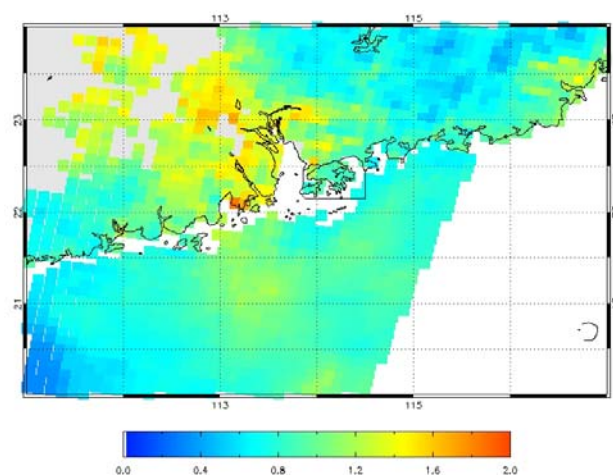
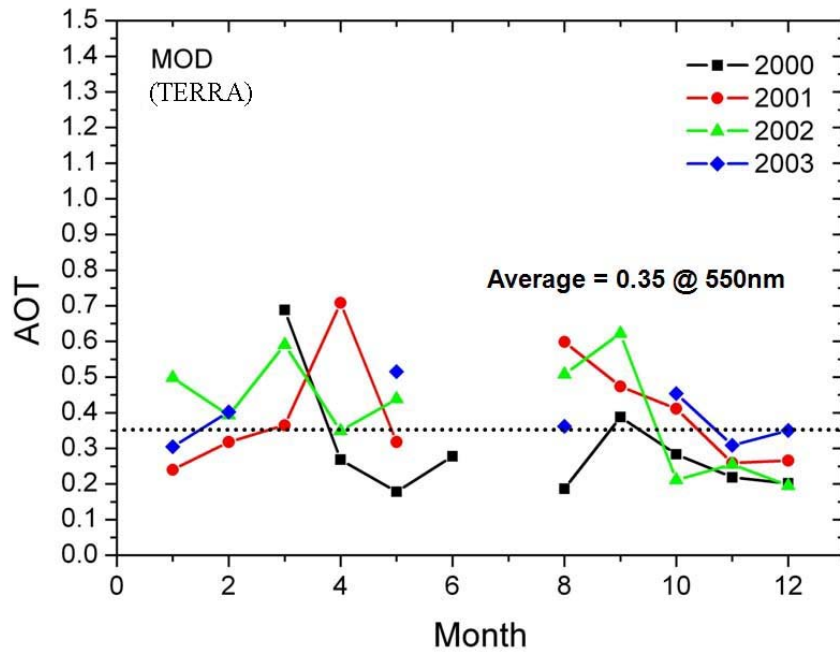


Figure 4.3. Collection 5 AOT derived from land and ocean algorithms (the missing areas are covered by clouds and scanned by other swath)

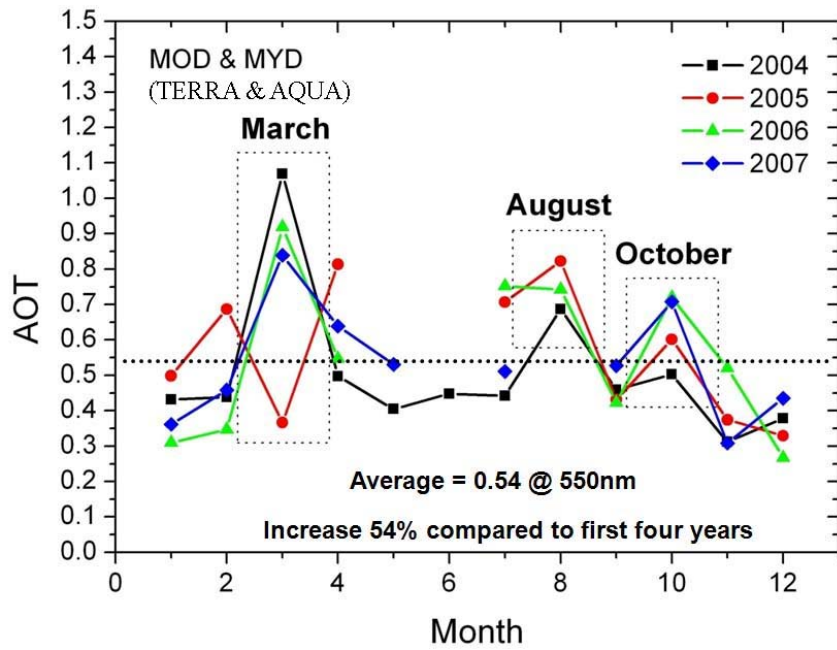
Although the collection 4 and collection 5 AOT data have high correlations and small bias, RMS and MAD values, its 10km spatial resolution limits its application to city-scale monitoring. Also, the high reflectance areas (eg. urban areas) are always masked out with no AOT values due to not meeting the surface reflectance criteria. Thus, there is a need to develop a methodology which can work on high and low reflectances at more detailed spatial resolution.

4.4. Seasonal and yearly variations of AOT from MODIS images

Section 4.1 demonstrated the accuracies of aerosol retrieval for collection 4 and 5 products which are reasonable and thus this section will discuss the seasonal and yearly variations of AOT over Hong Kong using TERRA and AQUA data. The area of $(0.1^\circ)^2$ degree (11km x 11km) around the AERONET location was also extracted from MODIS AOT images (Figure 4.1). Figure 4.4 shows that the average AOT between 2000 and 2003 is ca. 0.35 at 550nm and this was increased by 54% (to 0.54 at 550nm) between 2004 and 2007. The months of March, August and October (Figure 4.4b) show higher AOT concentrations as peaks over the year. In March and October, the pollutants are often trapped in Hong Kong due to low wind speeds caused by the changes of monsoon wind direction (Wong et al., 2007). In August, the hottest and sunniest month in Hong Kong, secondary aerosols from photochemical reactions are easily formed. Secondary aerosol is defined as the aerosol produced by atmospheric gases reacting and condensing from gas to particle conversion. PM_{2.5}, PM₁₀ and Carbon monoxide (CO) can be good indicators for the measurements of secondary aerosol (Chang and Lee, 2007) but this is beyond the scope of our study. Since the AERONET station in Hong Kong PolyU has operated since September 2005 and there is insufficient data during summer due to the instrument calibration taking place at NASA, similar seasonal analysis cannot be undertaken using AERONET data.



a.



b.

Figure 4.4. AOT seasonal and yearly variations, a. between 2000 and 2003, b. between 2004 and 2007 (MOD stands for TERRA satellite; MYD stands for AQUA satellite)

The AOT variation in 2006 between Hong Kong and Guangzhou is illustrated in Figure 4.5. March and October are still also identified as the months with the highest AOT and the peaks over the year (points within the black box). It is obvious that Guangzhou has much higher AOT (~ 62%) than Hong Kong, the annual mean AOT levels observed in Hong Kong and Guangzhou are 0.535 and 0.867 respectively. The heavy industrialization and geographical location of Guangzhou as an inland city, along with the higher aerosol concentration from power plants and industries, explains the higher AOT levels whereas the dominant source of pollutants in Hong Kong is from the vehicles.

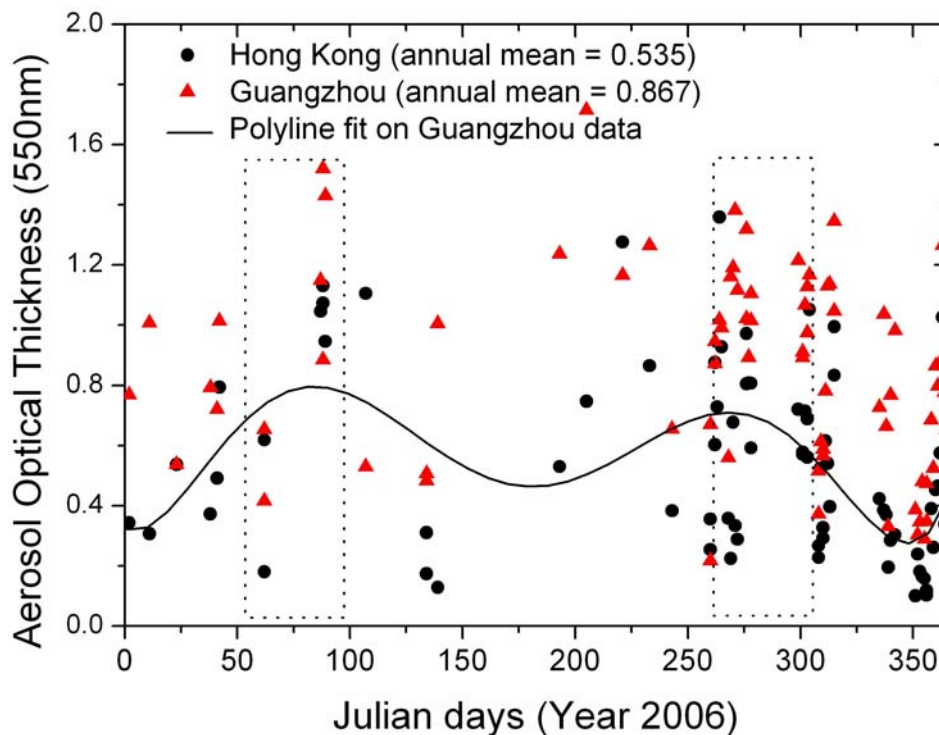


Figure 4.5. Daily AOT variation in 2006, between Hong Kong and Guangzhou

Comparisons were also made between the Hong Kong AERONET station and other urban stations worldwide, with for example a mean AOT of 0.69 for the 440nm band, compared with 0.57 for Beijing, 0.55 for Singapore, 0.22 for Rome, and 0.24 for Goddard Space Flight Center show Hong Kong AOT levels to be significantly higher than the other places.

CHAPTER 5.

METHODOLOGY

A new methodology is described here for aerosol retrieval from MODIS 500m data. The algorithm is designed for application over complex land surface areas such as Hong Kong and the Pearl River Delta region. Five MODIS 500m channels and two MODIS 250m channels were acquired in the study for aerosol retrieval, as well as cloud and water masking. Figure 5.1 shows a logical flow chart for the development of the AOT retrieval method.

First, the AERONET data (2005 to 2007) from the Hong Kong PolyU station was acquired and clustered to four different aerosol models. The aerosol models coupled with relative humidity data and different viewing geometries were input into radiative transfer model for building Look Up Tables. To minimize the computer memory, the specific relative humidity was first retrieved and LUT geometry was interpolated to the specific satellite geometry. Finally, the simulated aerosol reflectances and TOA reflectances as function of AOT were created.

Second, the MODIS 500m calibrated reflectance images in 2007 were acquired from NASA DAAC. Geometric correction, reprojection, cloud and water screening, viewing angles screening and Rayleigh correction were first applied to the images. The modified Minimum Reflectance Technique was then applied to the MODIS 500m images to create surface reflectance images. The derived surface reflectance images were validated with field measurements and MODIS surface reflectance products (MOD09).

Third, the aerosol reflectances derived from MODIS were checked with modeled aerosol reflectances from LUTs using spectral fitting technique. The aerosol model with minimum residual would be selected and the corresponding aerosol reflectance and AOT values would be obtained. Finally, the AOT images at 550nm were derived.

Four, the derived AOT images were compared with AERONET and MicrotopsII measurements. Statistical estimators including correlation coefficient, bias estimator, RMS and MAD errors were used to examine the accuracy.

More discussion and explanation will be given in the following sections.

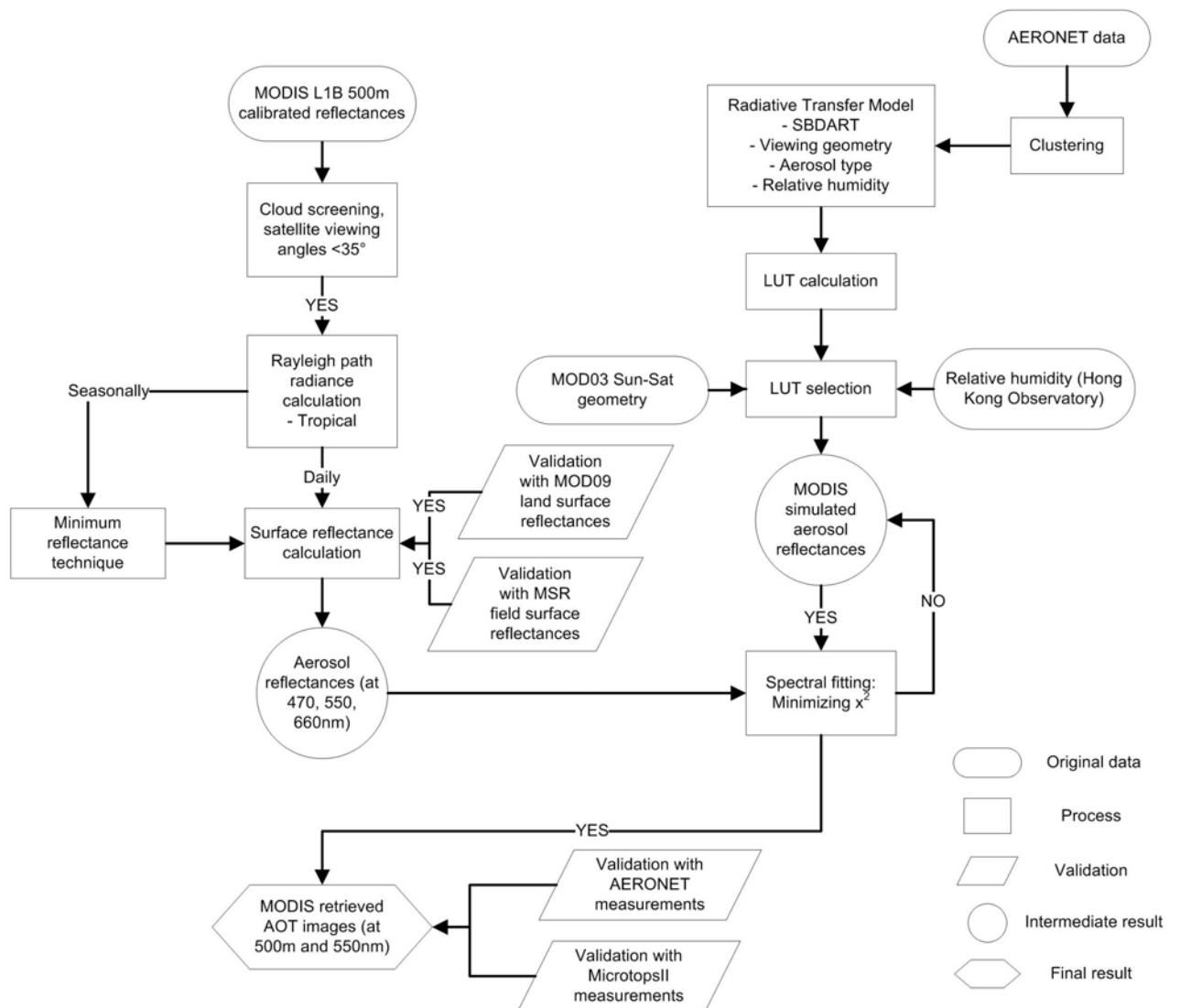


Figure 5.1. The schematic diagram for aerosol retrieval in the study

The rationale of the proposed aerosol retrieval algorithm is to determine the aerosol reflectance by decomposing the Top Of Atmosphere (TOA) reflectance from surface reflectance and the Rayleigh path reflectance. The TOA reflectance $\rho_{TOA}(\theta_0, \theta_s, \phi)$ is expressed as (Kaufman et al., 1997):

$$\rho_{TOA}(\theta_0, \theta_s, \phi) = \rho_{ATM}(\theta_0, \theta_s, \phi, \tau_{Aer}, \tau_{Ray}, pr(\theta), \omega_0) + \frac{\Gamma_{Tot}(\theta_0) \cdot \Gamma_{Tot}(\theta_s) \cdot \rho_{Surf}(\theta_0, \theta_s)}{1 - \rho_{Surf}(\theta_0, \theta_s) \cdot r_{Hem}(\tau_{Tot}, g)} \quad \text{Eq 5.1.}$$

where θ_0 is the solar zenith angle, θ_s is the satellite zenith angle, ϕ is the azimuth angle, τ_{Aer} , τ_{Ray} and τ_{Tot} are aerosol optical thickness, Rayleigh optical thickness, and total optical thickness respectively. $pr(\theta)$ is the phase function, ω_0 is a single-scattering albedo, g is the asymmetry parameter, ρ_{ATM} is the atmospheric path reflectance, $\Gamma_{Tot}(m_0)$ is the total transmittance, $\rho_{Surf}(\theta_0, \theta_s)$ is the surface reflectance, and $r_{Hem}(\tau_{Tot}, g)$ is the hemispheric reflectance.

5.1. Rayleigh correction of TOA images

Before applying the Rayleigh correction to each MODIS 500m (MOD02HKM) image, the Region Of Interest (ROI) is first defined for the area of the Pearl River Delta region and Hong Kong to reduce the data volume. All the ROI extracted images were then geometrically corrected to the World Geodetic System 1984 (WGS84) latitude and longitude coordinate system using the MOD03 geolocation data. The “bow-tie” effect caused by the overlap of the satellite field of view from two granules was then corrected using MODIS Reprojection Tool - Swath (MRTSwath) which is provided by NASA Land Processes Distributed Active Archive Center (LP DAAC) for geometric correction, re-projection and correction for oversampling between scans (MRTSwath, 2006). The MRTSwath software is run in Linux system. The MOD02HKM and MOD03 geolocation data were resampled, spatially averaged and re-projected to 500m resolution.

Rayleigh correction is important because it corrects for the finer particles with diameter less than $0.1\mu\text{m}$ which scatters in shorter wavelengths. In the visible wavelengths, particles with diameter larger than $0.1\mu\text{m}$ also scatter and adsorb, and there is notably more scattering when the particle size is similar to the visible wavelength (Mie theory: Mie, 1908).

The determination of Rayleigh path reflectance is based on the computation of spectral dependence of the Rayleigh optical thickness and phase function. Equation 5.2 is adopted for calculating the Rayleigh scattering optical thickness (Bucholtz, 1995).

$$\tau_{Ray}(\lambda) = A \cdot \lambda^{-(B+C\lambda+D/\lambda)} \cdot \frac{p(z)}{p_0} \quad \text{Eq 5.2.}$$

where A, B, C, D are the constants of the total Rayleigh scattering cross-section and the total Rayleigh volume scattering coefficient at standard atmosphere. The coefficient values of B, C, and D are variable for different wavelengths, and the coefficients of A take account of seasonal and latitudinal variations (Table 5.2): Tropical (15°N), Midlatitude Summer (45°N , July), Midlatitude Winter (45°N , January), Subarctic Summer (60°N , July), Subarctic Winter (60°N , January), and 1962 U.S. Standard Atmosphere. In this study the Tropical coefficients of A is adopted since Hong Kong is located at the sub-tropical latitude of 22°N .

coefficient	Wavelength λ	
	0.2 - 0.5 μm	> 0.5 μm
B	3.55212	3.99668
C	1.35579	0.00110298
D	0.11563	0.0271393

Table 5.1. Coefficients of B, C, D in Rayleigh scattering (Bucholtz, 1995)

	Wavelength λ	
	0.2 - 0.5 μm	> 0.5 μm
Tropical	0.00652965	0.00868094
Midlatitude Summer	0.00651949	0.00866735
Midlatitude Winter	0.00653602	0.00868941
Subarctic Summer	0.00648153	0.00861695
Subarctic Winter	0.00649997	0.00864145
1962 U.S.Standard	0.00650362	0.00864627

Table 5.2. Coefficients of A in Rayleigh scattering (Bucholtz, 1995)

$p(z)$ is the pressure relevant to the height which was determined by the parameterized barometric equation (Equation 5.3), the unit of $p(z)$ is pascal.

$$p(z) = p_0 \cdot \exp\left[\frac{-29.87 \cdot g \cdot 0.75 \cdot z}{8.315 \cdot (T_{SURF} - g \cdot 0.75 \cdot z)}\right] \quad \text{Eq 5.3.}$$

where g is the gravity acceleration (9.807 ms^{-2}), T_{surf} is the surface temperature (acquired from the Hong Kong Observatory) (e.g. 298K) and p_0 is the actual pressure in mean sea level (1008 Pa) and z is the height (meter). A Digital Elevation Model (DEM) in MOD03 geolocation data was used for estimating the height z and for calculating the pressure $p(z)$ for each pixel.

In the calculation of Rayleigh reflectance, the air mass factor should be defined to normalize the attenuation of optical path length relative to that at the zenith. The air mass is 1 at the zenith and it can reach 38 at the horizon. In this study, the air mass calculation proposed by Kasten and Young (1989) is adopted (Equation 5.4):

$$X = \frac{1}{\cos(\theta) + 0.50572(96.07995 - \theta)^{-1.6364}} \quad \text{Eq 5.4.}$$

where θ is the solar zenith angle

The Rayleigh optical thickness can be calculated using Equation 5.2 and it is then corrected for temperature (Equation 5.5):

$$\tau_{correct-Ray}(\lambda) = \tau_{Ray}(\lambda) \cdot \frac{T_0}{T} \quad \text{Eq 5.5.}$$

where T_0 is the surface temperature acquired from the Hong Kong Observatory (eg. T_0 is 273K), $T = 298 - 9.81 \cdot 0.75 \cdot z$ (where 0.75 is lapse rate)

Then the atmospheric transmittance can be computed by Equations 5.6 and 5.7:

$$\Gamma_{Sat} = \exp(-\tau_{Ray} \cdot X(\theta_{Sat}) \cdot \frac{P}{P_0}) \quad \text{Eq 5.6.}$$

$$\Gamma_{Sun} = \exp(-\tau_{Ray} \cdot X(\theta_{Sun}) \cdot \frac{P}{P_0}) \quad \text{Eq 5.7.}$$

where Γ_{Sat} = atmospheric transmittance along the path from ground to sensor and Γ_{Sun} = atmospheric transmittance along the path from the sun to ground, $X(\theta_{sat})$ is the air mass along the path from ground to sensor and $X(\theta_{Sun})$ is the air mass along the path from sun to ground

The Rayleigh optical thickness for multiple scattering (Deepak et al., 1980) can also be calculated with Equation 5.8:

$$\tau_{multi-ray} = \frac{\frac{1}{2} \cdot \Gamma_{Sat} \cdot \Gamma_{Sun} \cdot (0.02 \cdot \tau_{correct-ray} + 1.2 \cdot (\tau_{correct-ray})^2)}{X(\theta_{Sun})^{\frac{1}{4}} \cdot X(\theta_{Sat})^{\frac{1}{4}}} \quad \text{Eq 5.8.}$$

After calculating the Rayleigh optical thickness for multiple scattering and the temperature and pressure corrected Rayleigh optical thickness, the nadir reflection by Rayleigh scattering can also be calculated:

$$R_{nadir} = \pi \cdot (\tau_{multi-ray} + \tau_{correct-ray}) \cdot pr \quad \text{Eq 5.9.}$$

where R_{nadir} = nadir reflection by rayleigh scattering, pr is the phase function (Bucholtz, 1995), $\tau_{multi-ray}$ is the Rayleigh optical thickness for multiple scattering, $\tau_{correct-ray}$ is the temperature and pressure corrected Rayleigh optical thickness.

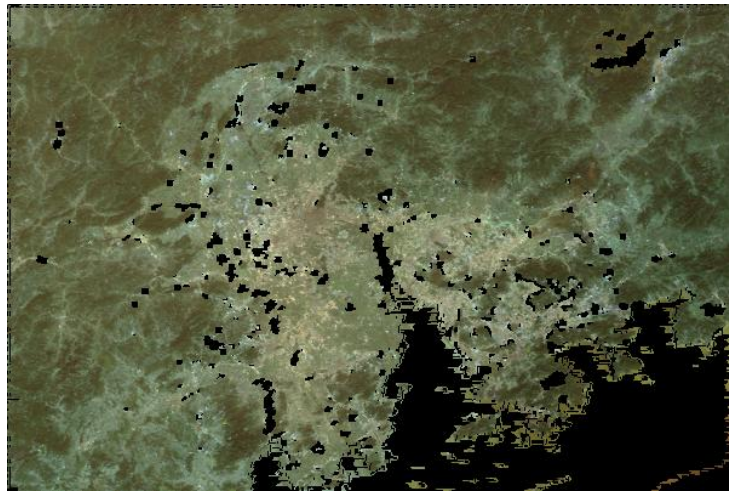
Finally, the Rayleigh reflectance can be obtained by geometric correction of R_{nadir} (Equation 5.10):

$$\rho_{Ray} = R_{nadir} \cdot \left(\frac{P}{P_0} \cdot X(\theta_{Sat})\right) \cdot \left(\frac{P}{P_0} \cdot X(\theta_{Sun})\right) \quad \text{Eq 5.10.}$$

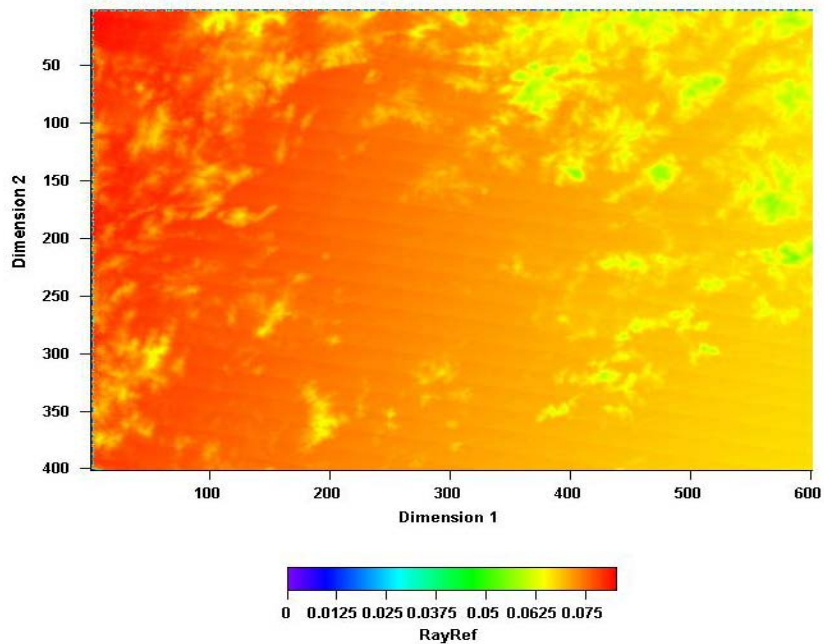
Figure 5.2a shows an example of the TOA reflectance image and Figure 5.2b depicts the Rayleigh corrected reflectance image after water and cloud masking. Figure 5.2c shows the Rayleigh scattering reflectance at 470nm.



a.



b.



c.

Figure 5.2. a. TOA reflectance image b. Rayleigh corrected reflectance image (masked with water and clouds) and c. Rayleigh reflectance image at 470nm

Water and clouds are also masked during the Rayleigh correction. The water is masked based on the land mask data in the MOD03 geolocation data (Equation 5.11). There are 8 different classes of water and land masking, listed below:

MODIS Land Mask

- 0: Shallow Ocean (< 5km from Coast, < 50m deep)
- 1: Land
- 2: Ocean coast line & lake shoreline
- 3: Shallow Inland Water (< 5km from Shore, < 50m deep)
- 4: Ephemeral (intermittent) Water
- 5: Deep inland Water (> 5km from Shore, > 50m deep)
- 6: Moderate/Continental Ocean (> 5km from Coast, > 50m deep)
- 7: Deep Ocean (> 500m deep)

If (land mask > 1 or = 0) or (reflectance at 660nm < 0.08) or (satellite zenith angle > 70)
then mask Eq 5.11.

Since there is no high resolution thermal band in MODHKM (500m) data, a tailor-made cloud-masking algorithm is proposed for this study by making use of three visible channels and an NDVI band. This algorithm tests the brightness of reflectance for each pixel, with thresholds set based on a trial-and-error approach (Equation 5.12):

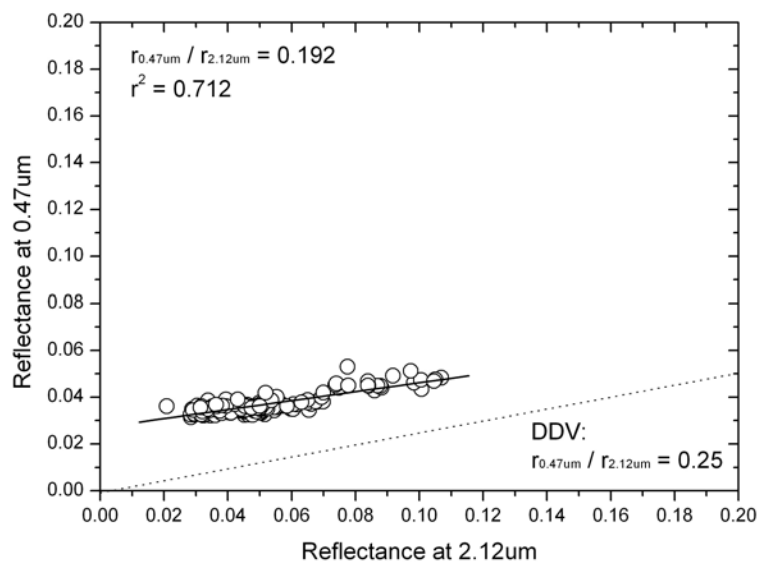
If (reflectance at 470nm > 0.2) or (reflectance at 550nm > 0.2) or (reflectance at 660nm > 0.2) or (NDVI < -0.5) then mask Eq 5.12.

5.2. Derivation of surface reflectance images

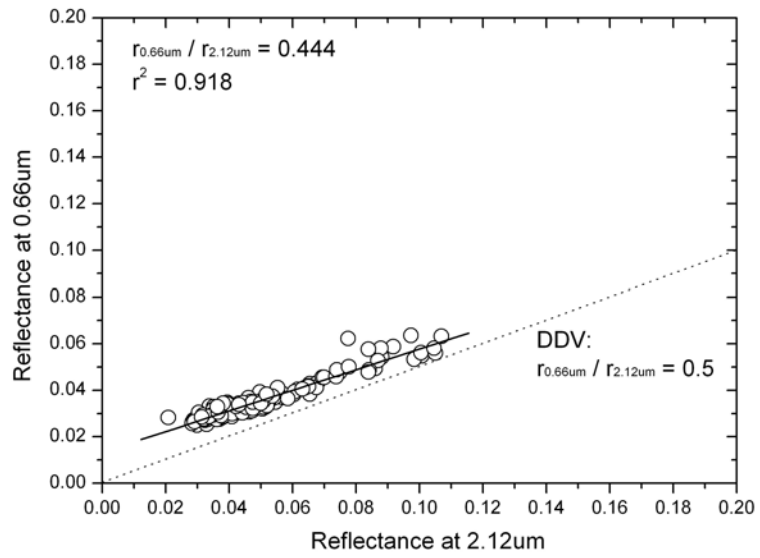
Aerosol retrieval from satellite remotely sensed images basically aims to distinguish the attenuated radiation by aerosols from that of reflection from the surface. The procedure is complex because ground surface reflectances are difficult to distinguish from the total satellite received signal. The estimation of surface reflectances is thus the key factor in aerosol retrieval. Different approaches for estimation of surface reflectance have been developed in previous studies eg. DDV and Second generation of MODIS operation

algorithms. But as previously stated (Section 2.1), they do not operate over bright surfaces such as deserts and urban areas.

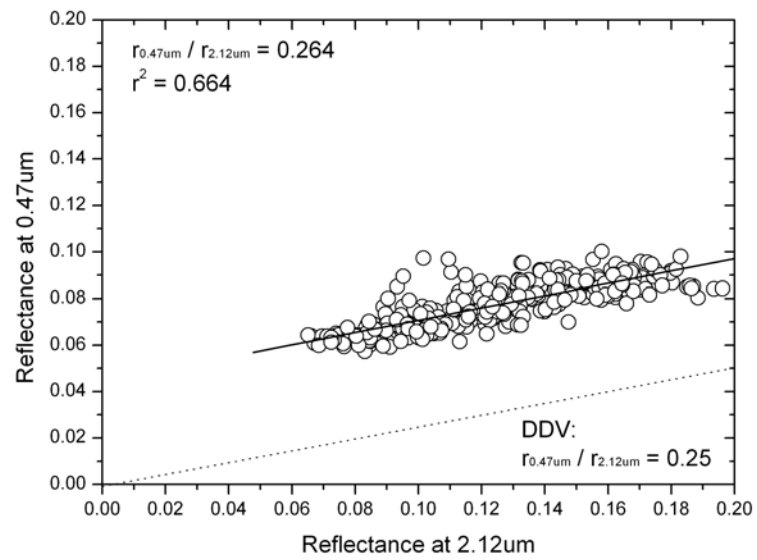
The empirical ratios (DDV) suggested by Kaufman and Tanré (1998) using atmospherically corrected Landsat images between Blue/SWIR and Red/SWIR are 0.25, 0.5, respectively. The assumption they made is the SWIR band is atmospheric-free where the surface reflectance images can be developed by the known relationship between visible bands (Blue and Red) and SWIR band. However, these correlations between bands are highly variable between different vegetation types and different satellite-to-sun geometries. Thus, different studies suggest different ratios, for example: Karnieli et al. (2001) found the ratios were 0.23 and 0.52 over Brazil; Levy et al. (2005) found 0.33 and 0.65 over east coast USA; Lee et al. (2007) found 0.31 and 0.88 during winter over south Korea. In this study, the relationship between the visible and SWIR band is first investigated using the atmospherically-corrected MODIS satellite images (with clear-sky MODIS images which are matched with ground measurements for AOT < 0.2 at 550nm). The band ratios for i. Blue/SWIR and ii. Red/SWIR are computed for both vegetated and urban areas (Figure 5.3). The regions of vegetated and urban areas were selected based on land cover maps created in previous project (Wong et al., 2008).



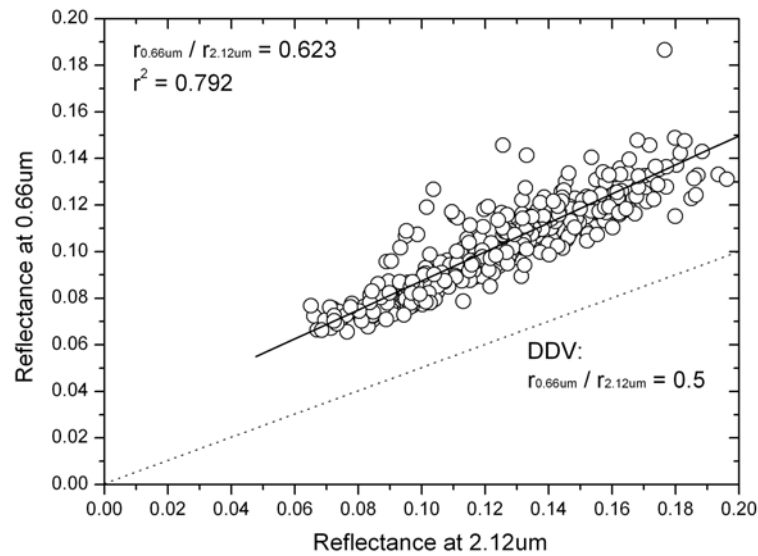
a.



b.



c.



d.

Figure 5.3. Empirical ratios for vegetated areas: a. Blue/SWIR, b. Red/SWIR; Empirical ratios for urban areas: c. Blue/SWIR, d. Red/SWIR

It was found that the differences between the ratios observed for vegetated and urban areas for Blue/SWIR (0.19 and 0.26 for vegetated and urban areas respectively) and for Red/SWIR (0.44 and 0.62 in vegetated and urban areas respectively) are large, it is suggested that the empirical ratios (DDV) method for deriving the surface reflectance for both vegetated and urban areas in Hong Kong is inapplicable. Thus, there is a need to develop a new method which can estimate reflectance of both dark and bright surfaces accurately.

Aerosol retrieval over bright surfaces is challenging because the land surface and atmospheric aerosol contents are not easy to differentiate due to both having high reflectance values. To overcome this difficulty, Herman and Celarier (1997) suggested a new technique the “Minimum Reflectance Technique” (MRT) for retrieving surface reflectance from Nimbus-7/Total Ozone Mapping Spectrometer (TOMS) data. They applied the algorithm to 14.5 years of data to estimate Lambertian surface reflectances at 340nm and 380nm wavelengths and found the absolute accuracy to be within 10% on $1^\circ \times 1.25^\circ$ spatial scale. Koelemeijer et al. (2003) used minimum reflectance technique for

developing a surface reflectance database for 5.5 years of observation the Global Ozone Monitoring Experiment (GOME). The results appeared to agree well with the TOMS database. Although there is no validation for applying the “minimum reflectance technique” to high resolution satellite images, in this study we estimate the surface reflectance using the modified MRT for MODIS images

The basic scheme of the modified MRT is to extract the minimum reflectance values of land surfaces from Rayleigh corrected images over a time period. In this study, an entire year (2007) of MOD02HKM (500m) images were acquired from NASA DAAC. To minimize the effects from land cover changes, seasonal minimum reflectance images were derived based on at least thirty clear-sky images for each of four seasons. Then, the second minimum reflectance values (rather than the actual minimum) were retrieved in order to avoid abnormally low reflectance such as noise or shadow. Figure 5.4 demonstrates the frequency of different surface reflectances from first and second minimum reflectance images in a. autumn season, and b. winter season. It is shown that the numbers of abnormal surface reflectances (lower than 0.015) are significantly decreased on second minimum reflectance images in both autumn and winter. These extreme low values are mostly caused by shadow, and the surface reflectances larger than 0.015 are represented as dense forest (Section 6.2). In addition, only nadir images with satellite viewing angle $< 35^\circ$ have been considered in this study in order to minimize the angular effects caused by Bidirectional Reflectance Distribution Function (BRDF) effect in heterogeneous areas. Figure 5.5 shows the example of MRT surface reflectance images in the autumn season.

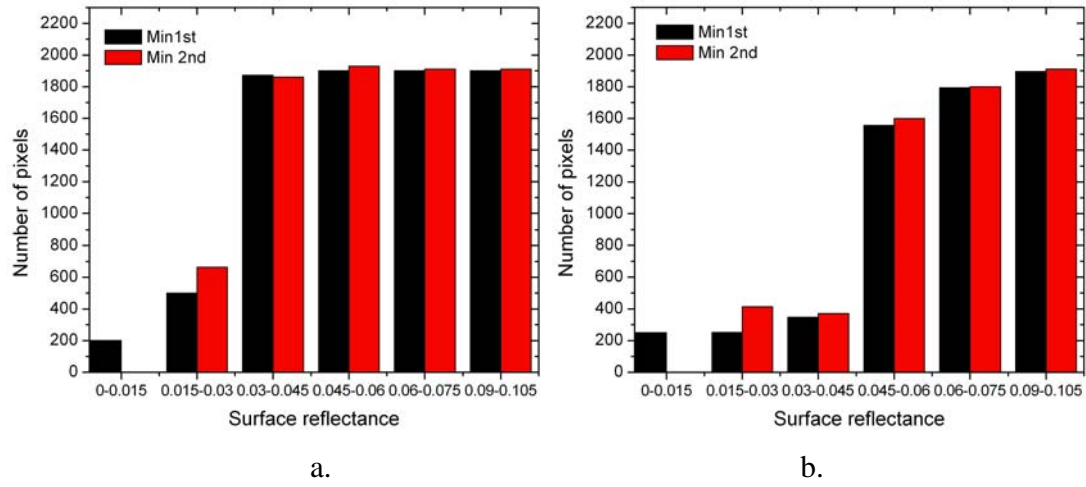
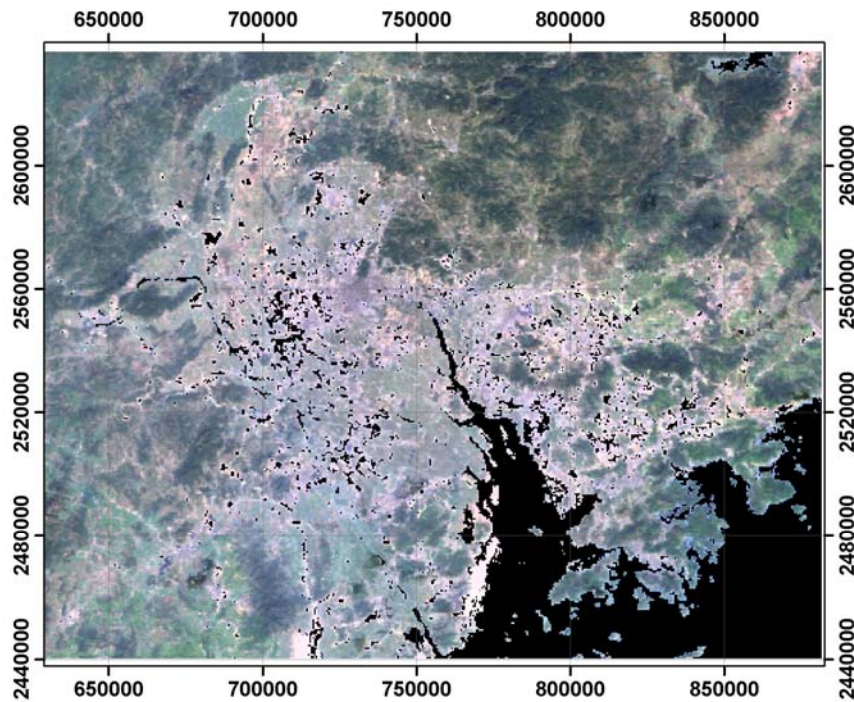
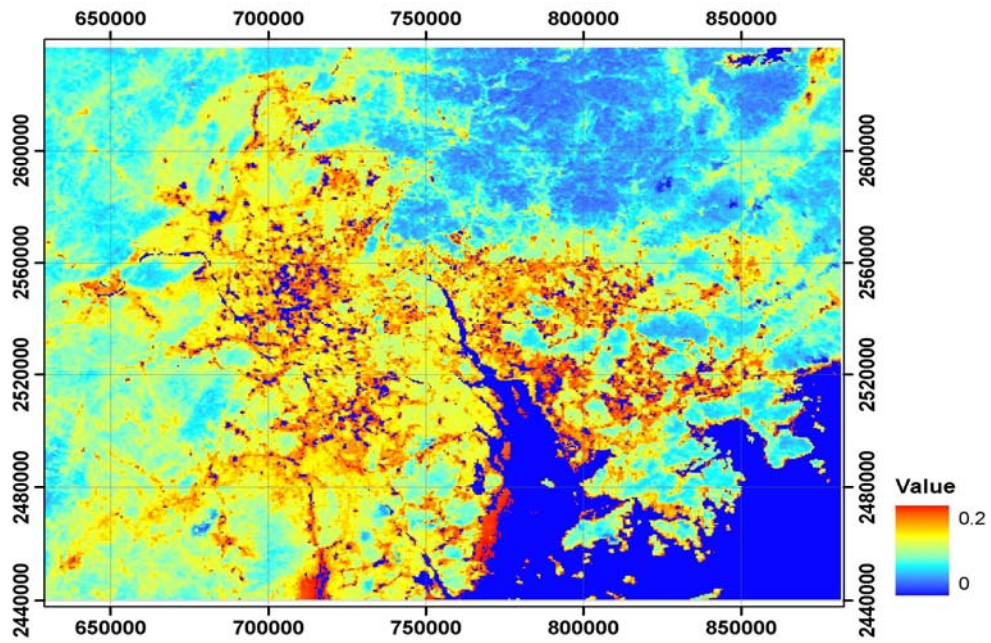


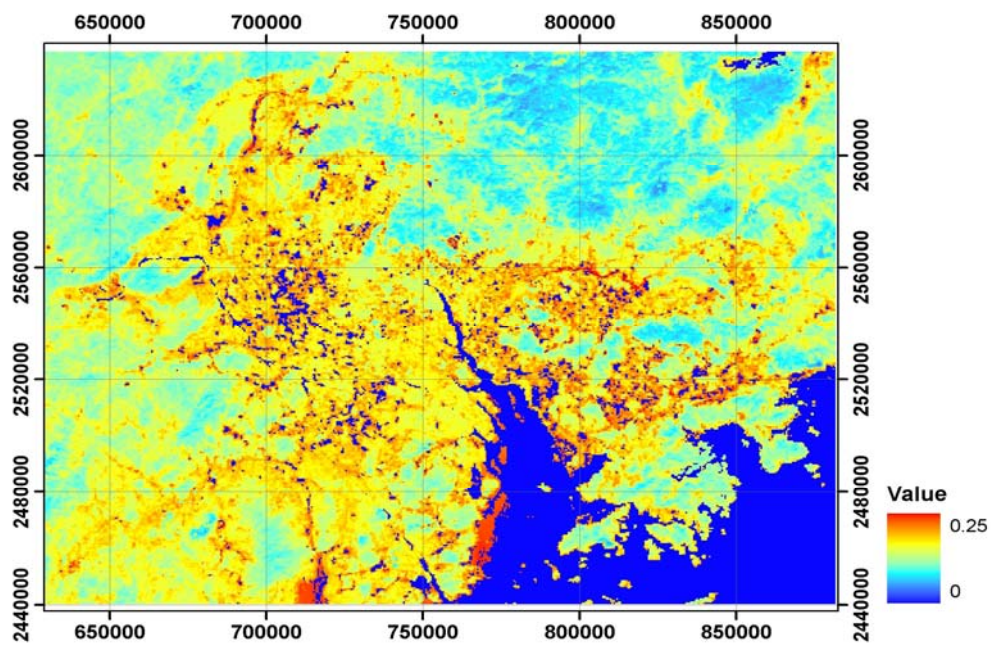
Figure 5.4. Histograms of different surface reflectance values from first minimum reflectance and second minimum reflectance images, a. at 470nm in autumn season, b. at 470nm in winter season



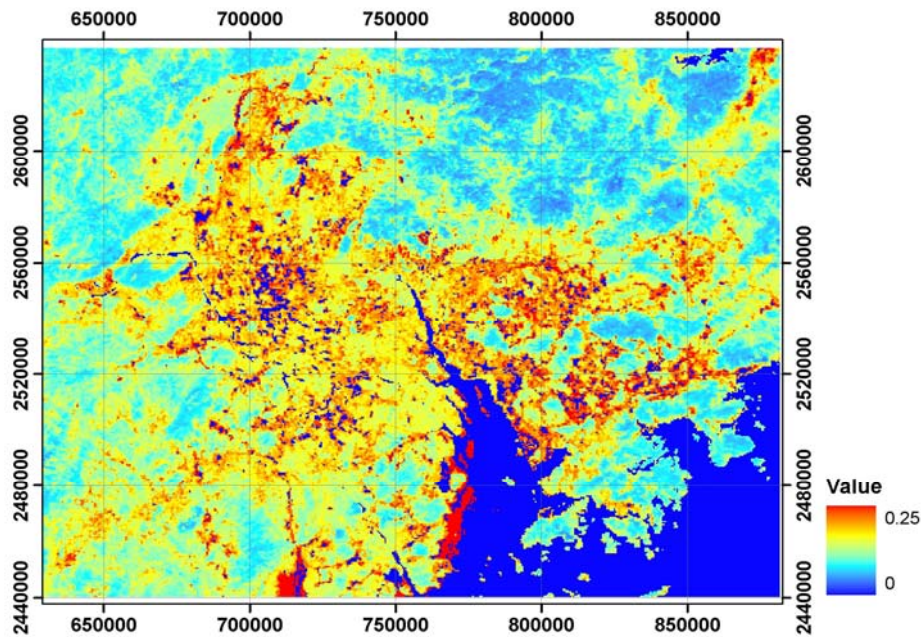
a.



b.



c.



d.

Figure 5.5. Surface reflectance images in the autumn (in UTM grid coordinate system); a. RGB composite of MRT, b. MRT at 470nm, c. MRT at 550nm, d. MRT at 660nm

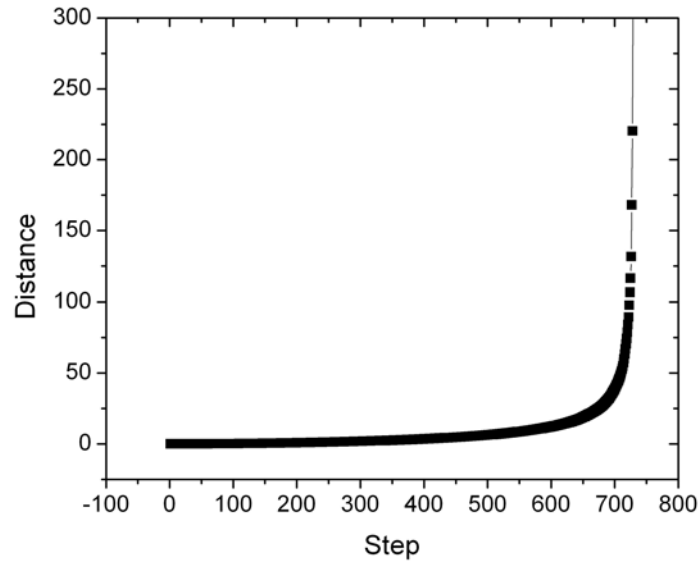
5.3. Look up table construction

The Intergovernmental Panel on Climate Change (IPCC) (2001, 2007) reported that radiative forcing by aerosols is the most uncertain among all other types of estimated radiative forcing. To reduce this uncertainty, there is a need to develop a set of local aerosol models which is tailor-made for specific regional studies. Li et al. (2005) made use of the four default aerosol models in the Second Simulation of a Satellite Signal in the Solar Spectrum (6S) radiative transfer model, namely, dust-like, water-soluble, oceanic, and soot, and determined their fraction of the basic models for each season. Since their experiments and estimation only made use of the satellite data and MicrotopsII measurements in 2001, without the inversion data such as size distribution and Single Scattering Albedo (SSA) from AERONET, the accuracy of the models are questionable.

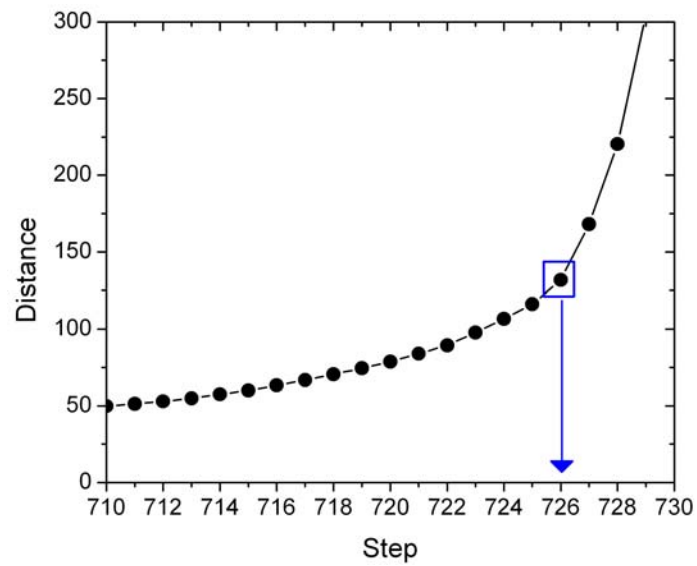
Omar et al. (2005) developed a type-specific set of optical properties of aerosol models using the AOT and inversion data from 200 AERONET stations around the world. They classified six aerosol types geographically, namely, desert dust, biomass burning, polluted continental, clean continental, polluted marine aerosol, and dirty pollution. The technique for classification is based on clustering analysis whose rationale is to group and partition the data based on suggested variables. Twenty-six parameters of aerosol optical properties were adopted during clustering and the relative errors were computed to check the accuracy of each model. In this study, the clustering analysis technique is adopted for classifying the aerosol optical properties.

The K-means clustering analysis was carried out in SPSS statistical software with 24 selected parameters. The aerosol optical properties and AOT from the Hong Kong PolyU AERONET station (from 2005 to 2007) were used for clustering. The rationale of K-means clustering (MacQueen, 1967) is to un-supervise the dataset through a number of clusters and define their centroids. The data points belong to certain groups according to their associations with the nearest centroid. In this study, the number of clusters was first tested by Ward's method (Ward, 1963) under automated hierarchical clustering method, the distance between each step from 0 to 730 (the sample of data) was calculated and shown in Figure 5.6a. The "elbow" or "saturation" point was found at step 726 (Figure 5.6b), therefore, the number of clusters was set as four ($730 - 726 = 4$). The sensitivity tests were also investigated by calculating the distances between cluster centers (Table 5.3), the variability of cluster membership (Figure 5.7), and the scatter plots (Figure 5.8a, b). Table 5.3 shows that cluster 3 is significantly different from the other clusters. Cluster 2 and cluster 4 also appear dissimilar, but the pairs of cluster 1 and 2, cluster 1 and 4 are approximately similar. Figure 5.8a shows the three dimensional scatter plot using SSA_{439nm} , AOT_{500nm} , and coarse mode mean radius. Four clusters are located at the extremities with small overlapping. Figure 5.8b shows the two dimensional scatter plot using coarse and fine mode mean radii, and cluster 3 appears more dissimilar in function of radius. Moreover, the outliers of each cluster can be also identified in Figure 5.7 while there are 4, 4, 2, 5 outliers in cluster 1, 2, 3, 4 respectively. Since the number of outliers is small, they would not be classified as another unique class. Finally, the separability and

robustness of four clusters are demonstrated and the 24 parameters for each cluster are used for building the Look Up Table.



a.



b.

Figure 5.6. Sample distances calculated from hierarchical clustering method, a. a range from 0 to 730, b. a range from 710 to 730

Cluster	1	2	3	4
1		0.734	2.086	0.773
2	0.734		1.370	0.630
3	2.086	1.370		1.735
4	0.773	0.630	1.735	

Table 5.3. Distances between cluster centers

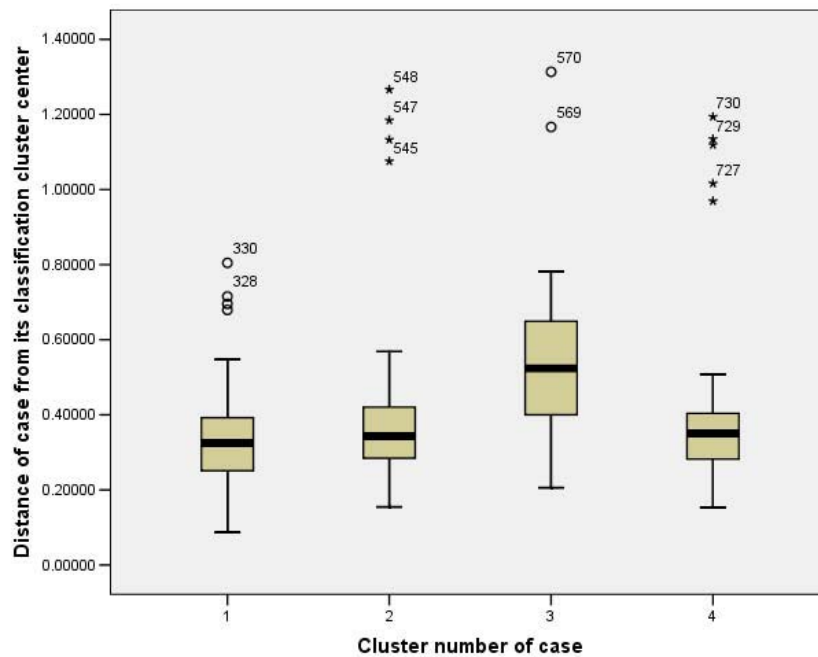


Figure 5.7. Plot of distances from cluster centers by cluster memberships

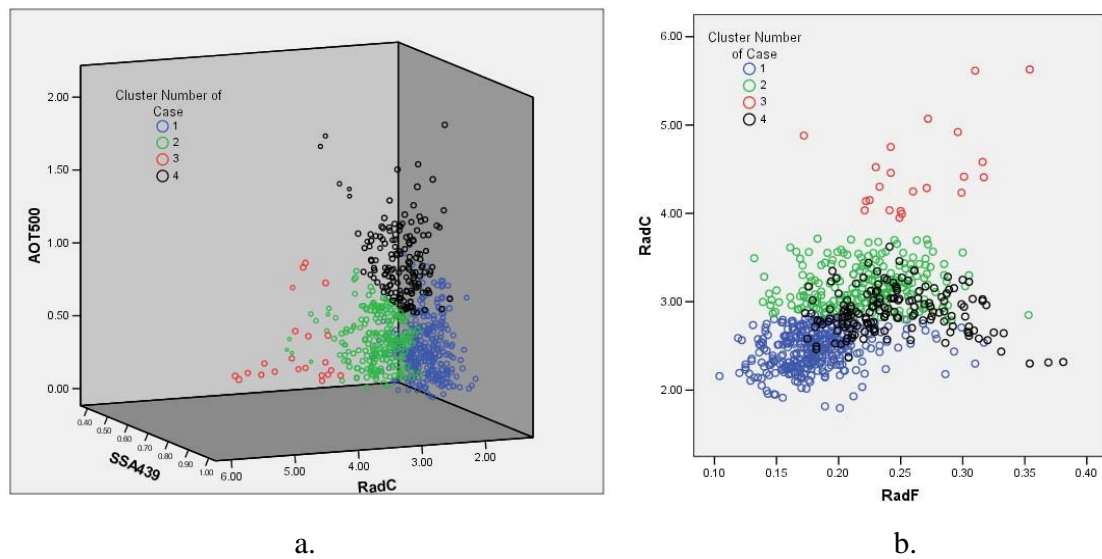


Figure 5.8. Scatter plots, a. three-dimensional scatter plot of four clusters, b. two-dimensional scatter plot of four clusters

After the aerosol optical properties have been classified and local aerosol models have been defined, the LUT is constructed based on the Santa Babara DISORT Radiative Transfer (SBDART; Ricchiazzi et al., 1998) code. A set of aerosol models including solar zenith angles, viewing zenith angles, relative sun/satellite azimuth angles, Relative Humidity (RH) values was input to the LUT construction. The relative humidity is specifically involved during the LUT calculation since Sifakis et al. (1998) found when the RH levels below 60%, water vapour does not contribute to visibility reduction and the AOT detected is wholly due to airborne particulates, not to natural mist. However Hong Kong is a humid city and the size of aerosol always increases with high RH values.

5.3.1. Local aerosol models

In this study, localized and customized aerosol models for Hong Kong are developed using cluster analysis based on AERONET measurements. The classes of natural and anthropogenic aerosol types were determined using 24 parameters from the AERONET

aerosol and inversion products which includes AOT at 500nm (τ_{500}), angstrom exponent ($\alpha_{870-440}$), single scattering albedo at 4 wavelengths, real and imaginary refractive index at the same 4 wavelengths, asymmetry factor, mean radii, standard deviations and total volumes of the coarse and fine mode particles. In total, four aerosol types were identified using a total of 730 cases during 2005 to 2008. They are i. mixed urban, ii. polluted urban, iii. dust, and iv. heavy pollution. Table 5.4 shows the aerosol and microphysical properties, as well as the number of records of each cluster.

	Type 1	Type 2	Type 3	Type 4
Aerosol Optical Thickness (500nm)	0.451	0.518	0.510	1.065
Single scattering albedo (439nm)	0.876	0.869	0.885	0.894
Single scattering albedo (676nm)	0.889	0.874	0.871	0.911
Single scattering albedo (869nm)	0.878	0.857	0.855	0.899
Single scattering albedo (1020nm)	0.872	0.844	0.848	0.888
Real refractive index (676nm)	1.470	1.452	1.500	1.452
Imaginary refractive index (676nm)	0.014	0.022	0.016	0.015
Angstrom coefficient (870nm/440nm)	1.363	1.316	0.952	1.286
Asymmetry factor (676nm)	0.643	0.665	0.683	0.682
Fine mode total volume	0.064	0.081	0.070	0.155
Fine mode mean radius	0.181	0.222	0.262	0.244
Geometric standard deviation (fine)	0.478	0.562	0.644	0.542
Coarse mode total volume	0.055	0.038	0.148	0.066
Coarse mode mean radius	2.458	3.177	4.484	2.892
Geometric standard deviation (coarse)	0.672	0.592	0.504	0.594
Number of records	332	216	22	160

Table 5.4. Summary of the cluster analysis results

The results of clustering show, type 1 (mixed urban aerosol) to have the largest number (45% of total) and type 3 (dust) to have the least number of records (3% of total). This reveals that the Hong Kong AERONET station is more exposed to urban pollution and only a few observations represent desert dust from mainland China. Observations of desert dust may be limited by AERONET being located within the urban area and the topographic effect caused by the high mountains and high rise buildings. Heavy urban pollution (type 4) accounts for 22% of total records, and type 2 (polluted urban aerosol) accounts for 30% of total records. In this classification, there is no cluster representing rural and background aerosols types in Hong Kong, since the AERONET is deployed in the urban area without direct measurements of aerosols from continental areas and without influence from urban and industrial sources.

Type 1 (mixed urban aerosol) has moderate absorption properties (SSA at $0.44\mu\text{m} = 0.88$) and is dominated by both coarse and fine particles (Figure 5.9). Coarse mode most likely originates from sea salt and the fine mode most likely from local urban pollutants. In the existence of these two aerosol types, the absorbing properties could be determined by mixing state of carbonaceous particles. Since the AERONET is located 1km from the coast, the sea salt and local urban pollutant is likely to be mixed, thus we refer to this type as mixed urban aerosol. Type 2 (polluted urban aerosol) has the moderate absorption properties (SSA at $0.44\mu\text{m} = 0.87$) and a high volume of fine particles (0.081), and this type is probably dominated by small black carbon particles which show high absorption properties. In Figure 5.9, type 2 and type 4 show similar size distribution but the former has lower AOT (0.52). We refer to this type as polluted urban aerosol. Dust (type 3) explains relative high AOT ($\tau_{500} = 0.51$) with large amount of coarse particles (68% of total volume concentration). Heavy pollution (type 4) is characterized by heavy aerosols ($\tau_{500} > 1$) and a large volume of fine particles (70%). The heavy pollution could be explained by a mixture of particle types such as very small carbonaceous and sulfate particles.

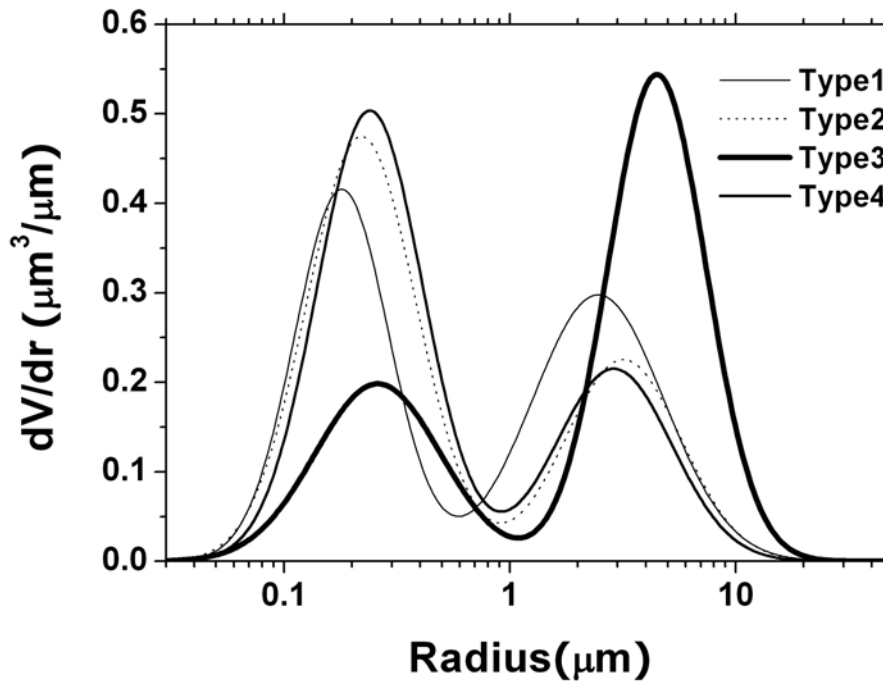


Figure 5.9. Aerosol size distributions used in this study

The LUT construction was based on the above 4 aerosol models with 9 solar zenith angles ($0^\circ \sim 80^\circ$, $\Delta = 10^\circ$), 17 view zenith angles ($0^\circ \sim 80^\circ$, $\Delta = 5^\circ$), 18 relative sun/satellite azimuth angles ($0^\circ \sim 170^\circ$, $\Delta = 10^\circ$), 8 RH values (RH = 0%, 50%, 70%, 80%, 90%, 95%, 98%, and 99%). The SBDART code used the aerosol properties associated with a given model, plus the combinations of values for the 4 parameters listed above (amounting to 264,384 combinations for 3 bands (470, 550, 660 nm)), to compute the hypothetical AOT. Figure 5.10 represents one of the LUTs from the SBDART results.

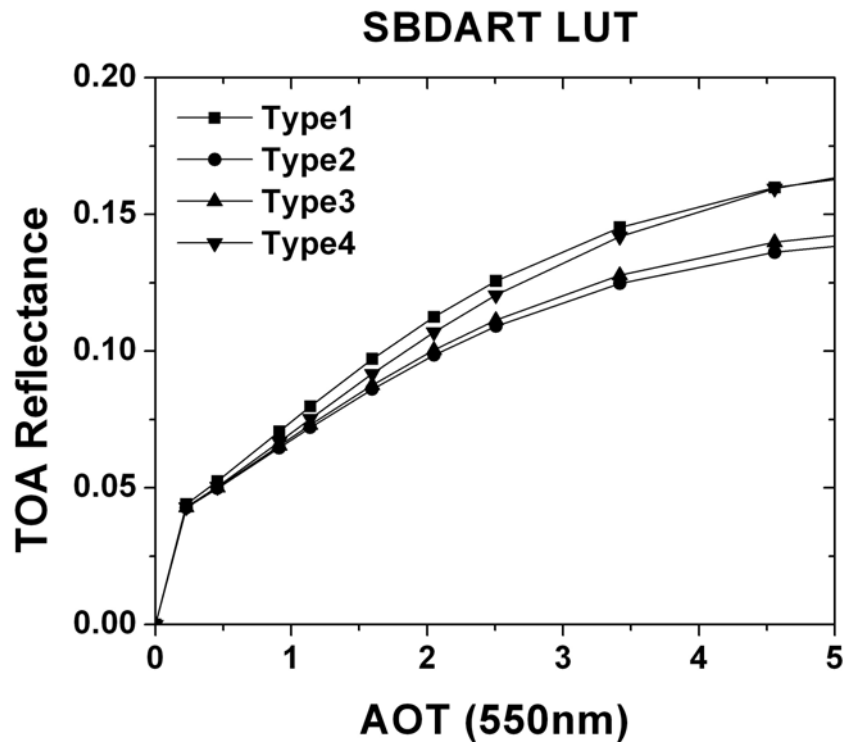


Figure 5.10. The SBDART calculations were performed with solar zenith = 30° , satellite zenith angle = 10° , azimuth angle = 150°

5.4. *Aerosol retrieval*

The satellite measured aerosol reflectances decomposed from TOA reflectances, surface reflectances and Rayleigh path radiance can be fitted to the LUT to derive the AOT from the images. The first step in this retrieval starts from deriving aerosol reflectances from images. The second step is to derive modeled aerosol reflectances from LUT, and the last step is to compare the image and modeled aerosol reflectances and to find the appropriate aerosol model and AOT for each pixel.

5.4.1. Deriving image aerosol reflectances

Before deriving aerosol reflectances from images, the LUTs with a specific RH should be read. The hourly RH values were acquired from the Hong Kong Observatory station at Tsim Sha Tsui. They were sorted out and co-matched with the MODIS overpass time (within ± 30 minutes) and the nearest RH values in the LUT were read. The second step is the interpolation of the LUT geometry to the measured (satellite) geometry. The bilinear interpolation method was adopted for interpolating between two nearest data in LUTs at a given geometry. These two steps can reduce the number of LUT values being read in the computer memory. In the third step, image aerosol reflectances are determined based on the Equation 5.13:

$$\rho_{TOA} = \rho_{Aer} + \rho_{Ray} + \frac{\Gamma_{Tot}(\theta_0) \cdot \Gamma_{Tot}(\theta_s) \cdot \rho_{Surf}}{1 - \rho_{Surf} \cdot r_{Hem}} \quad \text{Eq 5.13.}$$

where θ_0 is the solar zenith angle, θ_s is the satellite zenith angle, ρ_{Aer} is the aerosol reflectance, ρ_{Ray} is the Rayleigh reflectance, $\Gamma_{Tot}(\theta_0)$ is the transmittance along the path from the sun to ground, $\Gamma_{Tot}(\theta_s)$ is the transmittance along the path from the sensor to ground, ρ_{Surf} is the surface reflectance, and r_{Hem} is the hemispheric reflectance.

The Rayleigh transmittances were calculated with Equations 5.6 and 5.7, and aerosol transmittances were computed using the same equations by replacing the Rayleigh optical thickness with hypothetical aerosol AOT at 550nm. The total transmittances are the products of aerosol and Rayleigh transmittances. The Rayleigh reflectances were calculated with Equation 5.10. The surface reflectances were determined using the MRT technique and the TOA reflectances are the MODIS at-sensor reflectance. Then the hemispheric reflectance with both Rayleigh and aerosol contribution was determined from Equation 5.14. Finally, the aerosol reflectances from the image were obtained.

$$r_{Hem} = 0.33185 \cdot (\tau_{Ray} + \tau_{AOT_hypothetical}) - 0.19653 \cdot (\tau_{Ray} + \tau_{AOT_hypothetical})^2 + 0.08935 \cdot (\tau_{Ray} + \tau_{AOT_hypothetical})^3 - 0.01674 \cdot (\tau_{Ray} + \tau_{AOT_hypothetical})^4 \quad \text{Eq 5.14.}$$

where r_{Hem} is the hemispheric reflectance, τ_{Ray} is Rayleigh optical thickness, $\tau_{AOT_hypothetical}$ is hypothetical aerosol optical thickness at 550nm.

5.4.2. Deriving modeled aerosol reflectances

The original LUT contained the AOT values and TOA reflectances at different geometries and relative humidities, while LUTs of aerosol reflectances as a function of AOT values at different geometries and relative humidities were also created by simply:

$$\rho_{Aer} = \rho_{TOA} - \rho_{TOA_when_AOT=0} \quad \text{Eq 5.15.}$$

where ρ_{Aer} is aerosol reflectance, ρ_{TOA} is TOA reflectance, $\rho_{TOA_when_AOT=0}$ is the TOA reflectance when AOT = 0, it is Rayleigh reflectance.

Therefore, both image and modeled aerosol reflectances with specific relative humidity and geometry were obtained for each pixel.

5.4.3. Deriving AOT

Finally, the satellite observed aerosol reflectances ($\rho_{\lambda_j}^a$) were compared to the modeled aerosol reflectances ($\rho_{\lambda_j}^m$) for each geometrically corrected LUT. For these comparisons, an optimal spectral shape-fitting technique was executed to select the aerosol model with the smallest systematic errors (Kaufman and Tanré, 1998; Costa et al., 1999; Torricella et al., 1999; Lee et al., 2007) (Equation 5.16).

$$x^2 = \frac{1}{n} \sum_{i=1}^n \left(\frac{\rho_{\lambda_j}^m - \rho_{\lambda_j}^a}{\rho_{\lambda_j}^m} \right)^2 \quad \text{Eq 5.16.}$$

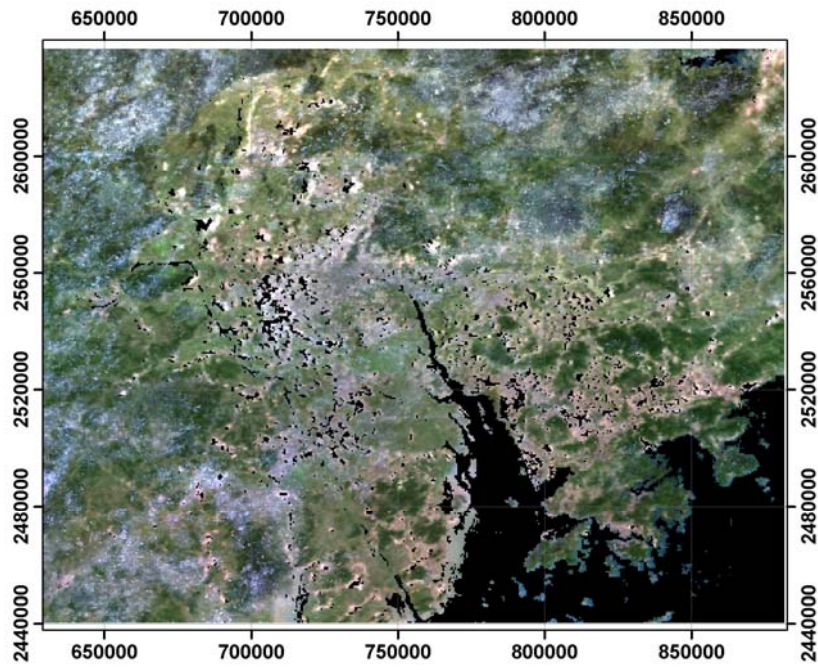
The error term of x^2 is described as the residual of the measured aerosol reflectances $\rho_{\lambda_j}^m$ from MODIS and modeled aerosol reflectances $\rho_{\lambda_j}^a$ from aerosol models in three different wavelengths (eg. 470nm, 550nm, 660nm). The minimum residual of x^2 is selected from the four aerosol types for each pixel. After locating the appropriate aerosol model, the AOT values at 470nm, 550nm, 660nm were derived for each pixel.

CHAPTER 6.

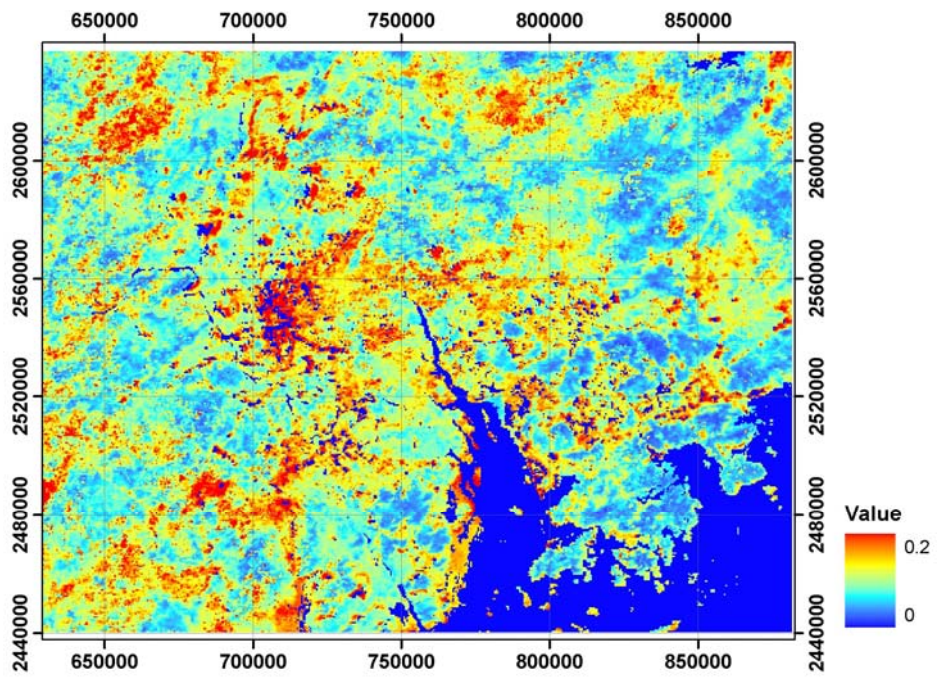
RESULTS

6.1. *Validation of surface reflectance images (MRT vs MOD09)*

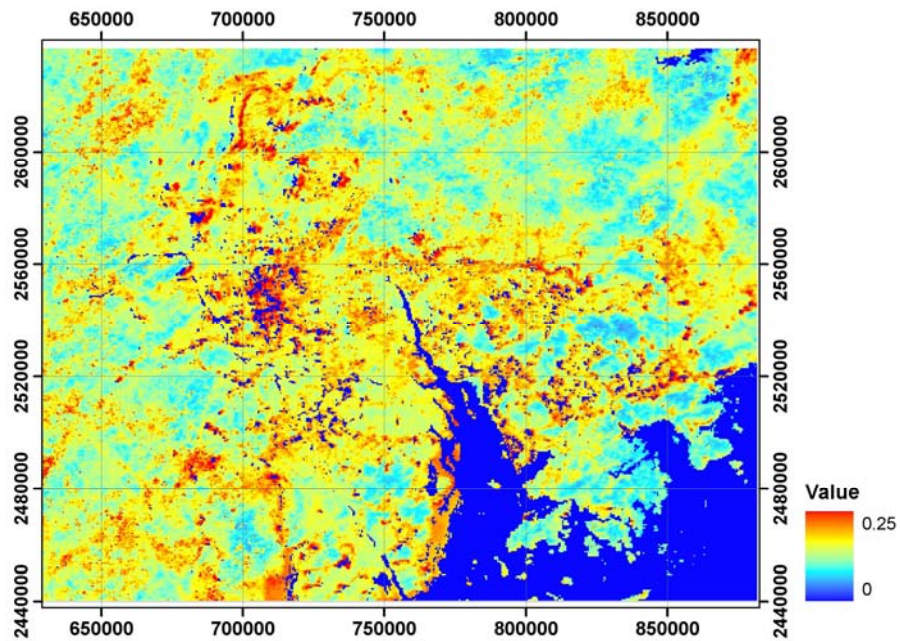
The minimum reflectance images at 500m resolution were validated by comparison with the MOD09 images which were resampled from 1km to 500m resolution. Figure 6.1 shows the example of MOD09 surface reflectance images in the autumn season. The comparison between the seasonally averaged MOD09 images and MRT images is shown in Figures 5.5 and 6.1. The MRT images of the two longer wavelengths, 550 and 660nm are similar to the MOD09 images (Figure 5.5c and 6.1c; 5.5d and 6.1d), but the 470nm image is not (Figure 5.5b and 6.1b). The differences in surface reflectances (y-intercepts of the slopes) were less than or equal to 0.01 for the 550 and 660nm wavelengths (Figure 6.2 b, c, e, f, h, i) while the differences are greater for the shorter 470nm wavelength (~0.02 - 0.03) (Figure 6.2 a, d, g). The MAD errors listed in Table 6.1 show the largest errors for shorter wavelengths (eg. 470nm, 550nm, 660nm) in three seasons are ca. 0.0249, 0.0109, 0.0120 respectively, whereas RMS errors have larger error values: 0.0260, 0.0152, 0.0146 respectively. This gives a potential AOT error of 0.2 - 0.3 due to error in surface reflectance for the 470nm wavelength, if absolute accuracy of the MOD09 images is assumed. However such accuracy cannot be assumed due to the errors of atmospheric correction in the MOD09 products (Vermote and El Saleous, 2006). Thus we estimate the uncertainty of our AOT values induced by the MRT surface reflectances to be in the range of 0 to 0.3, and to be greater and more significant in the shorter wavelength (470 nm) but minimal at longer wavelengths (550, 660 nm). Generally, stronger correlations between the MRT images and MOD09 were observed in the autumn and winter seasons ($r^2 > 0.87$), while moderate correlations were noted in the spring season ($r^2 > 0.76$) (Figure 6.2). Due to the cloud covers being always present in summer, less than fifteen clear sky images could be acquired.



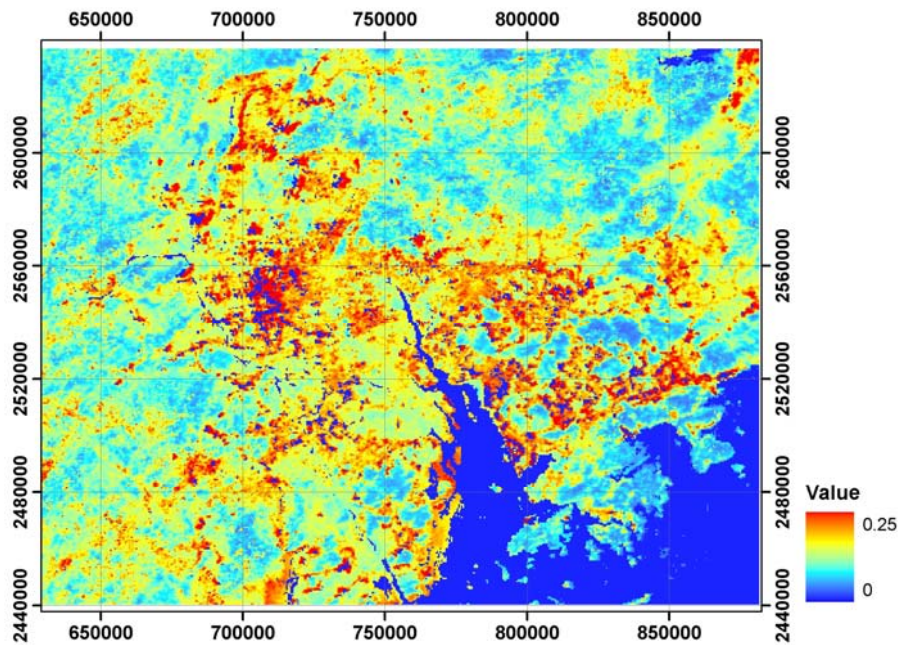
a.



b.

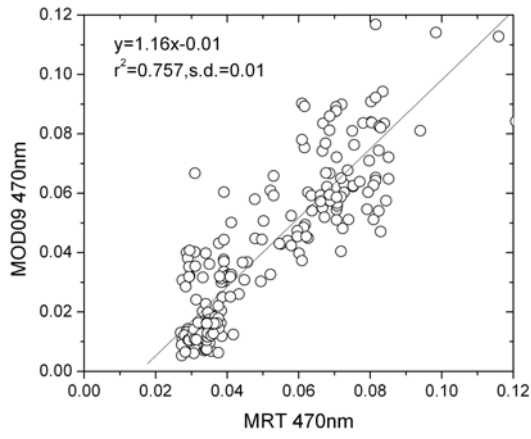


c.

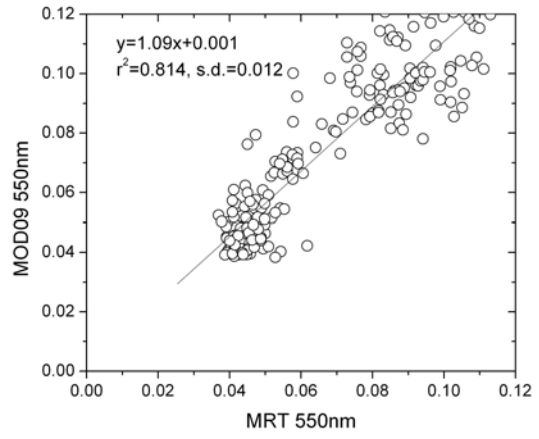


d.

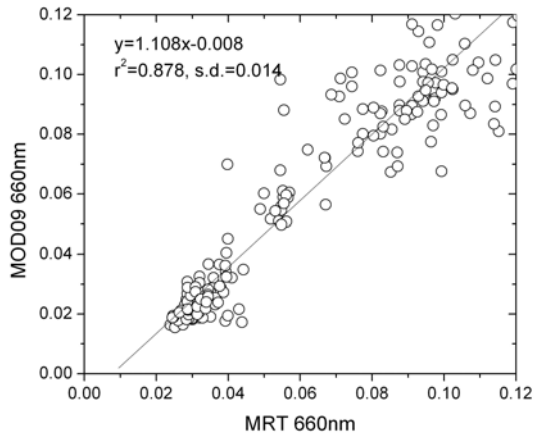
Figure 6.1. Surface reflectance images in the autumn (in UTM grid coordinate system); a. RGB composite of MOD09, b. MOD09 at 470nm, c. MOD09 at 550nm, d. MOD09 at 660nm



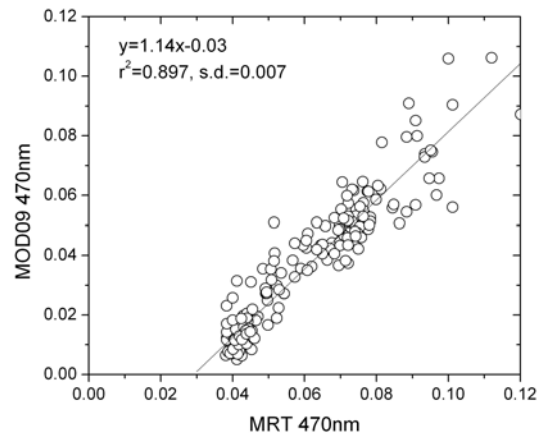
a.



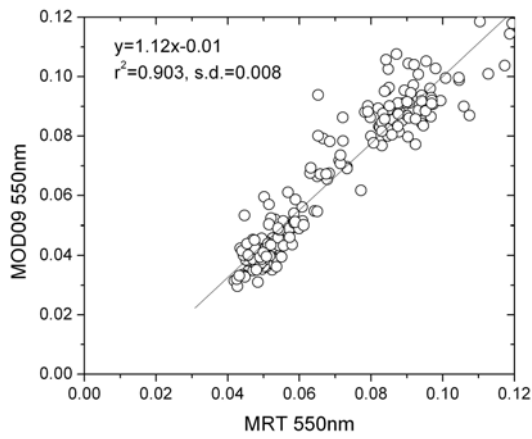
b.



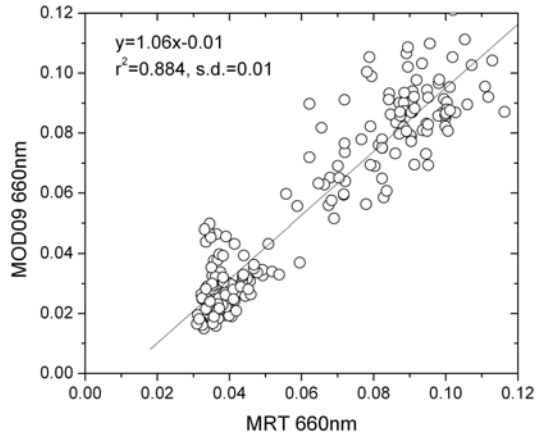
c.



d.



e.



f.

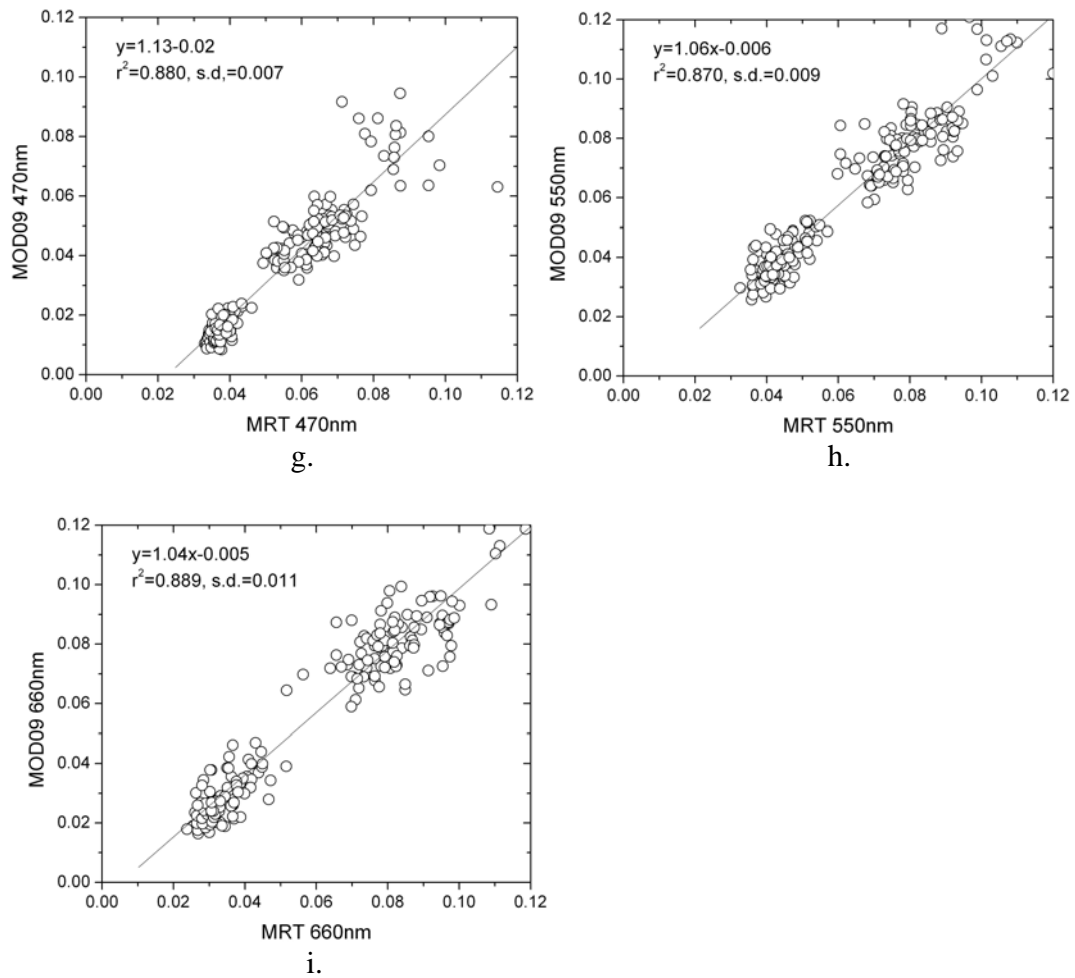


Figure 6.2. Scatter plots between surface reflectances derived from MRT and from MOD09 products: a. at 470nm in spring, b. at 550nm in spring, c. at 660nm in spring, d. at 470nm in autumn, e. at 550nm in autumn, f. at 660nm in autumn, g. at 470nm in winter, h. at 550nm in winter, i. at 660nm in winter

	Winter			Autumn			Spring		
	470nm	550nm	660nm	470nm	550nm	660nm	470nm	550nm	660nm
Root-Mean-Square (RMS) error	0.0202	0.0097	0.0114	0.0260	0.0097	0.0140	0.0170	0.0152	0.0146
Mean Absolute Difference (MAD)	0.0191	0.0070	0.0083	0.0249	0.0080	0.0120	0.0150	0.0109	0.0106

Table 6.1. Statistical comparison between the surface reflectances of MRT and MOD09

6.2. Validation of surface reflectance images (MRT vs MSR field measurements)

Fifty-one ground-based reflectance measurements using Cropscan MSR-16R multispectral radiometer were taken on four winter dates: Oct 21 2006, Oct 29 2006, Nov 05 2006 and Dec 29 2006. It is assumed that vegetation does not change much in terms of reflectance in winter time, thus ground measurements taken by Cropscan multispectral radiometer were used to validate the results from the winter MRT image (Figure 6.3 and 6.4).



Figure 6.3. Field measurements of surface reflectances over dense vegetation

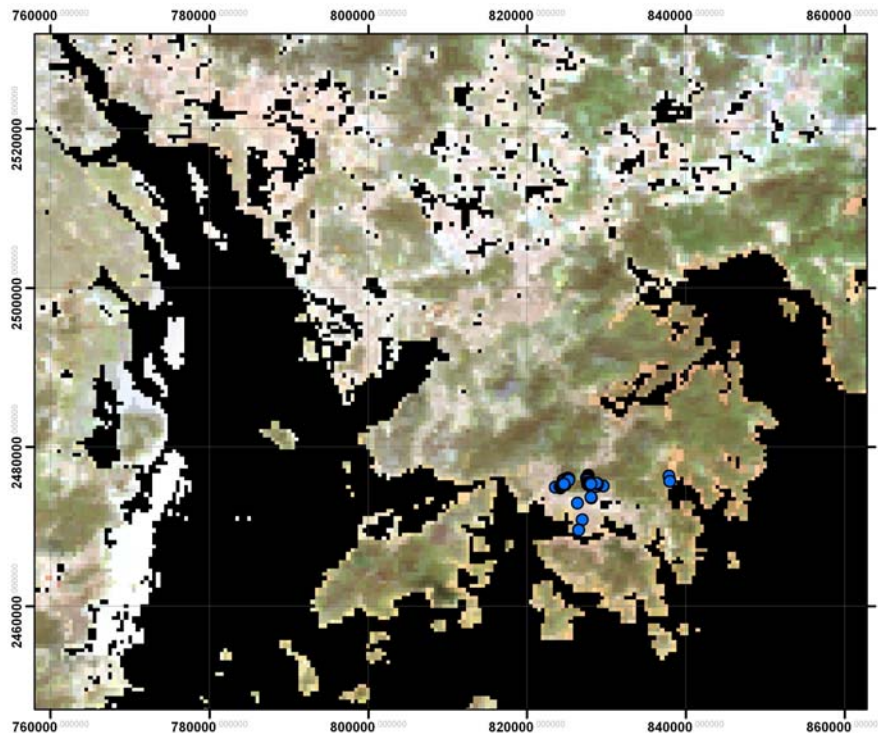


Figure 6.4. Locations of field measurements overlaid with the winter MRT image (blue spots)

Table 6.2 lists all the fifty-one field measurements and surface reflectances observed from winter MRT image. It was found that the general differences between minimum reflectances and ground reflectances were between 0.01 - 0.03. The Mean Absolute Difference (MAD) values are 0.03 (470nm), 0.02 (550nm) and 0.02 (660nm), respectively. Since ground-based measurements were only taken from vegetated areas, there were no validation points on bright and dark urban surfaces. But the consistency of the findings both confirm the magnitude of error previously observed i.e. 0 - 0.03. Thus the AOT has an uncertainty of between 0 and 0.3, and this is greater and more significant in the shorter wavelength (470 nm) but minimal at longer wavelengths (550, 660 nm).

Point ID	Date	Time	Surface characteristics	Latitude	Longitude	MRT-470nm	MSR-485nm	MRT-555nm	MSR-550nm	MRT-660nm	MSR-660nm
1	10/21/2006	13:21:12	Dense forest	20.989	11.989	0.059	0.018	0.073	0.048	0.065	0.028
2	10/21/2006	13:27:54	Dense forest	20.988	11.505	0.046	0.019	0.058	0.052	0.042	0.030
3	10/21/2006	14:52:24	Dense forest	21.158	11.588	0.043	0.016	0.053	0.041	0.037	0.025
4	10/21/2006	14:58:05	Dense forest	21.197	11.533	0.042	0.022	0.052	0.056	0.035	0.034
5	10/21/2006	15:14:38	Dense forest	21.201	11.524	0.042	0.021	0.052	0.066	0.035	0.033
6	10/21/2006	15:20:54	Dense forest	21.205	11.522	0.042	0.011	0.052	0.028	0.035	0.015
7	10/21/2006	15:25:02	Dense forest	20.989	11.989	0.059	0.014	0.073	0.041	0.065	0.021
8	10/29/2006	11:18:44	Dense forest	20.214	11.109	0.078	0.020	0.095	0.057	0.101	0.032
9	10/29/2006	11:43:00	Shrubland	20.256	11.071	0.077	0.063	0.095	0.135	0.100	0.072
10	10/29/2006	13:36:16	Dense forest	19.886	10.075	0.073	0.020	0.087	0.125	0.091	0.089
11	10/29/2006	14:44:53	Dense forest	18.738	10.397	0.074	0.021	0.088	0.057	0.092	0.027
12	10/29/2006	15:43:17	Dense forest	18.051	10.147	0.066	0.019	0.078	0.061	0.077	0.038
13	10/29/2006	15:59:13	Dense forest	18.041	10.136	0.064	0.017	0.077	0.048	0.075	0.019
14	11/5/2006	11:42:18	Dense forest	21.136	09.225	0.047	0.014	0.059	0.042	0.045	0.019
15	11/5/2006	11:57:54	Dense forest	21.282	09.095	0.046	0.012	0.058	0.034	0.045	0.015
16	11/5/2006	12:06:16	Shrubland	21.391	09.077	0.046	0.064	0.057	0.156	0.045	0.144
17	11/5/2006	12:14:17	Dense forest	21.476	09.086	0.045	0.011	0.056	0.042	0.045	0.034
18	11/5/2006	12:20:03	Dense forest	21.496	09.193	0.044	0.017	0.056	0.045	0.044	0.050
19	11/5/2006	12:26:43	Dense forest	21.512	09.194	0.044	0.008	0.056	0.017	0.044	0.010
20	11/5/2006	12:40:39	Shrubland	21.527	09.363	0.044	0.027	0.056	0.081	0.043	0.083
21	11/5/2006	12:47:35	Dense forest	21.532	09.334	0.044	0.015	0.055	0.036	0.042	0.029
22	11/5/2006	12:53:01	Shrubby grassland	21.590	09.417	0.044	0.129	0.056	0.283	0.042	0.320
23	11/5/2006	13:00:32	Dense forest	21.559	09.481	0.044	0.016	0.056	0.054	0.042	0.023
24	11/5/2006	14:12:43	Shrubland	21.468	09.496	0.053	0.033	0.066	0.068	0.058	0.055
25	11/5/2006	14:28:34	Dense forest	20.935	08.865	0.061	0.020	0.073	0.051	0.069	0.037
26	11/5/2006	14:33:01	Dense forest	20.982	08.484	0.053	0.014	0.065	0.037	0.056	0.020
27	11/5/2006	14:41:10	Dense forest	21.040	08.845	0.051	0.022	0.064	0.053	0.054	0.058
28	11/5/2006	14:46:13	Shrubland	21.050	08.859	0.051	0.034	0.063	0.080	0.052	0.053
29	11/5/2006	14:52:03	Shrubland	21.060	08.924	0.050	0.027	0.062	0.073	0.050	0.052
30	11/5/2006	14:58:28	Dense forest	21.055	08.955	0.049	0.022	0.061	0.063	0.049	0.033
31	11/5/2006	15:03:42	Dense forest	21.111	08.964	0.049	0.015	0.061	0.055	0.049	0.034
32	11/5/2006	15:08:51	Dense forest	21.118	08.998	0.048	0.026	0.060	0.073	0.047	0.056
33	11/5/2006	15:13:42	Dense forest	21.134	09.039	0.047	0.018	0.059	0.058	0.045	0.021
34	11/5/2006	15:16:08	Dense forest	21.182	09.077	0.048	0.010	0.056	0.034	0.046	0.019

35	11/5/2006	15:17:47	Dense forest	22- 21.202	114- 09.123	0.045	0.022	0.053	0.045	0.040	0.041
36	12/29/2006	12:14:31	Dense forest	22- 21.742	114- 10.905	0.043	0.014	0.051	0.046	0.038	0.023
37	12/29/2006	12:24:27	Dense forest	22- 21.703	114- 10.902	0.043	0.015	0.051	0.038	0.037	0.051
38	12/29/2006	12:32:24	Shrubland	22- 21.643	114- 10.898	0.059	0.029	0.066	0.064	0.049	0.049
39	12/29/2006	12:45:05	Dense forest	22- 21.579	114- 10.862	0.044	0.023	0.053	0.059	0.039	0.042
40	12/29/2006	12:49:52	Dense forest	22- 21.575	114- 16.846	0.043	0.014	0.051	0.042	0.038	0.023
41	12/29/2006	12:55:56	Shrubland	22- 21.576	114- 10.822	0.045	0.031	0.054	0.076	0.040	0.051
42	12/29/2006	13:00:07	Shrubland	22- 21.559	114- 10.817	0.044	0.031	0.054	0.069	0.039	0.060
43	12/29/2006	13:08:22	Shrubland	22- 21.554	114- 10.794	0.043	0.058	0.052	0.157	0.037	0.142
44	12/29/2006	13:33:00	Dense forest	22- 21.547	114- 10.782	0.042	0.020	0.052	0.050	0.037	0.039
45	12/29/2006	13:49:15	Dense forest	22- 21.438	114- 10.807	0.060	0.016	0.065	0.065	0.050	0.056
46	12/29/2006	13:57:29	Dense forest	22- 21.278	114- 10.842	0.042	0.024	0.053	0.078	0.038	0.048
47	12/29/2006	14:12:24	Shrubby grassland	22- 21.221	114- 16.883	0.042	0.102	0.053	0.227	0.038	0.163
48	12/29/2006	14:16:02	Dense forest	22- 21.182	114- 10.878	0.042	0.022	0.053	0.048	0.038	0.036
49	12/29/2006	14:20:50	Dense forest	22- 21.131	114- 10.887	0.042	0.011	0.053	0.040	0.038	0.029
50	12/29/2006	14:38:38	Shrubland	22- 21.086	114- 10.948	0.042	0.055	0.052	0.091	0.037	0.079
51	12/29/2006	14:44:43	Dense forest	22- 21.123	114- 10.983	0.042	0.022	0.052	0.053	0.037	0.040

Table 6.2. Surface reflectances from MRT images and multispectral radiometer field measurements

6.3. Validation of cloud masking with Hong Kong Observatory data

Equation 5.12 was adopted for cloud masking based on a trial-and-error approach. Validation using Hong Kong Observatory cloud cover data is illustrated in this section. The celestial dome in Hong Kong Observatory measures the oktas of cloudiness with a range of 0 (no obscuration) to 8 (full obscuration). The confusion matrix of cloud masking (Table 6.3) shows 78.13% accuracy (type 7 & type 8). The error of commission is 3.91% (type 0 & type 1). The accuracy of cloud removal suggested in this study is comparable to the accuracy stated in the MODIS operational algorithm (ca. 82%). In addition, the confusion matrix also shows that 43.48% (type 2 to type 8) of the image data still contains small and thin cirrus clouds without masking, the small clouds are

difficult to detect except using very high resolution thermal image, more analysis and tests will be considered in future work.

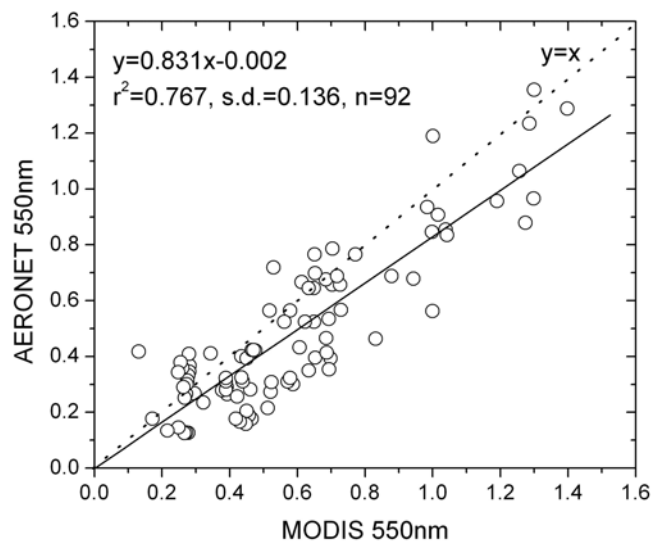
With cloud masking on MODIS images			Without cloud masking on MODIS images		
	Number of days	Percentage		Number of days	Percentage
Type 0	2	0.78	Type 0	29	31.52
Type 1	9	3.13	Type 1	22	23.91
Type 2	6	2.34	Type 2	5	5.43
Type 3	9	3.13	Type 3	4	4.35
Type 4	4	1.56	Type 4	3	3.26
Type 5	17	6.25	Type 5	6	6.52
Type 6	13	4.69	Type 6	6	6.52
Type 7	177	64.84	Type 7	16	17.39
Type 8	36	13.28	Type 8	0	0.00
Sum of Type7 and 8		78.13	Sum of Type 1 and 2		55.43

Table 6.3. Confusion matrix of cloud masking

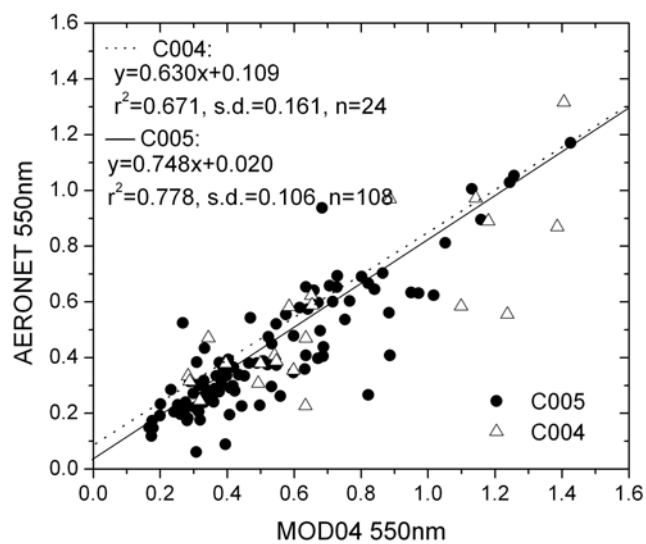
6.4. Validation of image derived AOT (500m) with AERONET measurements

The MODIS 500m retrieved AOT was validated using AERONET measurements for 2007 (Figure 6.5a) and good agreement is shown between our methodology and the AERONET, with a correlation coefficient $r^2 = 0.767$. For further comparison, the MOD04 collection 4 and 5 AOT data at 10km resolution were also compared with AERONET (Figure 6.5b). The correlation coefficients of $r^2 = 0.778$ and $r^2 = 0.671$ were observed from collection 5 and collection 4 respectively. The correlation coefficient of our methodology is similar to the values of collection 5, but it has a smaller magnitude of overestimation of AOT (~ -0.002) than that of collection 4 and 5. The MAD error computed for MODIS 500m image and AERONET data is 0.142, and that for MODIS collection 5 is 0.129. The RMS error and bias error estimated from MODIS 500 AOT are similar to those for collection 5: the bias values are 0.11 for both MODIS 500m and collection 5. The RMS errors of collection 5 and MODIS 500m are 0.167, 0.176

respectively (Table 6.4). However, more importantly, our MRT methodology does not only retrieve AOT images at a much higher spatial resolution, but it can also retrieve AOT over bright urban surfaces as well as dark rural vegetated areas. Both of these improvements are significant for a topographically complex area with heterogeneous land cover like Hong Kong.



a.



b.

Figure 6.5. Scatter plots, a. between MODIS 500m AOT and AERONET measurements; b. between MOD04 collection 4, 5 AOT and AERONET measurements

	Correlation (r^2)	Bias estimator ($E(S^2)$)	Root-Mean- Square Error (RMS)	Mean Absolute Difference (MAD)	Number of samples (n)
MODIS Collection 4	0.671	0.032	0.249	0.174	24 (on year 2007)
MODIS Collection 5	0.778	0.011	0.167	0.129	108 (on year 2007)
MODIS 500m (validated with AERONET)	0.767	0.011	0.176	0.142	92 (on year 2007)
MODIS 500m (validated with MicrotopsII)	0.760	0.011	0.182	0.150	14 (on year 2007)

Table 6.4. Statistical comparison between the performances of collection 4 and collection 5, MODIS 500m AOT with AERONET and MicrotopsII data

Given that aerosol models play an important role in aerosol estimation, the minimum residual of x^2 is selected from the four aerosol types for each pixel (Equation 5.16). Thus the most appropriate aerosol type is assigned to the pixel with the minimum error and the AOT is derived from the appropriate aerosol type. Figure 6.6 shows the histogram of aerosol types derived from MODIS 500m algorithm over year 2007. The AOT for all ninety-two data was extracted in terms of aerosol types over the region surrounding the AERONET station. The results show that there are 18 days for type 1 (mixed urban aerosol), 60 days for type 2 (polluted urban aerosol), 10 days for type 3 (dust) and 4 days for type 4 (heavy urban pollution). Thus aerosol type 2 is mostly used ($\sim 65\%$) and aerosol type 4 is least used ($\sim 4\%$) during the MODIS aerosol retrieval. Since the MODIS overpass time is in the mid-morning (10:30 a.m.) following peak traffic density, the frequency of type 4 (heavy urban pollution) is certainly smaller compared with type 2

(polluted urban aerosol). Type 1 and type 3 account for 20% and 11% of occurrence respectively for the MODIS overpass time over the AERONET station. As mentioned in Section 5.3.1, the dust aerosol model is not often applicable in Hong Kong which is far from the source area and the mixed urban aerosol type is the second highly used model because the AERONET station is near the coast.

It should be noted that the occurrences of different aerosol types during aerosol retrieval is different from those during the clustering classification (Section 5.3.1). This is because the MODIS aerosol retrieval is only taken with images of overpass time of 10:30 a.m. where the clustering classification made use of all the data from AERONET which operates from 8 a.m. to 6 p.m. daily. However, the results show that type 1 (mixed urban aerosol) and type 2 (polluted urban aerosol) are the dominant aerosol types during both the clustering and the retrieval.

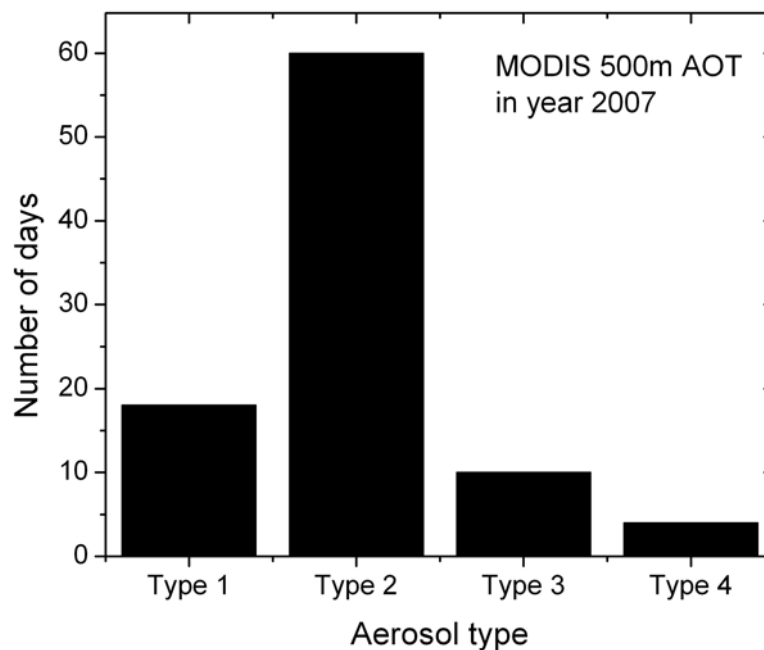


Figure 6.6 Histogram of occurrences for different aerosol types derived from the MODIS 500m algorithm

6.5. Validation of image derived AOT (500m) with MicrotopsII measurements

The mobile MicrotopsII sunphotometer provides an alternative to AERONET for measuring “in-situ” aerosols. The portability of this instrument allows us to measure the AOT in different locations and over different landcover types (eg. urban, rural and water). It measures the AOT at wavelengths of 440nm, 550nm, 675nm, 870nm and 936nm. Since there is no wavelength at 550nm, the Angstrom exponent (Equation 6.1) can be calculated based on 440nm and 675nm wavelengths.

$$\alpha = -\frac{\ln\left(\frac{\tau_{\lambda_1}}{\tau_{\lambda_2}}\right)}{\ln\left(\frac{\lambda_1}{\lambda_2}\right)} \quad \text{Eq 6.1.}$$

where Angstrom exponent is α , τ_{λ_1} is AOT at wavelength 1, λ_1 is wavelength 1. τ_{λ_2} is AOT at wavelength 2, λ_2 is wavelength 2.

A total of 172 measurements were taken on Nov 11 2007, Nov 28 2007, Dec 14 2007 from 9:00 a.m. to 12:00 p.m.. Each measurement was taken at intervals of 10 minutes. Only the measurements with times close to the MODIS overpass time (± 60 minutes) were used, and they were averaged. This gives 14 temporally matched measurements at 14 different sites, the locations of which are displayed in Figure 6.7. Four measurements were taken on the bright urban surfaces, two on urban grass and the others are in rural sites. Table 6.5 shows the 14 measurements and Table 6.6 shows the meteorological conditions on those dates. The wind speeds were moderate ($3 - 4.5\text{ms}^{-2}$) and no precipitation was recorded on those three dates. Very little cloud cover recorded on Nov 28 2007 while 4/8 and 5/8 of sky were covered by cloud on Nov 11 2007 and Dec 14 2007. This can also be seen in Figure 6.8 where the missing areas are cloud covered.

A good agreement is shown between AOT from MicrotopsII measurements and AOT derived from MODIS 500 images, with a correlation coefficient $r^2 = 0.760$ (Figure 6.9).

The MODIS 500 AOT images have a larger magnitude of underestimation of AOT (y intercept = 0.132) compared with MicrotopsII measurement. The MAD error between MODIS 500m AOT and MicrotopsII is 0.150 whereas a smaller MAD error (0.142) was obtained for the comparison with AERONET. The RMS error with a value 0.182 was obtained from MicrotopsII whereas a smaller RMS error (0.176) was obtained for the comparison with AERONET. The same bias value (0.011) was estimated from both AERONET and MicrotopsII measurements (Table 6.4). The general MAD and RMS errors can be concluded to be within 0.150 and 0.182 of AOT values which is smaller than the estimated errors which may be derived from errors in surface reflectances (0 - 0.3). It is noted that all fourteen data were selected with the type 2 (polluted urban aerosol) aerosol model. The high correlation coefficients, small bias, small RMS error and small MAD error observed from both AERONET and MicrotopsII suggest the robustness of the methodology which can derive accurate AOT images for local and regional air pollution monitoring.

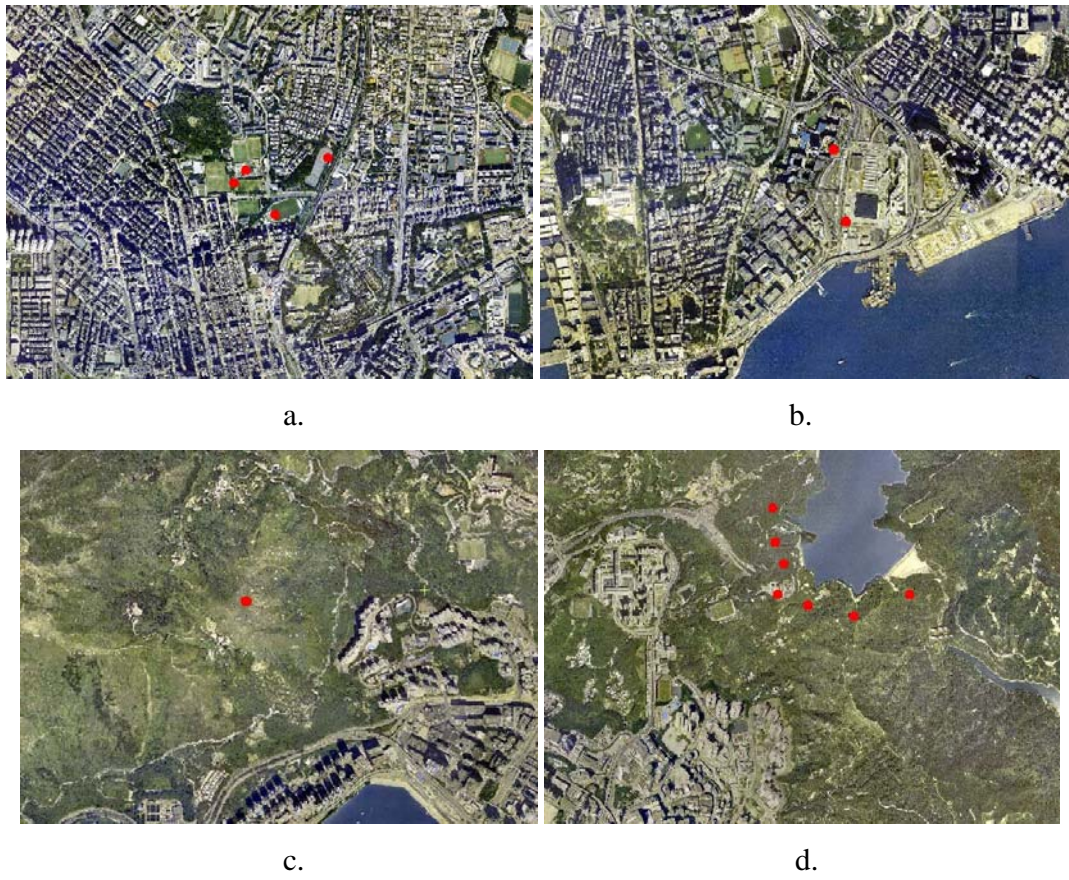
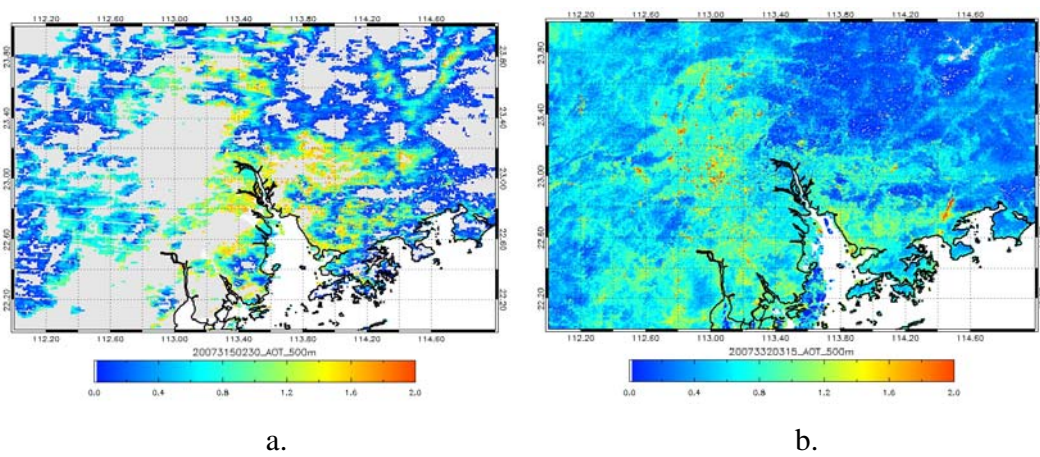
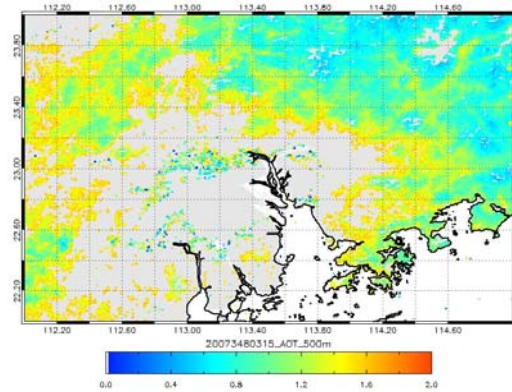


Figure 6.7. Locations of MSR field measurements, a. Mong Kok (urban area), b. Hung Hom (urban area), c. Tsuen Wan (rural area), d. Shing Mun (rural area)





c.

Figure 6.8. MODIS 500m AOT images on a. Nov 11 2007, b. Nov 28 2007, c. Dec 14 2007

ID	Date	Time	Latitude	Longitude	Surface characteristics	MODIS 500m AOT	MicrotopsII AOT
1	11/11/2007	10:30	22- 22.783	114- 05.917	rural	0.935	0.605
2	11/28/2007	10:30	22- 22.867	114- 08.600	rural	0.654	0.609
3	11/28/2007	10:30	22- 22.667	114- 08.767	rural	0.586	0.624
4	11/28/2007	10:30	22- 22.683	114- 08.550	rural	0.578	0.636
5	11/28/2007	10:30	22- 22.783	114- 08.617	rural	0.963	0.641
6	11/28/2007	10:30	22- 22.683	114- 08.933	rural	0.654	0.649
7	11/11/2007	11:15	22- 22.733	114- 08.650	rural	0.963	0.661
8	11/11/2007	11:15	22- 22.683	114- 08.550	rural	0.762	0.684
9	11/11/2007	11:15	22- 19.633	114- 10.233	urban grass	1.191	0.980
10	11/11/2007	11:15	22- 19.667	114- 10.267	urban grass	1.191	1.004
11	12/14/2007	11:15	22- 19.550	114- 10.350	urban	1.192	1.043
12	12/14/2007	11:15	22- 19.700	114- 10.500	urban	1.191	1.065
13	12/14/2007	11:15	22- 18.233	114- 10.833	urban	1.191	1.068
14	12/14/2007	11:15	22- 18.050	114- 10.867	urban	1.221	1.091

Table 6.5. AOT measurements from MicrotopsII on different dates

Station	Date	Time	Temperature (°C)	Wind speed (ms ⁻²)	Relative Humidity (%)	Precipitati on (mm)	Cloud cover (Okta 0-8)
HKO	11/11/2007	10:30	23	3	60	0	4
HKO	11/28/2007	10:30	15	4.5	27	0	1
HKO	12/14/2007	11:15	21	3.5	60	0	5

Table 6.6. Meteorological conditions on different dates

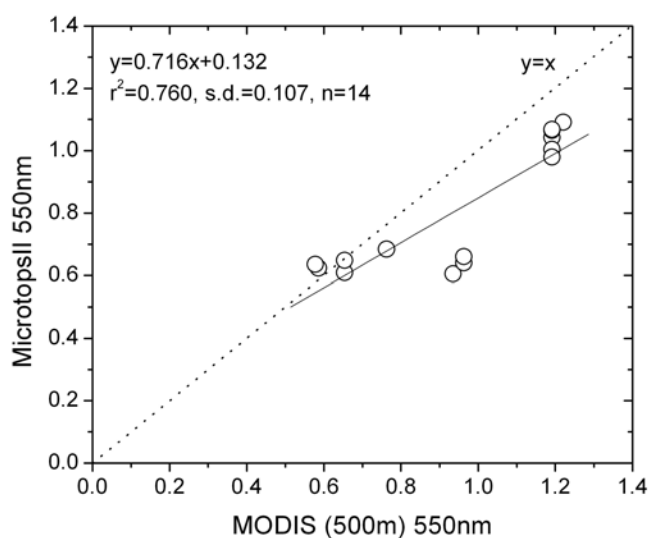


Figure 6.9. Scatter plot between MODIS 500m AOT and MicrotopsII measurements

6.6. Comparisons between AOT 500m image and AOT 10km image

The AOT distribution over Hong Kong and the PRD region on Oct 20 2007 retrieved using MODIS 500m data is shown in Figure 6.10. It is likely that fifteen pixels cover the entire Hong Kong territories with an AOT image at 10km resolution (Figure 6.10a) while there are many more using 500m resolution (Figure 6.10b). The spatial pattern of aerosols especially in Shenzhen (Chinese city near Hong Kong) is much more precisely defined using 500m AOT image compared with the 10km coarse pixels of MOD04. Figure 6.11 shows the AOT 500m images over Kowloon peninsula and part of Hong

Kong island overlaid with GIS road networks. The districts like Hung Hom, Sham Shui Po, Kowloon Bay and Ap Lei Chau observe high AOT values (~ 1.0) whereas the rural areas have relatively low AOT values (~ 0.3). Nichol et al. (2008) observed that PM10 data is not expected to show a high correlation with image-derived AOT data because of the non-selective scattering action of PM10 particles which are larger than the wavelengths used, while image-derived AOT data showed significant correlation with aerosol precursor gases (eg. the “urban continental” aerosol type is formed from unstable nitrate and sulphate compounds). Correlations (r^2) of 0.476, 0.16 and 0.096 for NO_2 , NO_x and SO_2 were obtained respectively. The image time at mid-morning (ca 10:30 a.m.) following peak traffic density may explain the substantial NO_2 levels came from traffic emission. Thus the higher resolution AOT image would be a good indicator for pinpointing the “black-spots” of traffic emission which will assist better urban design and traffic control.

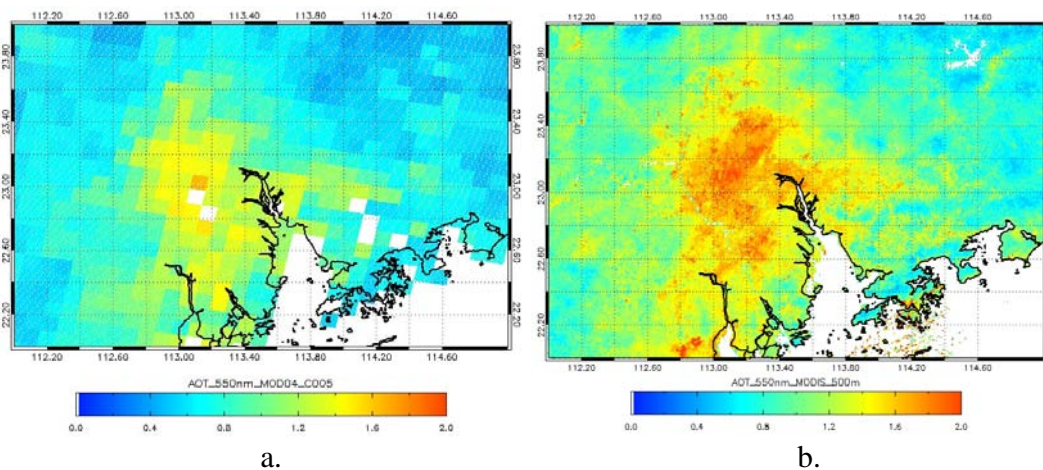


Figure 6.10. a. AOT at 550nm derived from MODIS MOD04 collection 5 algorithm, b. AOT at 550nm and 500m resolution derived from this study over Hong Kong and the Pearl River Delta region

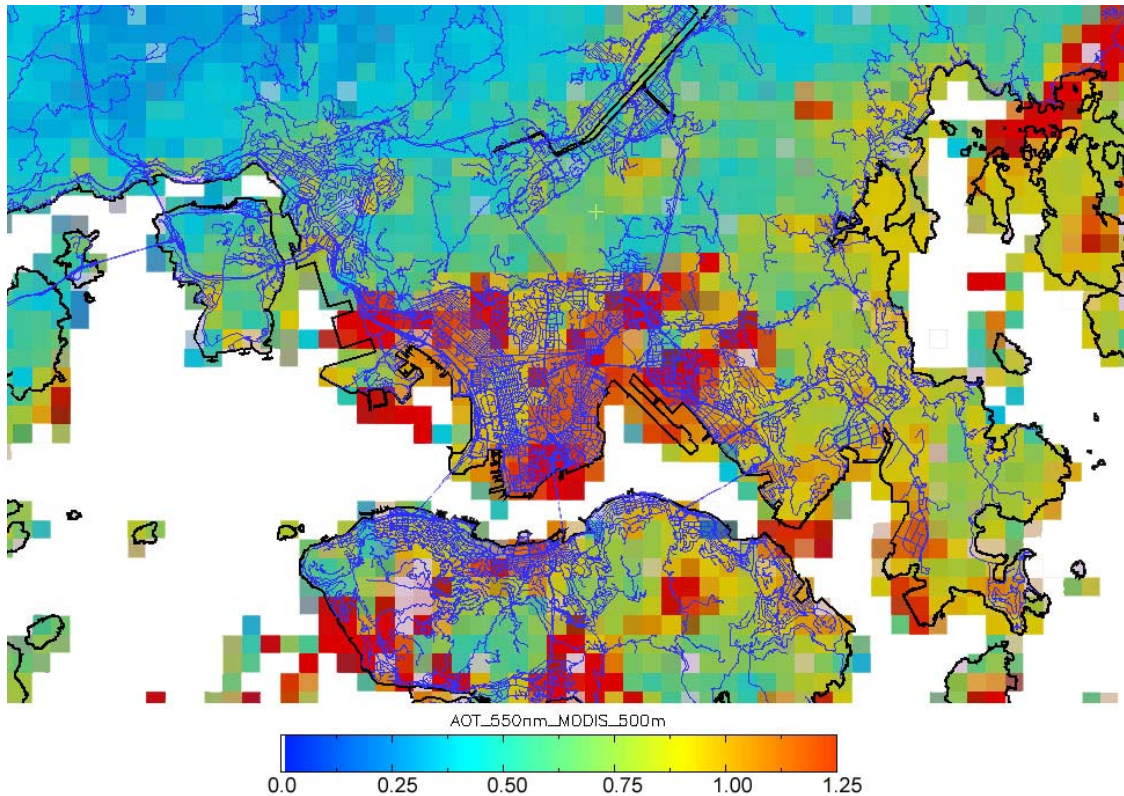


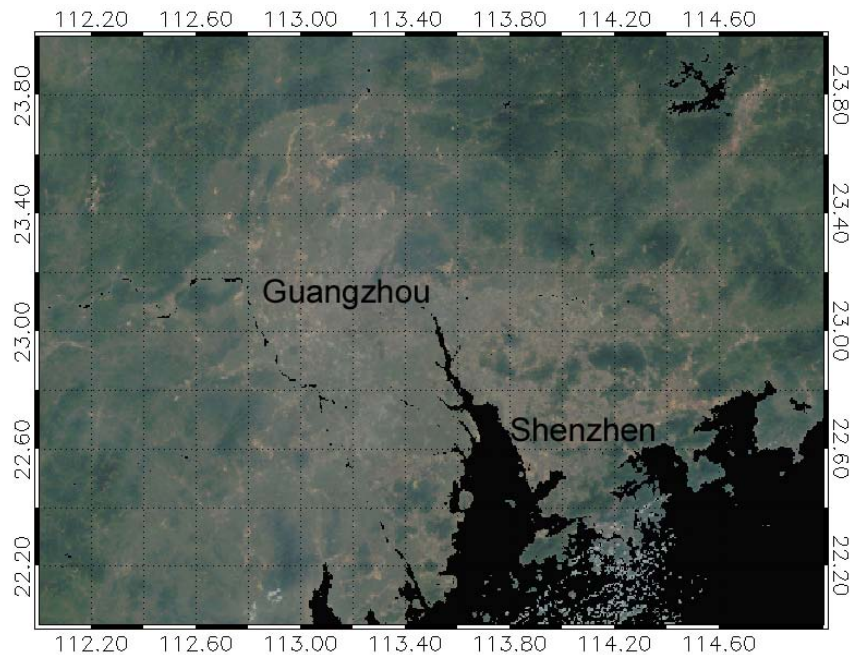
Figure 6.11. AOT at 550nm and 500m resolution derived from this study overlaid with GIS road data

6.7. Anthropogenic aerosol emission observed from AOT images

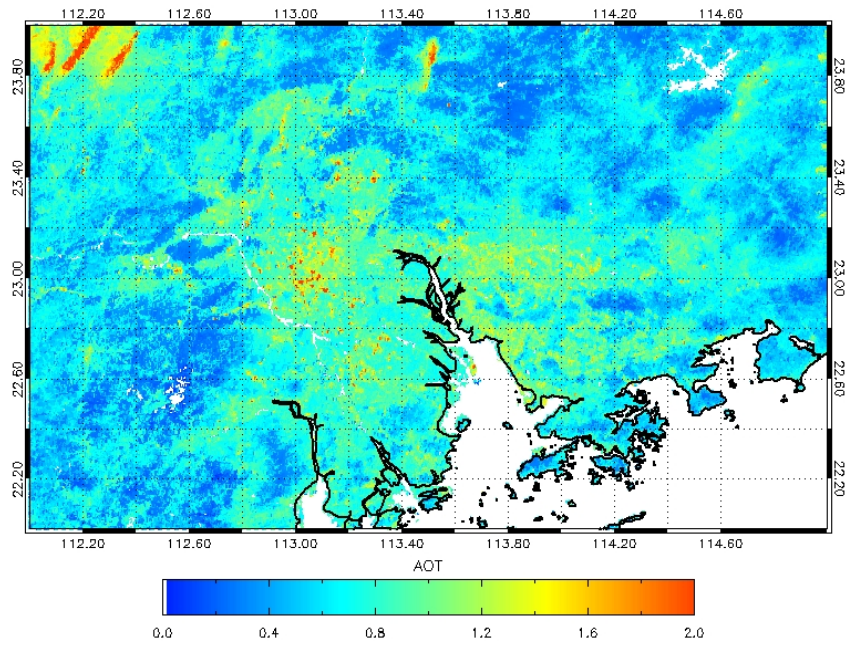
The AOT distribution over Hong Kong and the PRD region on Jan 28 2007 and Jan 30 2007 retrieved using MODIS 500m data are shown in Figure 6.12b, d. The general AOT of Jan 28 2007 is relatively low with a range of ~ 0.4 in rural areas to ~ 1.4 in urban areas. It is particularly notable that in industrialized areas of the PRD eg. Guangzhou city and Shunde district (Figure 6.12a), high AOT is observed, but in the other areas, low AOT values are observed due to strong wind speed ($\sim 4\text{ms}^{-2}$) (Figure 6.13a). However a rapid increase of AOT occurred two days later, Jan 30 2007. This extremely high AOT (~ 1.8) was observed over most industrialized areas in the PRD and it is shown as red colour in Figure 6.12c. There are many industries and power plants located there and due to the very low wind speeds ($\sim 1\text{ms}^{-1}$) on that day (Figure 6.13c), pollutants would be trapped in

the PRD region. The pollutants would be progressively accumulated as wind speeds decreased from 4ms^{-1} on Jan 28 2007 to 2ms^{-1} on Jan 29 2007 and 1ms^{-1} on Jan 30 2007.

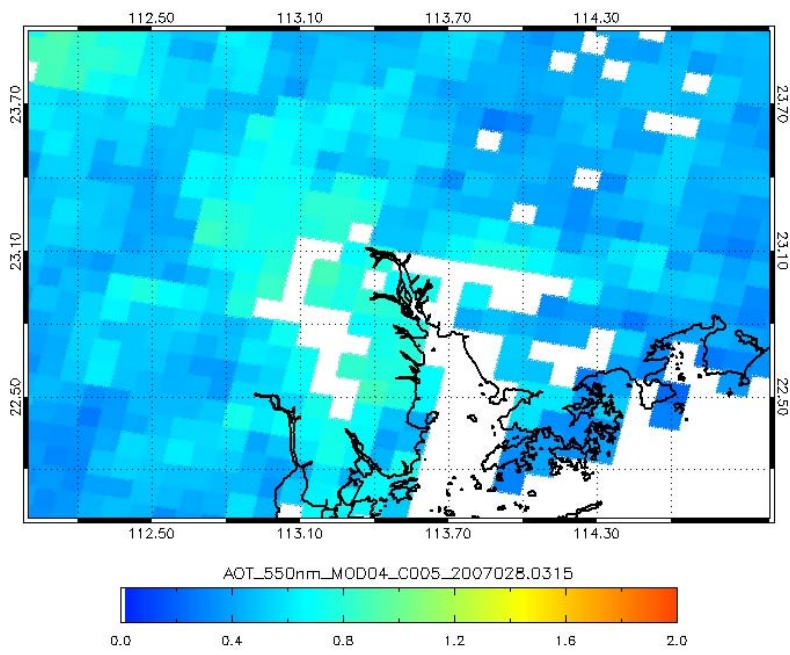
The northern part of Hong Kong especially near the Chinese city of Shenzhen commonly suffers from cross-boundary pollutants which are emitted from industries in the PRD region, and here AOT values of 1.0 are observed on Jan 30 2007. The MODIS collection 5 AOT image is visually and spatially inferior to its coarser (10km) resolution product (Figure 6.12c, e) and is ineffective for aerosol mapping in urban areas. The urban areas with heavy pollutants are masked out with no AOT data due to their high reflectance values not meeting the criteria in the operational algorithm. The rapid changes of aerosol contents over the PRD region and Hong Kong can be monitored using our methodology with higher resolution and it is possible to pinpoint the sources of anthropogenic emission.



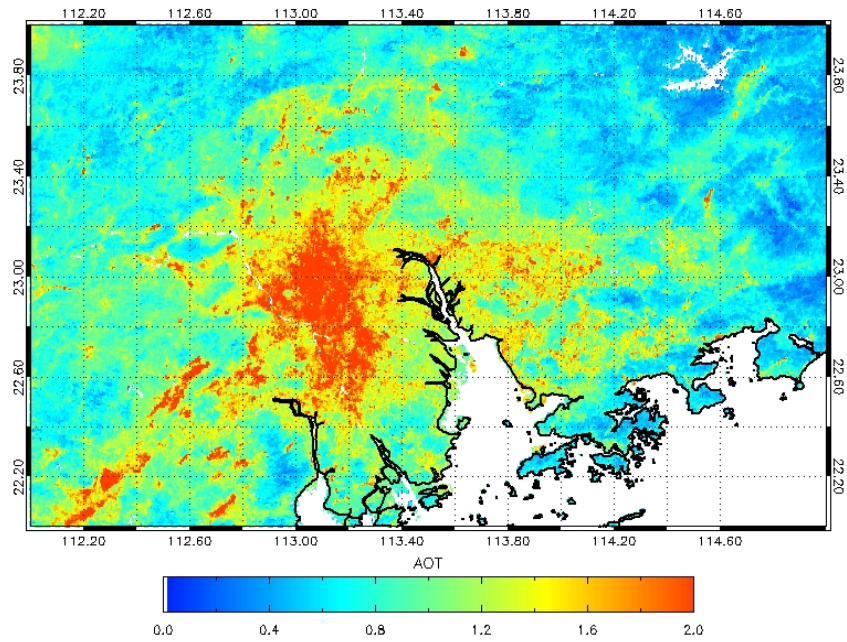
a.



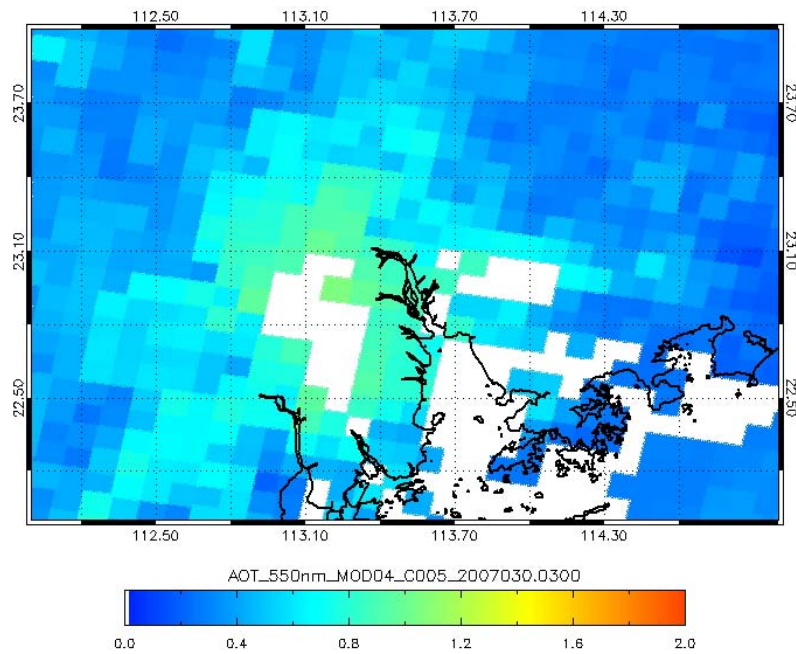
b.



c.



d.



e.

Figure 6.12. a. Color composite RGB image on Jan 28 2007; AOT at 550nm and 500m resolution derived from this study over Hong Kong and the Pearl River Delta region on, b. Jan 28 2007, d. Jan 30 2007; MODIS collection 5 AOT products (10km) on, c. Jan 28 2007, e. Jan 30 2007

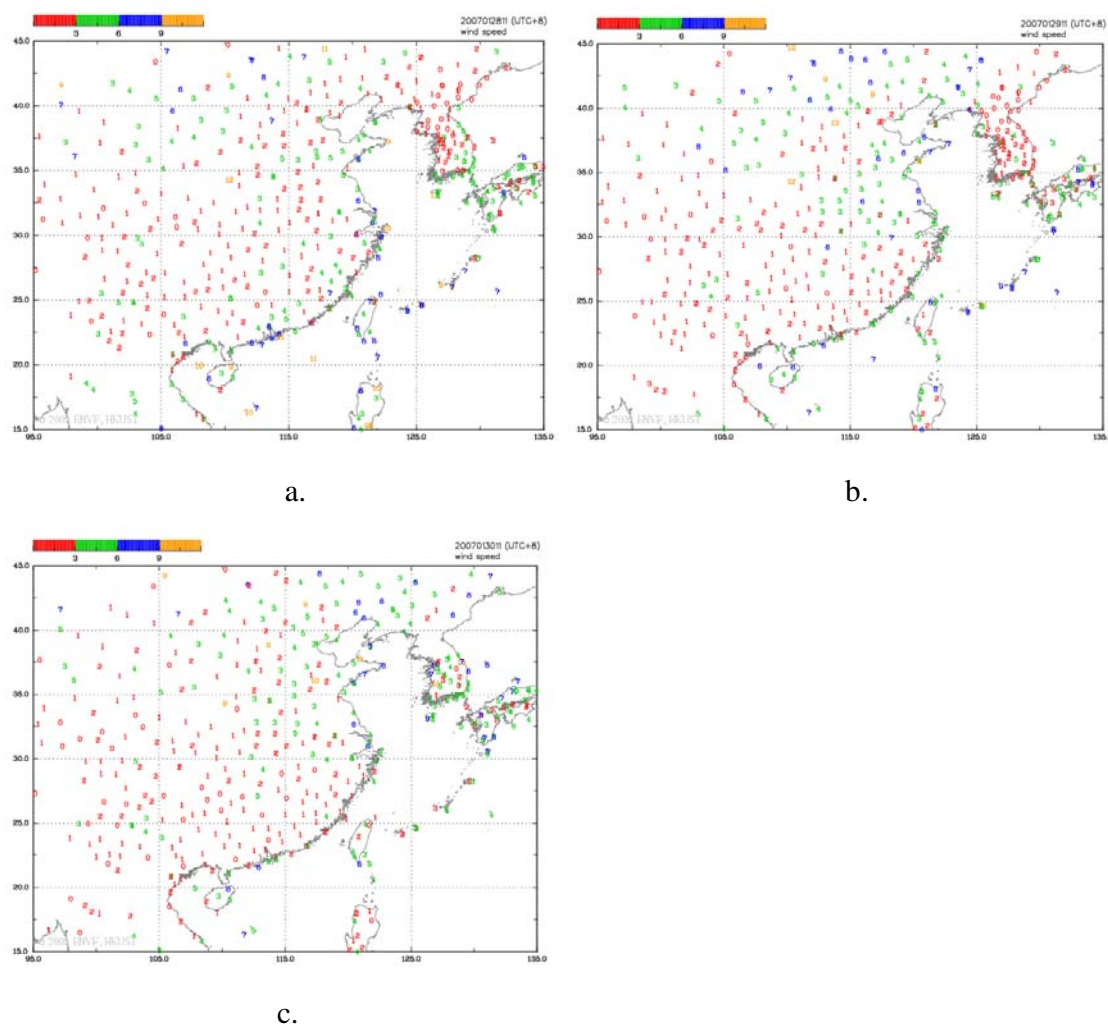


Figure 6.13. Wind speed maps over the whole of south China on, a. Jan 28 2007, b. Jan 29 2007, c. Jan 30 2007 (courtesy of the Institute for the Environment (IENV), the Hong Kong University of Science and Technology)

6.8. *Aerosols from biomass burning observed from AOT images*

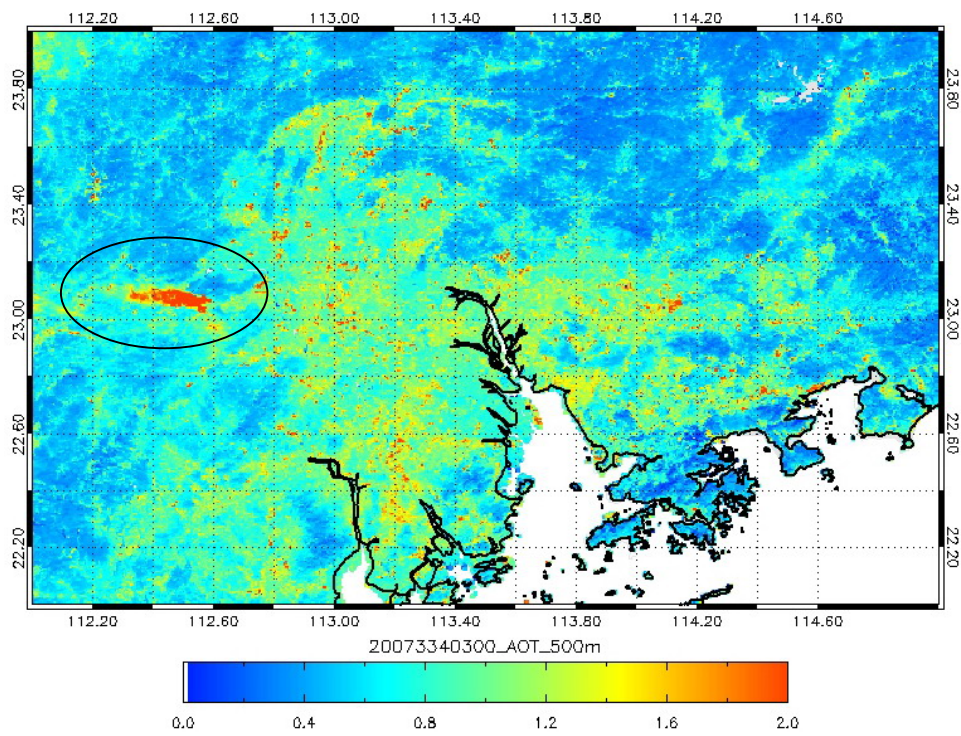
China is still an agricultural country, and had a yield of 690 million tons of straw in 2000 (Wang et al., 2007), of which 36% is used for domestic fuel and 7% is disposed by open fires (Gao et al., 2002). In the Pearl River Delta region with extensive areas of dense forest, biomass burning (intentionally or accidentally fires) occurs frequently. This

section demonstrates the application of the MODIS AOT 500 image to locate and pinpoint sources of biomass burning.

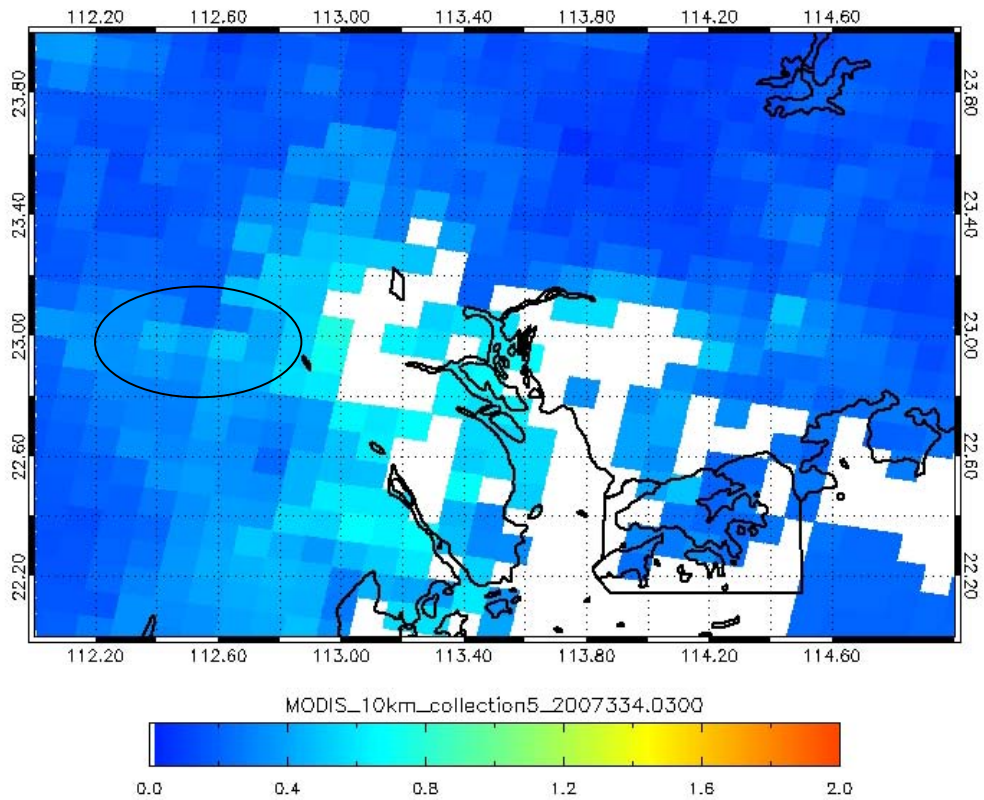
Figure 6.14a shows the Rayleigh corrected RGB image on Nov 30 2007. Biomass burning clearly evident on the left of the image (marked on the image) which is located in the dense forest area of Zhaoqing county. It is also observed with high AOT values (> 1.8) on MODIS 500 AOT images (Figure 6.14b). The smoke plumes and the source of burning can be easily identified on the AOT 500m image whereas it is not observable on MODIS 10km AOT image. In addition, a large patch of the urban areas are masked out with no AOT data values on MODIS collection 5 algorithm (Figure 6.14c) due to their high surface reflectances not meeting the surface reflectance criteria in the collection 5 AOT algorithm. Figure 6.14d shows the same fire spots located from the Web Fire Mapper developed by the Geographic Department of the University of Maryland. Also, the easterly wind from wind direction map confirmed the direction of fire smoke. The images derived from our study not only have the ability to retrieve aerosols over bright urban surfaces, but also can map the pollutant sources such as biomass burning.



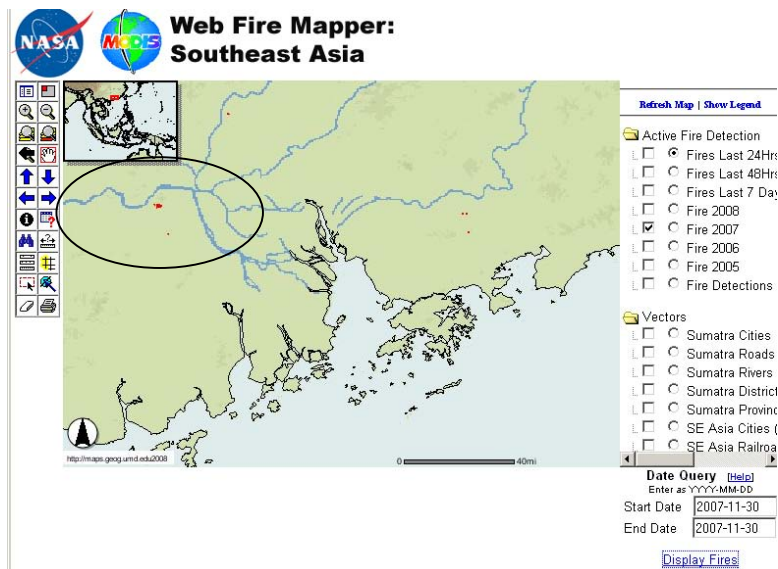
a.



b.



c.



d.

Figure 6.14. a. Rayleigh corrected RGB image on Nov 30 2007, b. AOT 500m image, c. AOT collection 5 10km image, d. Fire spots shown on Nov 30 2007 from the Web Fire Mapper

6.9. Monitoring fine particulate matter (PM_{2.5}) using AOT images

Fine particles in the atmosphere have recently been recognized as the most serious pollutant for their damage to the circulatory and respiratory systems (Dominici et al., 2006). However, most air quality stations measure only common gaseous pollutants, as well as total particulate matter in the form of respiratory suspended particulates or those smaller than 10µm (PM₁₀). The finer PM_{2.5} is usually measured at only a few ground stations eg. 5 out of 14 air quality stations in Hong Kong. Furthermore, such ground-based measurements do not provide spatially continuous data over a region, neither do they offer predictive capabilities. This section investigated the relationship between AOT derived from collection 5 and MODIS 500m satellite images and "in-situ" fine particulate matter (PM_{2.5}) from Hong Kong air quality monitoring stations.

Hong Kong has 14 air quality stations measuring hourly pollutant gases and particulates, but only 5 of them are equipped to monitor PM_{2.5} (Figure 6.15). The annual average PM_{2.5} concentrations for the years 2005, 2006 and 2007 are high, at 60, 56, 53 µg/m³ respectively, and exceed 24-hour air quality standards (note 1). However considerable spatial variation is usually present. For example, over last three years, Central station had the highest frequency of PM_{2.5} concentrations higher than 70 µg/m³, which occurred 4130 times. This compares with 4000 times at Yuen Long, 3618 times in Tung Chung, 3304 times at Tsuen Wan, and 2747 times at Tap Mun.

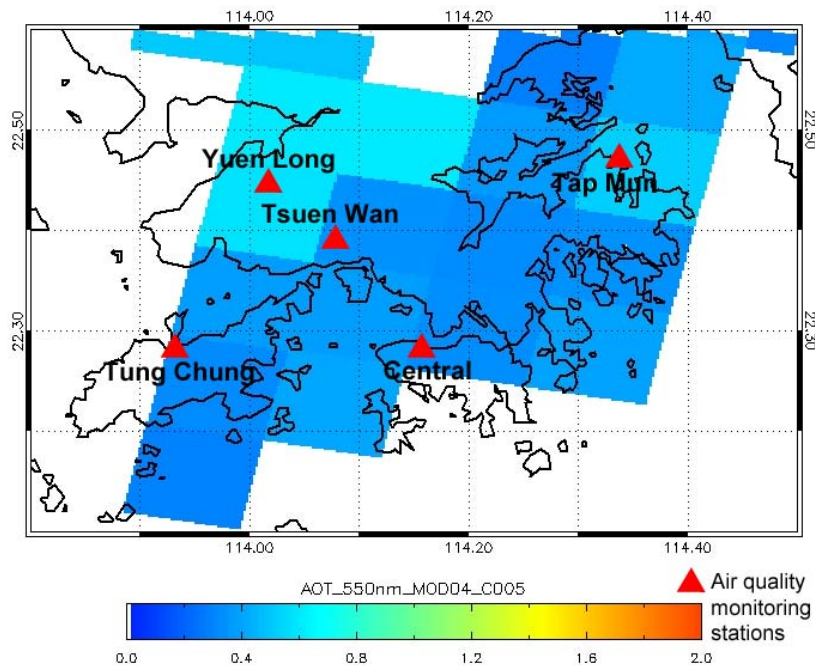


Figure 6.15. Monitoring stations in Hong Kong overlaid with MODIS collection 5 AOT image on Jan 28 2007

Correlation analysis was undertaken between collection 5, MODIS 500m AOT and PM_{2.5} concentration. Results show that only moderate correlation was obtained for collection 5 AOT at 10km resolution against PM_{2.5}. This was ($r^2 = 0.310$) for collection 5 AOT. This moderate correlation is similar to those of previous studies which also used the collection product at 10km resolution (Liu et al., 2005; Wang and Christopher, 2003; Engel-Cox et al., 2004; Hutchison et al., 2005), higher correlations have often been demonstrated when the data are controlled for more specific regional and temporal factors. Figure 6.16a shows the yearly averaged AOT derived from collection 5 data on 2007 and Figure 6.16b shows the modeled yearly PM_{2.5} on 2007.

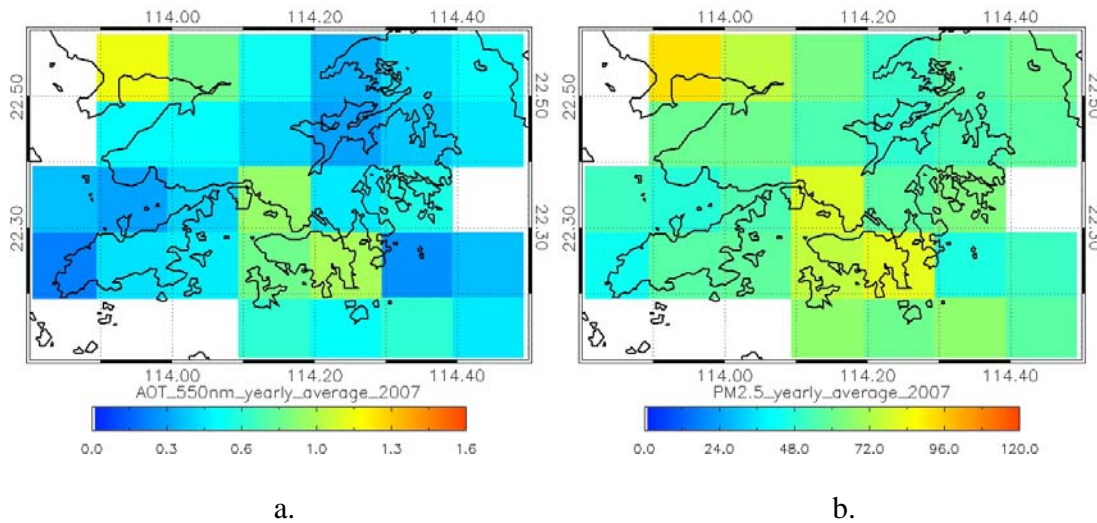


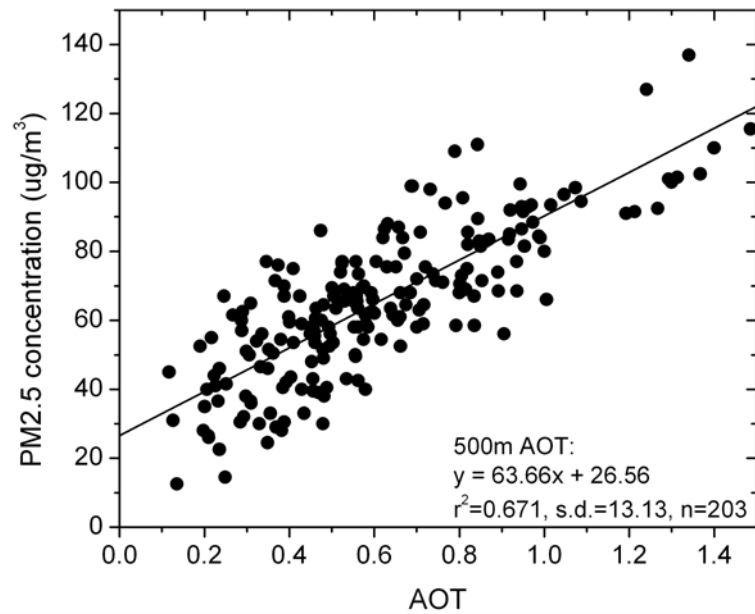
Figure 6.16. a. Yearly average collection 5 AOT in 2007, b. modeled yearly PM2.5 concentrations ($\mu\text{g}/\text{m}^3$) in 2007

Figure 6.17a shows the relationship between MODIS 500m AOT and PM2.5 concentrations. Compared with the MODIS collection 5 AOT at 10km ($r^2 = 0.310$), a much higher correlation ($r^2 = 0.671$), and much lower standard deviation are obtained. The derived equation is:

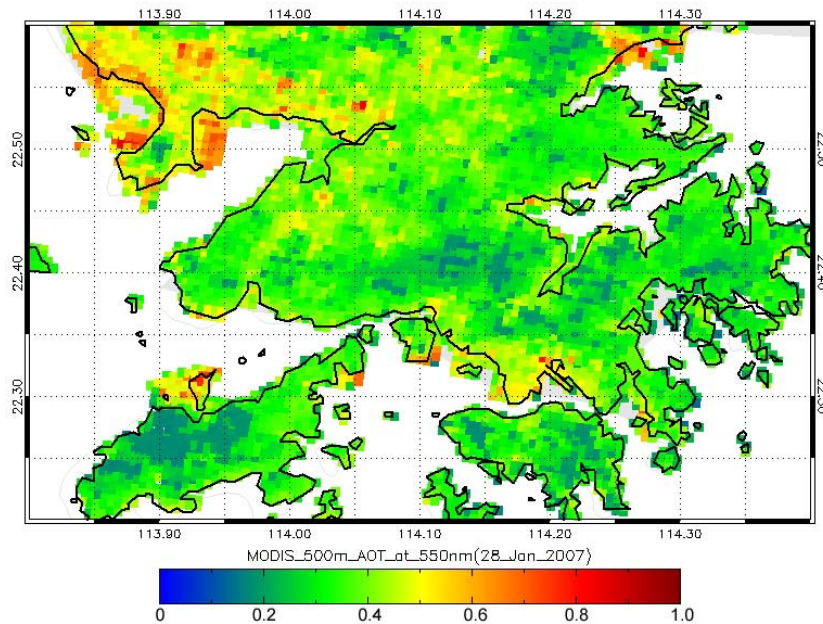
$$\text{PM2.5} = (63.66 \cdot \text{AOT}) + 26.56 \quad \text{Eq 6.2.}$$

The 500m AOT image and modeled PM2.5 image for Jan 28 2007 (Figure 6.17b and c) give values for areas which are masked out with no AOT data values on the MODIS collection 5 images (Figure 6.15) due to their surface reflectances not meeting the surface reflectance criteria in the collection 5 AOT algorithm. These are the western parts of Lantau island and southern part of Hong Kong island. Since the new aerosol retrieval algorithm works well over both bright and dark surfaces at 500m resolution, more AOT data can be retrieved (Figure 6.17b) permitting PM2.5 estimates over the whole region. Furthermore, the greater spatial detail of the AOT retrieval at 500m (Figure 6.17b) permits local areas with very high PM2.5 concentrations to be detected, namely the Hong Kong International airport, the Kowloon peninsula and areas bordering the mainland city of Shenzhen. Indeed on the image date, approximately two-thirds on the area of Hong

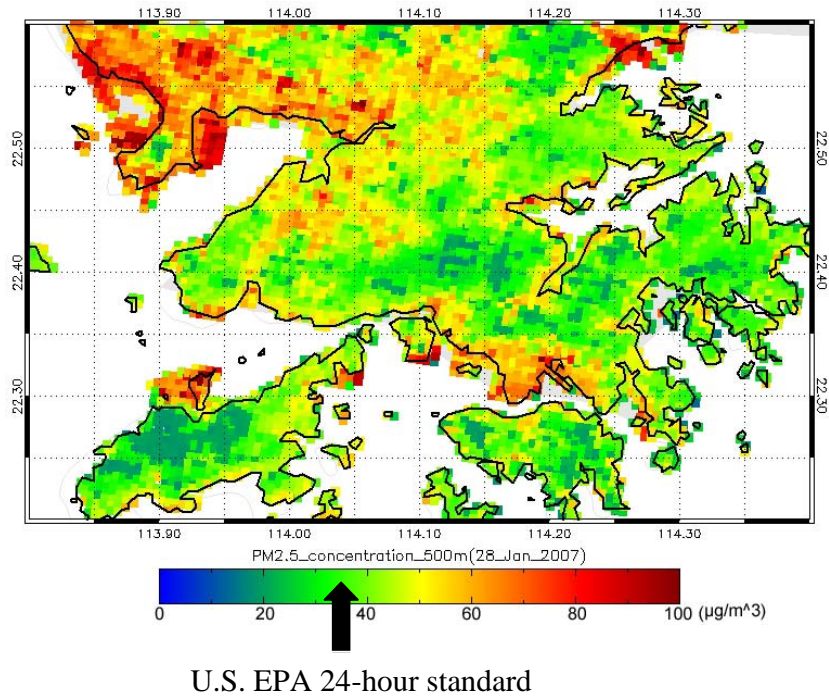
Kong appears to suffer from PM_{2.5} levels in excess of the U.S. EPA limit of 35 $\mu\text{g}/\text{m}^3$ over a 24-hour period (note 1). The high correlation of $r^2 = 0.671$ for the 500m AOT and PM_{2.5} data, is obtained across all data for 2007, with no attempt to control for other physical parameters as in other studies (Engel-Cox et al., 2004; Liu et al., 2005).



a.



b.



c.

Figure 6.17. a. Scatter plot of MODIS 500m AOT data versus PM_{2.5} measurements, b. 500m AOT map over Hong Kong on Jan 28 2007, c. modeled PM_{2.5} concentrations at 500m resolution over Hong Kong on Jan 28 2007

Note 1.

The United States Environmental Protection Department upgraded the 24-hour fine particle standards from 65 to 35 $\mu\text{g}/\text{m}^3$ in 2006.

CHAPTER 7.

DISCUSSION

The new aerosol retrieval algorithm shows good results from high resolution 500m MODIS satellite images, with strong correlations with AERONET ($r^2 = 0.767$) and MicrotopsII ($r^2 = 0.760$) sunphotometer measurements. Although a similar correlation (collection 5: $r^2 = 0.778$), similar RMS error (MODIS 500m = 0.176, collection 5 = 0.167), similar MAD error (MODIS 500m = 0.142, collection 5 = 0.129) and similar bias estimator (MODIS 500m = 0.011, collection 5 = 0.011) were obtained from MODIS 500m data compared with MODIS operational collection 5 products at 10km resolution, the signal to noise ratio of 10km resolution data is 20 times higher than the 500m resolution data (Kaufman and Tanré, 1998). However, this study tested the image AOT values at 500m resolution using both AERONET and MicrotopsII measurements, and on both high and low surface reflectance areas. The accuracy achieved is comparable to that for the 10km resolution data since the signal errors (aerosol signal errors influenced by background aerosol reflectance inside a kernel) had been reduced in the 10km retrieval. The MODIS collection 5 images have slightly higher accuracy than our algorithm, but the 16 additional datasets available and lower signal to noise ratio may explain this small advantage. Hsu et al. (2006) reported a general error of 20 to 30% for the Deep Blue algorithm. In this study, we found the error of AOT values from our methodology ($0.15/0.6 = 25\%$ where 0.6 is the mean AOT observed from MODIS on 2007) within this range when compared with the AERONET and MicrotopsII measurements (Table 7.1). Table 7.1 lists the expected errors, coverage and resolutions, bands used, working areas of MODIS collection 4, collection 5, Deep Blue, Li et al. (2005), and our algorithm. It is noticed that the expected error of our algorithm is comparable to those from the other methods, but is at higher spatial resolution.

	Working area	Band used	Coverage/ Resolution	Expected error
MODIS collection 4	Dense forest	0.47 μ m, 0.66 μ m, 2.12 μ m	Global/10km	~ 35% (ATBD: 0.21/0.6) ~ 28% (validated in this study: 0.17/0.6)
MODIS collection 5	Dense forest and semi- urban	0.47 μ m, 0.66 μ m, 2.12 μ m	Global/10km	~ 28% (ATBD: 0.17/0.6), ~ 22% (validated in this study: 0.13/0.6)
Deep Blue algorithm	Forest and urban	0.41 μ m, 0.49 μ m	Global/10km	20 – 30%
Li et al., 2005	Dense forest (interpolation for urban areas)	0.47 μ m, 0.66 μ m, 2.12 μ m	Hong Kong/1km	15 – 20% (validated between October to December in 2003)
Our method	Both urban and vegetated areas (eg. complex land)	0.47 μ m, 0.55 μ m, 0.66 μ m	Hong Kong and PRD region/500m	~ 25% (MAD: 0.15/0.6)

Table 7.1. Summary of different aerosol retrieval methods (ATBD stands for Algorithm Theoretical Basis Documents from MODIS; MAD stands for Mean Absolute Difference)

Although the 500m AOT has good agreement with ground measurements, the error sources in AOT retrieval are thought to be due to:

(i) the assumption of surface reflectance using MRT techniques. Although the surface reflectance images derived from the MRT technique were validated with the MOD09 surface reflectance images and MSR field measurements, the findings from both

validations suggest errors of 0 - 0.03 from the uncertainty of surface reflectance. This would be smaller at longer wavelengths and larger at shorter. The AOT uncertainty estimated from the errors of surface reflectance ranges from 0 to 0.3 whereas the actual errors when the AOT images were validated against AERONET and MicrotopsII measurements are smaller, 0.142 and 0.150 respectively. Thus, the error contribution on AOT retrieval from surface reflectance is not significant and the uncertainty of surface reflectance can be claimed as reasonable and acceptable.

(ii) the systematic bias from the aerosol model. Chu et al. (2002) stated the systematic bias from the aerosol model can range from 0 - 20% in collection 4 operational algorithm. However since aerosol models devised for Hong Kong were used, this error may be considerably reduced. Li et al. (2007) also indicated that the main causes of errors in AOT retrieval were due to the derivation of aerosol models and deviation of surface reflectance. For example, the collection 5 algorithm makes use of six aerosol models: two for very clean conditions, one for coarse-dominated aerosol and three for fine mode models, and since it is difficult to decide which of the fine mode models should be used, it assigns them according to location and season. Although Li et al. (2005) devised four aerosol models in 6S, namely, dust-like, water-soluble, oceanic, and soot, and determined their fraction of the basic models for each season in Hong Kong, high uncertainties are observed from modeling in the radiative transfer calculation. In this study, the clustering technique was adopted to derive the localized and regional aerosol models from AERONET measurements, since the data for constructing the models is local, and thus likely to obtain a better result than global scale models. Therefore, errors derived from the aerosol model used would be limited. In this study, only four clustering types were defined, which excluded rural and background aerosol types since the AERONET station is deployed in the city-center and rarely observed the rural and background aerosols. With the aid of data from the second AERONET station which is deployed at the remote site in the south of Hong Kong island (Hok Tsui), more observations of rural and background aerosols can be obtained. Further studies will couple the data from PolyU and Hok Tsui AERONET stations for clustering the Hong Kong and south China aerosol types.

(iii) the assumptions of insignificant adjacency effect. The adjacency effect causes a dark pixel to be affected by atmospheric scattering from the path of adjacent bright pixels between the ground and sensor. This effect is critical at the boundaries between bright and dark surfaces. The effect can be reduced by degrading and averaging the original pixel to coarser resolution but it will lose a level of detail. For our study, 500m resolution AOT images are produced which have smaller adjacency effects (Vermote, personal comment) than finer 250m resolution. In fact, there is no research which systematically describes and recommends a best resolution for aerosol retrieval to avoid the adjacency effect, but Justice et al. (1998) expected that the adjacency effect would be less significant for MODIS 250m and 500m pixels than for Landsat Thematic Mapper pixels.

(iv) the assumptions of insignificant BRDF effect. The Bidirectional Reflectance Distribution Function (BRDF) effect is caused by different viewing angles in heterogeneous areas. MODIS viewing angles are not constant and can vary from 0° to 65° . The errors caused from different viewing angles can be reduced by BRDF correction algorithms (Wu et al., 1995; Wong and Nichol, 2006) but is beyond the scope of this study. For reducing the BRDF in aerosol retrieval, only nadir images with satellite viewing angle $< 35^{\circ}$ have been considered in this study. Future work may be necessary to isolate the BRDF effect during aerosol retrieval.

(v) the assumption of accurate cloud masking. The study illustrates considerable spatial variability in AOT concentrations over the Pearl River Delta region and Hong Kong, and confirms the need for higher resolution AOT retrieval over both urban and rural areas. An accuracy of 78.13% is achieved for cloud masking in this study which is comparable to the accuracy from the MODIS operational algorithm which is 82%. Since the cloud removal adopted in this study is operated by thresholding and the thresholds were tested by a trial-and-error approach, if smaller cirrus clouds are still present on the images they may easily be confused with bright urban surfaces, and it was found that 43.48% of the image data still contains small and thin cirrus clouds without masking. In addition, cloud shadow is difficult to mask except by using very high resolution thermal images. Even

though collection 4 and 5 algorithms make use of the MODIS 1km thermal band for detecting and masking the clouds, sometimes the AOT end products show very high AOT over the sea with a large patch shape which is an error caused by clouds. Therefore, more analysis and tests will be considered in future work.

The aerosol retrieval methodology presented here can be transferred to other Asian cities such as Taipei and Singapore. The MODIS 500 AOT images are able to locate local scale anthropogenic emissions such as traffic “black-spots” and industrial emissions, map the rapid change of AOT in regional scale eg. between Jan 28 and 30 2007, and model the fine particulates (PM_{2.5}) in city-scale. Moreover, whereas MODIS collection 5 products masks high surface reflectances areas including fires, aerosols from biomass burning can be identified using the MODIS 500m AOT images, as the smoke plume and the source of burning can be easily identified. As such, they can be used for monitoring the influence of cross-boundary pollutants.

CHAPTER 8.

CONCLUSION

This study develops a new aerosol retrieval algorithm for MODIS data at 500m resolution based on a modified Minimum Reflectance Technique to derive surface reflectance images coupled with comprehensive Look Up Tables which consider many different aerosol models derived from Hong Kong AERONET measurements and sun-satellite geometries in radiative transfer modeling. The data from three years of AERONET measurements in Hong Kong including four different aerosol types, namely mixed urban, polluted urban, dust, and heavy pollution were identified by clustering. Their aerosol properties as well as the relative humidity acquired from the Hong Kong Observatory, solar zenith angles, view zenith angles, and relative sun/satellite azimuth angles were input to the LUT calculation. The localized and regional aerosol models devised in this study are more likely to be accurate for Hong Kong and the PRD region.

Good correlations were found between the MRT images and MOD09 surface reflectances. The differences between MRT and MOD09 images are between 0.01 - 0.03 at 470nm, 550nm and 660nm. Similar results were observed from MRT images compared with MSR field data. These give a potential AOT error of 0.3 in surface reflectance, but the results show the MAD errors to be only 0.142 and 0.150 when validated against AERONET and MicrotopsII measurements. These suggest the MRT images accurately represent surface reflectances, and are more accurate than existing collection 4 (DDV) and collection 5 algorithms because seasonal land cover changes as well as bright and dark surfaces are included in the estimations.

The MODIS 500m AOT is able to estimate aerosols over both urban and vegetated areas at a high spatial resolution. The derived MODIS 500m AOT shows a high level of accuracy ($r^2 = 0.767$, RMS error = 0.176, MAD error = 0.142 and bias estimator = 0.011) compared with ground-based AERONET measurements and good agreement ($r^2 = 0.760$, RMS error = 0.182, MAD error = 0.150, bias estimator = 0.011) with portable

MicrotopsII measurements at different sites. The general error of AOT is 0.15 (relative error is 25%). This study has demonstrated the possibility of using MODIS 500m AOT for mapping urban anthropogenic emissions, modeling fine particles (PM_{2.5}) and pinpointing biomass burning locations. Given the high accuracy and higher spatial resolution of the derived MODIS 500m AOT images, they can be used to monitor localized intra-urban aerosol distributions as well as to study transient cross-boundary aerosols.

REFERENCES

Ball R.J. and Robinson G.P., 1982. The origin of haze in the central United States and its effect on solar radiation. *Journal of Applied Meteorology*, 21:171-188.

Bucholtz A., 1995. Rayleigh-scattering calculations for the terrestrial atmosphere. *Applied Optics*, 34:2765-2773.

Business Environment Council, 2005. *Living Under Blue Skies: A Review of Air Pollution in Hong Kong and the Pearl River Delta*. A report from Business Environment Council, Hong Kong.

Cao J.J., Lee S.C., Ho K.F., Zhang X.Y., Zou S.C., Fung K., Chow J.C. and Watson J.G., 2003. Characteristics of carbonaceous aerosol in Pearl River Delta Region, China during 2001 winter period. *Atmospheric Environment*, 37(11):1451–1460.

Cao J.J., Lee S.C., Ho K.F., Zou S.C., Fung K., Li Y., Watson J.G. and Chow J.C., 2004. Spatial and seasonal variations of atmospheric organic carbon and elemental carbon in Pearl River Delta Region, China. *Atmospheric Environment*, 38(27):4447–4456.

Chang S.C. and Lee C.T., 2007. Secondary aerosol formation through photochemical reactions estimated by using air quality monitoring data in Taipei City from 1994 to 2003. *Atmospheric environment*, 41(19):4002-4017.

Cheng A.Y.S., Liu H. and Chan J.C.L., 1999. Lidar Observation of Atmospheric Processes in Hong Kong. In *Proceedings of the International Laser Sensing Symposium ILSS'99*, Fukui, Japan, Sep 6-8 1999, pp.67-70.

Chu A., Kaufman Y.J., Ichoku C., Remer L.A., Tanré D. and Holben B.N., 2002. Validation of MODIS aerosol optical depth retrieval over land. *Geophysical Research Letter*, 29(12):1–4.

CH2M HILL (China) Limited, 2002. Study of air quality in the Pearl River Delta region. Final report, R0355.01. Environmental Protection Department, The Government of Hong Kong Special Administrative Region.

Civic Exchange, 2007. Relative Significance of Local vs. Regional Sources: Hong Kong's Air Pollution.

(http://www.civic-exchange.org/eng/upload/files/200703_HKAirPollution.pdf)

Costa M.J., Cervino M., Cattani E., Torricella F., Levizzani V. and Silva A.M., 1999. Aerosol optical thickness and classification: Use of METEOSAT, GOME and modeled data, EOS-SPIE International Symposium on Remote Sensing. In *Proceedings of the SPIE Vol. 3867, Satellite Remote Sensing of Clouds and the Atmosphere IV*, Russell J.E. (Ed.), pp. 268–279.

Davidson C.I. and Phalen R.F., Solomon P.A., 2005. Airborne particulate matter and human health: A review. *Aerosol science and technology*, 39(8):737-749.

Deepak A., Box M.A. and Box G.P., 1980. Retrieval of aerosol size distribution from scattering and extinction measurements in the presence of multiple scattering. In *Remote Sensing of Atmospheres and Ocean*, Deepak A. (Ed.), Academic, pp.95 – 113.

Dominici F., Peng R.D., Bell M., Pham L., McDermott D., Zeger J. and Samet J., 2006. Fine Particulate Air Pollution and Hospital Admission for Cardiovascular and Respiratory Diseases. *Journal of the American Medical Association*, 295(10):1127-1134.

Dubovik O., Holben B.N., Kaufman Y., Yamasoe M.A., Smirnov A., Tanré D. and Slutsker I., 1998. Single-scattering albedo of smoke retrieved from the sky-radiance and

solar transmittance measured from the ground. *Journal of Geophysical Research*, 103(24):31903-31924.

Engel-Cox J.A., Holloman C.H., Coutant B.W. and Hoff R.M., 2004. Qualitative and quantitative evaluation of MODIS satellite sensor data for regional and urban scale air quality. *Atmospheric Environment*, 38:2495-2509.

EPD, 2004. Study of short term health impact and costs due to road traffic-related air pollution. Environmental Protection Department, The Government of Hong Kong Special Administrative Region.

Gao X.Z., Ma W.Q., Ma C.B., Zhang F.S. and Wang Y.H., 2002. Analysis on the current status of utilization of crop straw in China. *Journal of Huazhong Agricultural University*, 21:242 - 247.

Gatebe C.K., King M.D. Tsay S.C., Ji Q., Arnold G.T. and Li J.T., 2001. Sensitivity of off-nadir zenith angles to correlation between visible and near-infrared reflectance for use in remote sensing of aerosol over land. *IEEE Transactions on Geoscience and Remote Sensing*, 39(4):805-819.

Gnauk T., Mueller K., van Pinxteren D., He L.Y., Niu Y., Hu M. and Herrmann H., 2008. Size-segregated particulate chemical composition in Xinken, Pearl River Delta, China: OC/EC and organic compounds. *Atmospheric Environment*, 42(25):6296-6309.

Hao W.M. and Liu M.H., 1994. Spatial and temporal distribution of tropical biomass burning. *Global Biogeochemical Cycles*, 8:495-503.

Herman J.R. and Celarier E.A., 1997. Earth surface reflectivity climatology at 340–380 nm from TOMS data. *Journal of Geophysical Research*, 102:28003–28011.

Herman, J.R., Bhartia P.K., Torres O., Hsu C., Seftor C. and Celarier E., 1997. Global distribution of UV-absorbing aerosols from Nimbus 7/TOMS data. *Journal of Geophysical Research*, 102:16911-16922.

Hobbs P.V., 1993. *Aerosol-Cloud-Climate Interactions*. Academic Press Incorporation, San Diego, California.

Holben B.N., Eck T.F., Slutsker I., Tanré D., Buis J.P., Setzer A., Vermote E.F., Reagan J.A., Kaufman Y.J., Nakajima T., Lavenu F., Jankowiak I. and Smirnov A., 1998. AERONET-A federated instrument network and data archive for aerosol characterization. *Remote Sensing of Environment*, 66(1):1-16.

Hsu N.C., Herman J.R., Torres O., Holben B.N., Tanré D., Eck T.F., Smirnov A., Chatenet B. and Lavenu F., 1999. Comparison of the TOMS aerosol Index with Sun-photometer aerosol optical thickness: Results and application. *Journal of Geophysical Research*, 23:745-748.

Hsu N.C., Tsay S.C., King M.D. and Herman J.R., 2004. Aerosol Properties Over Bright Reflecting Source Regions. *IEEE Transactions on Geoscience and Remote Sensing*, 42(3):557-569.

Hsu N.C., Tsay S.C., King M.D. and Herman J.R., 2006. Deep Blue Retrievals of Asian Aerosol Properties During ACE-Asia. *IEEE Transactions on Geoscience and Remote Sensing*, 44(11):3180-3195.

Husar R.B., Prospero M.J. and Stowe L.L., 1997. Characterization of tropospheric aerosols over the oceans with the NOAA advanced very high resolution radiometer optical thickness operational product. *Journal of Geophysical Research*, 102(D14):16889-16909.

Hutchison K.D., Smith S. and Faruqui S.J., 2005. Correlating MODIS aerosol optical thickness data with ground-based PM_{2.5} observations across Texas for use in a real-time air quality prediction system. *Atmospheric Environment*, 39:7190-7203.

Intergovernmental Panel on Climate Change (IPCC), 2001. *Climate Change 2001: The Scientific Basis, Contribution of Working Group I to the Third Assessment Report of the Intergovernmental Panel on Climate Change*. Cambridge University Press, New York, pp.944.

Intergovernmental Panel on Climate Change (IPCC), 2007. *Climate Change 2007: The Physical Science Basis. Contribution of Working Group I to the Fourth Assessment Report of the Intergovernmental Panel on Climate Change*.

Junge C.E., 1952. Die Konstitution der atmosphärischen aerosols, *Annalen der Meteorologie*, pp.1-55.

Justice C.O., Vermote E., Townshend J., Defries R., Roy D.P., Hall D.K., Salomonson V., Privette J.L., Riggs G., Strahler A., Lucht W., Myneni R., Knyazikhin Y., Running S., Nemani R., Wan Z., Huete A., Leeuwen W., Wolfe R., Giglio L., Muller J., Lewis P. and Barnsley M., 1998. The Moderate Resolution Imaging Spectroradiometer (MODIS): Land remote sensing for global change research. *IEEE Transactions on Geoscience and Remote Sensing*, 36:1228–1249.

Justice C.O., Giglio L., Korontzi S., Owens J., Morisette J.T., Roy D.P., Descloitres J., Alleaume S., Petitcolin F. and Kaufman Y., 2002. The MODIS fire products. *Remote Sensing of Environment*, 83:244-262.

Karnieli A., Kaufman Y.J., Remer L.A. and Ward A., 2001. AFRI—aerosol free vegetation index. *Remote Sensing of Environment*, 77:10–21.

Kasten, F. and Young A.T., 1989. Revised optical air mass tables and approximation formula. *Applied Optics*, 28:4735–4738.

Kaufman Y.J. and Sendra C., 1987. Algorithm for automatic atmospheric corrections to visible and near-IR satellite imagery. *International Journal of Remote Sensing*, 9(8):1357-1381.

Kaufman Y.J., Tanré D., Gordon H.R., Nakajima T., Lenoble J., Frouin R., Grassl H., Herman B.M., King M.D. and Teillet P.M., 1997. Passive remote sensing of tropospheric aerosol and atmospheric correction for the aerosol effect. *Journal of Geophysical Research*, 102(D14):16815-16830.

Kaufman Y.J. and Tanré D., 1998. Algorithm for remote sensing of tropospheric aerosol from MODIS, NASA MOD04 product report.

Ko F.W.S., Tam W., Wong T.W., Chan D.P.S., Tung A.H., Lai C.K.W. and Hui D.S.C., 2007. Temporal relationship between air pollutants and hospital admissions for chronic obstructive pulmonary disease in Hong Kong. *Thorax*, 62:780–785.

Koelemeijer R.B.A., de Haan J.F. and Stammes P., 2003. A database of spectral surface reflectivity in the range 335–772 nm derived from 5.5 years of GOME observations. *Journal of Geophysical Research*, 108:4070.

Lee K.H., Kim Y.J., von Hoyningen-Huene W. and Burrow J.P., 2007. Spatio-Temporal Variability of Atmospheric Aerosol from MODIS data over Northeast Asia in 2004. *Atmospheric Environment*, 41(19):3959-3973.

Lenoble J., and Brogniez C., 1984, A Comparative Review of Radiation Aerosol Models. *Beiträge Zur Atmosphärenphysik*. 57:1–20.

Levy R.C., Remer L.A., Martins J.V., Kaufman Y.J., Plana-fattori A., Redemann J. and Wenny B., 2004. Evaluation of the MODIS aerosol retrievals over ocean and land during CLAMS. *Journal of the Atmospheric Science*, 62(4):974-992.

Levy R.C., Remer L.A., Mattoo S., Vermote E.F. and Kaufman Y.J., 2007. Second-generation operational algorithm: Retrieval of aerosol properties over land from inversion of Moderate Resolution Imaging Spectroradiometer spectral reflectance. *Journal of Geophysical Research*, 112, D13211.

Li C.C., Lau A.K.H., Mao J.T. and Chu D.A., 2005. Retrieval, validation, and application of the 1-km aerosol optical depth from MODIS measurements over Hong Kong. *IEEE Transactions on Geoscience and Remote Sensing*, 43(11):2650-2658

Li Z., Niu F., Lee K.H., Xin J., Hao W.M., Nordgren B., Wang Y. and Wang P., 2007. Validation and understanding of Moderate Resolution Imaging Spectroradiometer aerosol products (C5) using ground-based measurements from the handheld Sun photometer network in China. *Journal of Geophysical Research*, 112, D22S07.

Liepert B., Fabian P. and Grassl H., 1994. Solar radiation in Germany – Observed trends and an assessment of their causes; Part I: Regional approach. *Beiträge Zur Atmosphärenphysik*, 67:15-29.

Liu Y., Sarnat J.A., Kilaru V., Jacob D.J. and Koutrakis P., 2005. Estimating Ground-Level PM_{2.5} in the Eastern United States Using Satellite Remote Sensing. *Environmental Science and Technology*, 39:3269-3278.

Lo J.C.F., Lau A., Fung J.C.H. and Chen F., 2006. Investigation of enhanced cross-city transport and trapping of air pollutants by coastal and urban land-sea breeze circulations. *Journal of Geophysical Research*, 111, D14.

MacQueen J.B., 1967. Some Methods for classification and Analysis of Multivariate Observations. In Proceedings of the 5th Berkeley Symposium on Mathematical Statistics and Probability, Berkeley, University of California Press, 1:281-297.

Martonchik J.V., Diner D.J., Kahn R.A., Ackerman T.P., Verstraete M.M., Pinty B. and Gordon H.R., 1998. Techniques for the retrieval of aerosol properties over land and ocean using multiangle imaging. *IEEE Transactions on Geoscience and Remote Sensing*, 36:1212– 1227.

Martonchik, J.V., Diner D.J., Crean K.A. and Bull M.A., 2002. Regional aerosol retrieval results from MISR. *IEEE Transactions on Geoscience and Remote Sensing*, 40:1520–1531.

Mi W., Li Z., Xia X.G., Holben B., Levy R., Zhao F.S., Chen H.B. and Cribb M., 2007, Evaluation of the MODIS Aerosol Products at Two AERONET Stations in China. *Journal of Geophysical Research*, 112, D22S08.

Mie G., 1908. On optical characteristics of turbid media, with special reference to colloid. metallic solutions. *Annals of Physics*, 25:377-445.

MRTSwath, 2006. MODIS Reprojection Tool – Swath. User’s Manual, Land Processes DAAC USGS Center for Earth Resources Observation and Science (EROS), Release 2.1, Jan, 2006.

National Research Council, 1996. A plan for a research program: Aerosol Radiative Forcing and Climate Change. National Academy Press, Washington D.C..

Nichol J.E., Wong M.S. and Chan Y.Y., 2008. Fine resolution air quality monitoring from a small satellite images, CHRIS/PROBA. *Sensors*, 8(12):7581-7595.

Omar A.H., Won J.G., Winker D.M., Yoon S.C., Dubovik O. and McCormick M.P., 2005. Development of global aerosol models using cluster analysis of Aerosol Robotic Network (AERONET) measurements. *Journal of Geophysical Research*, 110, D10.

Remer L.A., Gasso S., Hegg D., Kaufman Y.J. and Holben B., 1996. Urban/industrial aerosols: ground based sun/sky radiometer and airborne in situ measurements. *Journal of Geophysical Research*, 02(D14):16849–16860.

Remer L.A., Wald A.E. and Kaufman, Y.J., 2001. Angular and seasonal variation of spectral surface reflectance ratios: Implications for the remote sensing of aerosol over land. *IEEE Transactions on Geoscience and Remote Sensing*, 39(2):275-283.

Remer, L.A., Kaufman Y.J., Tanré D., Mattoo S., Chu D.A., Martins J.V., Li R-R., Ichoku C., Levy R.C., Kleidman R.G., Eck T.F., Vermote E. and Holben B.N., 2005. The MODIS Aerosol Algorithm, Products and Validation. *Journal of the Atmospheric Science*, 62(4):947-973.

Ricchiuzzi P., Yang S.R., Gautier C. and Sowle D., 1998. SBDART: A research and teaching software tool for plane-parallel radiative transfer in the Earth's atmosphere. *Bulletin of the American Meteorological Society*, 79(10):2101-2114.

Schutz L.W., Prospero J.M., Buat-Menard P., Carvalho R.A.C., Cruzado A., Harriss R., Heidam N.Z. and Jaenicke R., 1990. In *The Long-Range Atmospheric Transport of Natural and Contaminant Substances*. NATO ASI Series C: Mathematical and Physical Sciences 297, Knap A.H. (Ed.), pp.197-230.

Seinfeld J.H. and Pandis S.N., 1998. *Atmospheric Chemistry and Physics. From Air Pollution to Climate Change*. John Wiley and Sons, New York, pp.1326.

Sifakis N., Soulakellis N.A. and Paronis D.K, 1998. Quantitative mapping of air pollution density using earth observations: a new processing method and applications to an urban area. *International Journal of Remote Sensing*, 19:3289-3300.

Scorer R.S., 2002. *Air pollution meteorology*, Horwood Publishing Limited, England.

Swap R., Garstang M. and Greco S., 1992. Saharan dust in the Amazon Basin. *Tellus*, 44B:133-149.

Tanré D., Kaufman Y.J., Herman M. and Mattoo S., 1997. Remote sensing of aerosol properties over oceans using the MODIS/EOS spectral radiances. *Journal of Geophysical Research*, 102:16971-16988.

Torricella F., Cattani E., Cervino M., Guzzi R. and Levoni C., 1999. Retrieval of aerosol properties over the ocean using global ozone monitoring experiment measurements: Method and applications to test cases. *Journal of Geophysical Research*, 104(D10): 12085-12098.

Vermote E.F. and El Saleous N.Z., 2006. Operational atmospheric correction of MODIS visible to middle infrared land surface data in the case of an infinite lambertian target. In: *Earth Science Satellite Remote Sensing, Science and Instruments*, Qu J. et al. (Ed.), 1(8):123-153.

von Hoyningen-Huene W., Kokhanovsky A.A., Wuttke M.W., Buchwitz M., Noë S., Gerilowski K., Burrows J.P., Latter B., Siddans R. and Kerridge B.J., 2006. Validation of SCIAMACHY top-of-atmosphere reflectance for aerosol remote sensing using MERIS L1 data. *Atmospheric Chemistry and Physics*, 6:673-699.

Wallace J.M. and Hobbs P.V., 2006. *Atmospheric Science: An Introductory Survey* (Second Edition), Academic Press, pp.169-181.

Wang J. and Christopher S.A., 2003. Intercomparison between satellite-derived aerosol optical thickness and PM_{2.5} mass: Implications for air quality studies. *Geophysical Research Letters*, 30:2095.

Wang Q., Shao M., Liu Y., William K., Paul G., Li X., Liu Y. and Lu S., 2007. Impact of biomass burning on urban air quality estimated organic tracers: Guangzhou and Beijing as cases. *Atmospheric Environment*, 41:8380-8390.

Wanner W., Strahler A.H., Hu B., Lewis P., Muller J.P., Li X., Barker Schaaf C.L. and Barnsley M.J., 1997, Global retrieval of bidirectional reflectance and albedo over land from EOS MODIS and MISR data: Theory and algorithm. *Journal of Geophysical Research*, 102(17):143-162.

Ward J.H., 1963. Hierarchical grouping to optimize an objective function. *Journal of the American Statistical Association*, 58:236-244.

Wei F., Teng E., Wu G., Hu W., Wilson W.E., Chapman R.S., Pau J.C. and Zhang J., 1999. Ambient concentrations and elemental compositions of PM₁₀ and PM_{2.5} in four Chinese cities. *Environmental Science & Technology*, 33(23):4188–4193.

Wong M.S. and Nichol J.E., 2006. Investigation of the geometric effects of multiple view angle satellite images on surface reflectance: a preliminary study for aerosol retrieval. In *Proceedings of the 1st Faculty Postgraduate Research Conference (2006)*, FCLU, The Hong Kong Polytechnic University, Hong Kong, Nov 4, 2006.

Wong M.S., Nichol J.E., Lee H.K. and Li Z.Q., 2007. Analysis of seasonal variation of aerosol optical depth and characterization of aerosol model using MODIS and AERONET measurements, a study in Hong Kong, In *Proceedings of the 10th International Conference on Atmospheric Sciences and Applications to Air Quality*, The Hong Kong Polytechnic University, Hong Kong, May 14-16, 2007.

Wong M.S., Nichol J.E. and Lee K.H., 2008. Anthropogenic heat mapping using satellite images, The Second Workshop on Earth Observation for Urban Planning and Management, The Hong Kong Polytechnic University, Hong Kong, May 20, 2008.

Wong T.W., Lau T.S., Yu T.S., Neller A., Wong S.L., Tam W. and Pang S.W., 1999. Air pollution and hospital admissions for respiratory and cardiovascular diseases in Hong Kong. *Occupational and Environmental Medicine*, 56:679-683

Wu, A., Li Z. and Cihlar J., 1995. Effects of land cover type and greenness on advanced very high resolution radiometer bidirectional reflectances: analysis and removal. *Journal of Geophysical Research*, 100:9179-9192.

Wu D., Tie X., Li C., Ying Z., Lau A.K.H., Huang J., Deng X. and Bi X., 2005. An extremely low visibility event over the Guangzhou region: A case study. *Atmospheric Environment*, 39:6568-6577.

Yuan Z., Lau A., Zhang H., Yu J.Z., Louie P.K. and Fung J., 2006. Identification and spatiotemporal variations of dominant PM10 sources over Hong Kong. *Atmospheric Environment*, 40:1803-1815.